Universitat Autònoma de Barcelona
Departament de Física
Tesi doctoral en Física
Curs Academic 2012–2013

Observing the VHE Gamma Ray Sky with the MAGIC Telescopes: the Blazar B3 2247+381 and the Crab Pulsar

Candidat
Gianluca Giavitto

Director
Dr. Daniel Mazin

Co-director
Dr. Juan Cortina

Tutor
Prof. Enrique Fern□ndez

A mia sorella Laura.

I hereby declare that I am the sole author of this thesis.

The data presented in this thesis is propriety of the MAGIC collaboration when not otherwise stated.

Gianluca Giavitto

I authorize the Universitat Aut□noma de Barcelona to lend this thesis to other institutions or individuals for the purpose of scholarly research.

Gianluca Giavitto

Acknowledgements

I would like to acknowledge the essential contributions of Daniel Mazin and Juan Cortina to this work: they have helped me with their insightful comments and suggestions throughout the whole period of its preparation, and they supported during the last, hectic weeks. I would also like to thank Stefan Klepser for the assistance and the encouragements.
I'm thankful to the IFAE Barcelona for giving me the opportunity to be part of the MAGIC Collaboration, and to all the members of the Collaboration itself, especially those in the Pulsar and AGN groups. A personal thank you goes to the present and former IFAE students Roberta Zanin, Diego Tescaro, Ruben L□pez Coto, Alicia L□pez, Ignasi Reichardt, Adiv Gonz□lez, Jelena Alecsi□. Thanks to Riccardo Paoletti, Hanna Kellerman and the rest of the MPI students.

Contents

1. Introduction

This chapter contains a brief overview on the general proprieties of cosmic radiation. The aim is to present the current status of the field of astroparticle physics and its open questions.

Its first part gives a quick overview on cosmic radiation, covering general aspects of the physics of cosmic rays, while its second part focuses on gamma rays only.

1.1 Cosmic rays

Cosmic rays were discovered in the early twentieth century as a results of baloon-borne experiments on atmospheric ionization. First Viktor F. Hess (Hess, 1912), later KolhHrster (KolhHrster, 1913) observed an increase in the rate of discharge of electroscopes with increasing altitude, and concluded (Hess, 1913) that its cause was a penetrating radiation of extraterrestrial origin. The collective term "cosmic rays" was coined in 1926 by Robert A. Millikan (Millikan and Cameron, 1926), however it was soon discovered by experiments with Geiger-MXller detectors in coincidence (Bothe and KolhHrster, 1929) that the cosmic radiation was of corpuscular nature, and it was due to high-energy charged particles. It is now a general term used to indicate particles coming from the cosmos. Later experiments showed that cosmic rays could initiate showers of secondary charged particles, both in cloud chambers and in the atmosphere: in 1938 Pierre Auger using a number of separated detectors discovered (Auger et al., 1938) that some of these air showers could extend over hundreds of meters on the ground and contained millions of charged particles. He concluded that the primary particles hitting the upper atmosphere must have had energies exceeding 10^{15} eV. From the 1930s until the 1950s, before man-made particle accelerators reached very high energies, cosmic rays were the only way of investigating high energy particle physics, and led to the discoveries of fundamental particles such as the positron (Anderson, 1933; Blackett and Occhialini, 1933), the muon (Anderson and Neddermeyer, 1936), the kaon (Rochester and Butler, 1947) and the pion (Lattes et al., 1947). Afterwards, the focus of research on cosmic rays shifted towards understanding their origin, the astrophysical processes that accelerate them to such high energies, and the physics of their propagation in the interstellar medium, using satellite-borne detectors or large ground installations to sample air showers.

In the 1980s and 1990s experiments on neutrinos coming from the sun and the supernova SN1987a questioned the standard model of particle physics exposing the first evidence of neutrino oscillation due to flavour mixing.
At present, research on cosmic rays is a very vast topic, broadly touted "astroparticle physics", that intersects at least three branches of classical physics: particle physics (e.g. study of fundamental particle interactions at very high energies, search for exotic physics), astrophysics (from planetary to extragalactic physics) and cosmology. It can be schematically divided into interconnected fields with different scales of length and time as shown in Fig. 1.1.

Furthermore, cosmic rays give rise or contribute to many terrestrial phenomena important to other sciences, such as archeology or climatology:

- about 16.4% (0.39 mSv) of the average absorbed dose of natural background radiation is due to cosmic rays (UNSCEAR, 2010).
- radiocarbon dating via ^{14}C isotopes is possible because the reaction

  $$+^{14}\mathrm{N} \rightarrow {}^{14}\mathrm{C} + \mathrm{p}$$

  is initiated by neutrons of cosmic ray origin.
- cloud formation has been linked to the ionization of air due to cosmic rays (Svensmark et al., 2007).
- lightning is possibly initiated by cosmic rays via the so called "runaway breakdown" process (Gurevich et al., 2003).
- long-term climate change could possibly be linked to the variability in the cosmic ray flux due to the galaxy spiral arm crossing of the solar system, on timescales of about 135 million years (Scherer et al., 2006).

In the following paragraphs I will summarize the current expermiental knowledge about cosmic rays, and how this information fits in with our understanding of their physics, origin and propagation.
It will be shown that cosmic rays energies follow a power-law distribution, different to the Maxwell-Boltzmann distribution associated to thermal movement. They are messengers of the *non-thermal* processes of our Universe.

Energy spectrum of cosmic rays

There are four different ways to describe the spectra of the components of the cosmic radiation:

- By particles per unit rigidity. Propagation and acceleration through cosmic magnetic fields depend on magnetic rigidity, R, which is gyroradius r_g multiplied by the magnetic field strength B:

  $$R = \frac{pc}{Ze} B = r_g B \tag{1.1}$$

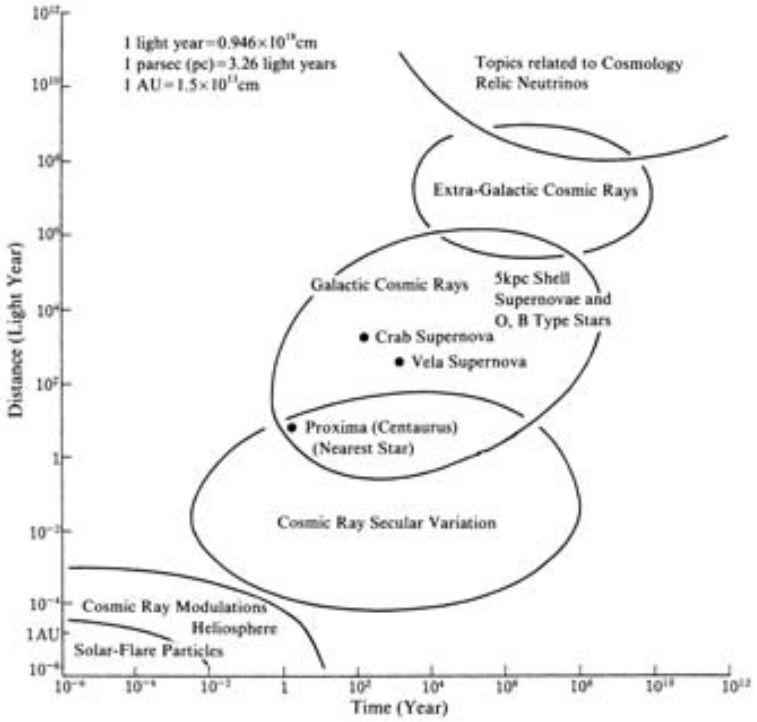

Figure 1.1
Research fields in cosmic ray astrophysics as a function of scale-length and time in the universe. From Oda et al. (1988, chapter 2).

- By particles per energy-per-nucleon. Fragmentation of nuclei propagating through the interstellar gas depends on energy per nucleon, since that quantity is approximately conserved when a nucleus breaks up on interaction with the gas.
- By nucleons per energy-per-nucleon. Production of secondary cosmic rays in the atmosphere depends on the intensity of nucleons per energy-per-nucleon, approximately independently of whether the incident nucleons are free protons or bound in nuclei.
- By particles per energy-per-nucleus. Used in air shower experiments, whose measured quantities are related to total energy per particle.

Differential energy spectra intensities are usually measured in particles $\times m^{-2}$ $\times s^{-1}$ $\times sr^{-1}$ $\times \varepsilon^{-1}$, where ε represents the units of one of the four variables listed above.

Protons and nuclei arriving at Earth span an energy range of about 14 orders of magnitude, from 10^6 to 10^{20} eV. Their flux at 1 MeV is about 10^4 particles per square meter per second, and it falls to less than 1 particle per square kilometer per century at 10^{19} eV. Electrons and positrons have a flux that is a couple of orders of magnitude lower. Even lower still ($\sim 2 \times 10^{-4}$ at 10 GeV) is the flux of cosmic antiprotons compared to the one of protons.

Due to the wide energy range and the rapidly changing flux, it is obvious that differ-

ent experimental techniques are needed in diverse energy regions. Direct measurements of the cosmic rays can be performed by means of detectors mounted on satellites or flown on baloons at very high altitudes. At low energies nuclear emulsions can be used to determine the charge and the energy of the primary; in the GeV-TeV region scintillator counters, trackers and calorimeters have been used. Above 10^{14} eV, the low fluxes due to the steeply falling spectrum force investigators to exploit indirect ground-based methods, such as detecting the extensive particle showers generated by the interaction of cosmic rays in the atmosphere.

Below energies of few GeV per nucleon, the energy spectra of the lighter particle species (protons and leptons) show a pronounced cut-off. Its cause is the solar wind outflow interfering with their propagation within the heliosphere, and impeding their diffusion towards the Earth. In fact, the scale length of magnetic irregularities in the solar system is of the order of the gyroradius of ~ GeV particles (Longair, 2011). The energy and shape of the cutoff show a time dependency anti-correlated with the solar activity: the greater the solar activity, the weaker the flux, as shown in Fig. 1.2.

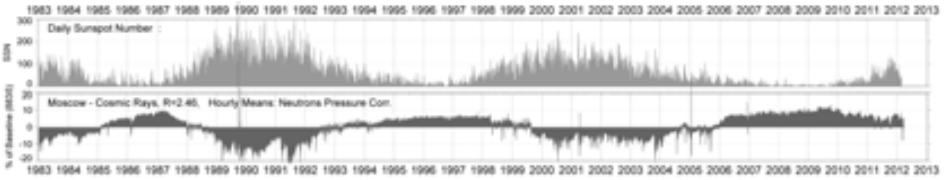

Figure 1.2
Anti-correlation between the sunspot number and the cosmic ray flux with rigidity R = 2.46 GV. From Wilkinson (2012).

The spectrum of electrons an positrons will be described later on, in the following we will refer only to the spectrum of hadrons (protons and nuclei). Between few GeV and few TeV per nucleon, their differential energy spectrum (shown in Fig. 1.3) follows a power law of the form

$$I_N(E) = I_0 E^{-\alpha} \approx 1.8 \times 10^4 \left(\frac{E}{1\ \mathrm{GeV}}\right)^{-2.7} \frac{\text{nucleons}}{\mathrm{m^2\ s\ sr\ GeV}} \tag{1.2}$$

There are, however, significant differences between the energy spectra of different elements which will be described later in §1.1.3.

Important features are present in the spectrum shown in Fig. 1.3: the differential spectral index α is about 2.7 from about 1 until 100 GeV and steepens (softens) slightly to 3.1 at the so-called "knee" region, around 3-4 PeV. A further spectral index softening is present also at the "second knee", near 400 PeV and a flattening (hardening) is measured at the "ankle", a broader feature around 3 EeV. These spectral changes are made more evident in Fig. 1.4, where the differential spectrum is multiplied by $E^{2.6}$, where E is the particle energy.
Below 100 GeV several processes besides solar modulation compete in shaping the spectrum: convection, reacceleration, nuclear fragmentation, electromagnetic losses. An in-depth study of their effects (often difficult to disentangle unambiguosly) is outside the scope of this introduction; for a recent review see Castellina and Donato (2011, and references therein)

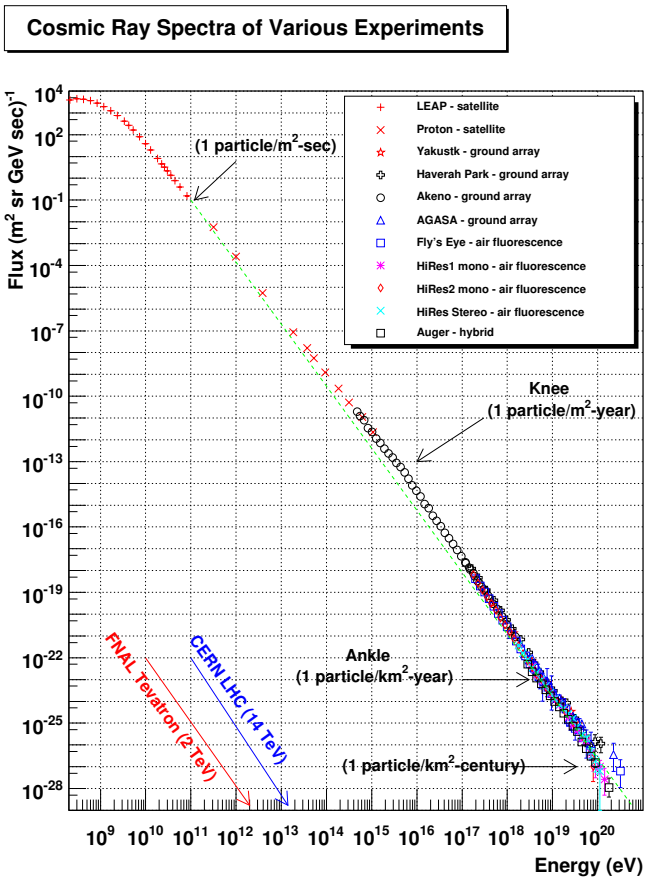

Figure 1.3
Differential energy spectrum of protons and nuclei in cosmic rays. Direct measurements by satellites or baloon flights go up to the knee. Above that indirect measurement techniques such as air shower scintillator arrays are employed. At low energies, only the flux of primary protons is shown. From Hanlon (2012, and references therein).

From 10^{11} up to 10^{18} eV the spectrum of cosmic rays is thought to be shaped basically by acceleration and diffusion of cosmic rays inside our local galaxy.
The spectral region between "knee", the "ankle" is not fully understood yet, however, a hypothesis blessed by long tradition explains it as the signature of the transition from galactic to extra-galactic cosmic rays (Hillas, 1984; Gaisser, 2006), itself determined by constraints on particle propagation and acceleration in the galaxy. A couple of simple dimensional arguments will illustrate this in the following.
Indicatively, particles are confined in the galaxy until their gyroradius r_g inside the galactic magnetic field $B \sim 0.3$ nT (as derived from pulsar rotation measures) is smaller than the thickness of the galactic disk $D \sim 1$ kpc. Partcles start to leak out when $r_g > D$. Inverting equation 1.1 we obtain that the rigidity at which particles start to escape is $R_{\rm esc} \approx 10^{15} V$. The corresponding escape energy $E_{\rm esc}$ depends on the charge of the particle Z:

$$E_{\rm esc} \approx Z \times 3 \times 10^{15} \text{ eV} \tag{1.3}$$

We expect protons to leak out at $\sim 3 \times 10^{15}$ eV, helium nuclei at $\sim 6 \times 10^{15}$ eV, up to iron nuclei ($Z = 26$) at $\sim 8 \times 10^{16}$ eV.

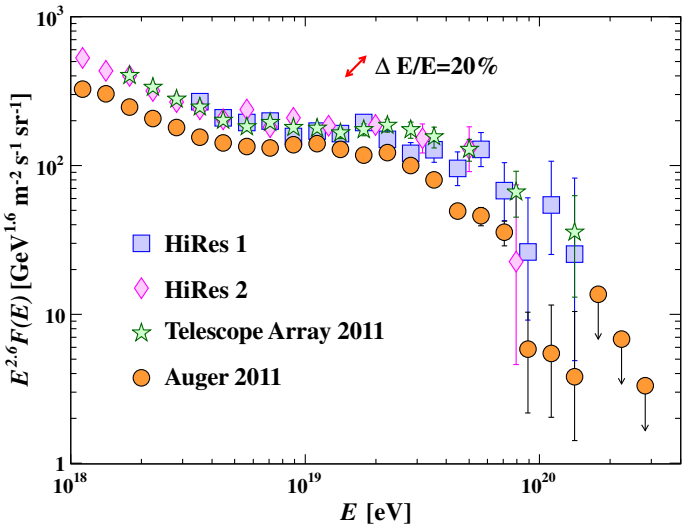

Figure 1.4
The all-particle cosmic ray spectrum above 10 TeV as a function of E (energy-per-nucleus), from air shower measurements. From Beringer et al. (2012, and references therein).

It is interesting to notice how 10^{15} eV is also the order of magnitude of the maximum energy $E_{\max}$ obtainable by particles accelerated in shocks of supernova remnants (SNRs) , supposedly the prime drivers of cosmic ray acceleration (see §1.3). To estimate this maximum energy, we use the following order-of-magnitude argument: the induced electric field by a magnetic field B over a region with scale L moving with velocity U is:

$$\times E = -\frac{KB}{Kt} \rightarrow \frac{E}{L} \sim \frac{B}{L/U} \rightarrow E \sim BU \tag{1.4}$$

So the maximum energy acquired by the particle is linearly proportional to these quantities, as well as the electric charge:

$$E_{\max} = ZeBUL \tag{1.5}$$

where B is the magnetic field flux density around the shock front, $U \sim 10^7$ m/s is the shock speed and $L \sim U \times 10^3$ years $\sim 10^{17}$ m is its scale-length. This would lead to a maximum energy of $\sim Z \times 3 \times 10^{14}$ eV, when considering the magnetic field flux density of the shock region to be that of the interstellar medium $\sim 10^{-10}$ T (Lagage and Cesarsky, 1983). From the discovery of very narrow X-ray filaments (VHk et al., 2005) in the shock regions of supernova remnants it is known that the magnetic flux density can be up to two or three orders of magnitude higher, from $\sim 10^{-10}$ T to $\sim 10^{-8}$ T; with these values the above equation predicts $E_{max} \sim Z \times 10^{16}$ eV not far from the results obtained with more detailed modelling (Berezhko, 1996).
In the above calculations the limiting energy both for acceleration and escape depends on Z. This means that the cosmic ray composition at the knee and beyond

should become heavier as the lighter species are less efficiently accelerated and more efficiently lost. The soft ($\alpha \sim 3$) spectrum measured between the 10^{15} and 10^{17} eV should be due to the superposition of the spectral cut-offs of individual particle species, each one of them found at increasing energies, as can be seen in Fig. 1.5. Some recent experiments sensitive in this energy region such as KASCADE (Antoni et al., 2005; Apel et al., 2009) have confirmed this prediction, while others, such as the Tibet Array, have (Amenomori et al., 2011), found a dominance of heavy nuclei around the knee. The discrepancy could be attributed to model dependence, or to the different kinematic regions explored (Castellina and Donato, 2011).

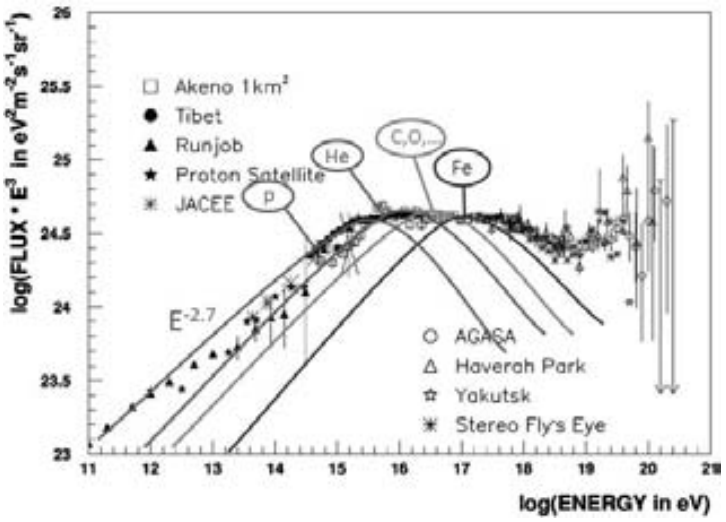

Figure 1.5
Cosmic ray differential energy spectrum multiplied by E^3, showing how the superposition of the energy spectra of different particle species could give rise to the soft region between the "knee" and the "ankle". From Longair (2011, and references therein).

At energies above 10^{18} eV measurements of spectrum of cosmic rays start to be challenging due to the rapidly falling flux intensities, requiring detectors with a huge effective area, such as large ground arrays, fluorescence detectors (such as HiRes, Abbasi et al., 2005) or hybrid detectors such as AUGER (Abraham et al., 2004). Following the assumption that this is the region of transition between galactic and extra galactic cosmic rays the "ankle" can be seen as the result of the intersection between the steep end of the galactic cosmic rays spectrum and a flatter extragalactic one (the "ankle model" by Hillas, 2005). The spectral index of the latter is required to be 2.2 2.5 to explain the dip observed at $\sim 10^{19}$ eV (Fig. 1.4); those values are broadly compatible with those predicted by Fermi acceleration at shocks. A problem with this model is the requirement of acceleration of galactic cosmic rays one order of magnitude above the iron knee, up to 10^{18} eV. Other models offer different scenarios, e.g. in the "dip model" the transition starts at the "second knee" (see Unger, 2008, for a review). The matter is not settled yet, the key discriminating factor being a precise determination of particle composition, which is challenging for these types of detectors at these energies.

At the ultra-high energy (UHE) end ($E > 10^{18}$ eV) of the cosmic ray spectrum, recent measurements (Abreu et al., 2011) seem to confirm the rapid steepening of the

spectrum (GZK cutoff) above 5×10^{19} eV due to the onset of inelastic interactions of UHE cosmic rays with the cosmic microwave background, as predicted by Greisen (1966); Zatsepin and Kuz'min (1966).

The spectrum of cosmic ray electrons and positrons above few GeV is can be described by a power law function (Webber, 1983):

$$I_N(E) \approx 7 \times 10^2 \left(\frac{E}{1\,\mathrm{GeV}}\right)^{-3.3} \frac{\text{leptons}}{\mathrm{m}^2\ \mathrm{s\ sr\ GeV}} \tag{1.6}$$

This spectrum is significantly steeper than the one found for protons and nuclei, but probably does not reflect the injected electron spectrum at the sources. It is in fact suspected that high energy electrons lose energy inside the galaxy emitting synchrotron radiation in radio wavelengths: measurements up to few GHz of the galactic radio emission extrapolate well to the predicted radio emission of > 10 GeV electrons. A minor departure of the spectrum from the power-law behaviour above 70 GeV was observed, (Abdo et al., 2009a; Borla Tridon, 2011), followed by a steepening above 600 GeV (Aharonian et al., 2008), possibly indicating the presence of an excess between 100 and 400 GeV. Furthermore, the positron fraction $R = e^+/e^-$ recently measured with high precision between 1.5 and 100 GeV by the PAMELA experiment (Adriani et al., 2009b,a). was found to change slope at about 10 GeV and increase steadily up to 100 GeV, from $R = 0.05$ to $R = 0.1$ in this energy range, in disagreement with the predictions of current models, where a decrease is instead expected. These measurements are to date not fully understood and various physical interpretations were proposed, including modified supernova remnant models for the $e^\pm$ background, new astrophysical sources, and new physics (see Fan et al., 2010, for a review).

Figure 1.8
Cosmic $e^\pm$ spectrum and e^+/e^- ratio.
a) From Fan et al. (2010) and references therein;
b) From Borla Tridon (2011) and references therein.

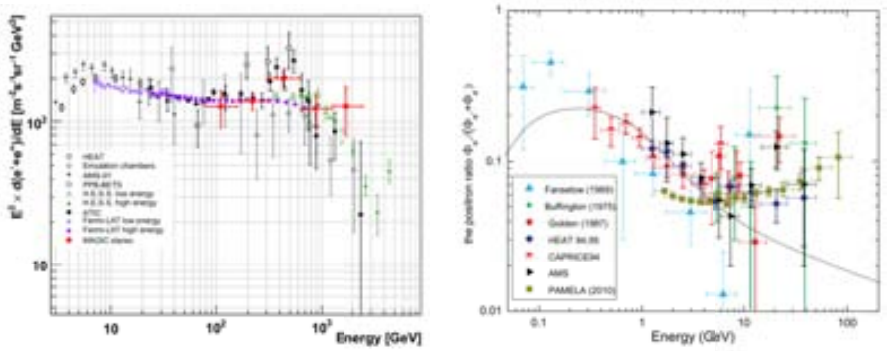

(a) Differential energy spectrum of cosmic ray electrons and positrons multiplied by E^3.

(b) Measurements of the positron fraction up to ~ 100 GeV.

Energy density and isotropy of cosmic rays

The energy density ρ_E of cosmic rays in deep space (i.e. outside the heliosphere) is calculated to be about 1 MeV/m^3, about three orders of magnitude lower than that of solar particles causing auroras. This lead to early speculations about supernova remnants being the main sources of cosmic rays, based on the following energetic argument due to Ginzburg and Syrovatskii (1964): assuming that the cosmic ray energy density $\rho_E \sim 1$ MeV/m^3 is uniform throughout the galaxy, and knowing that the mean lifetime of a cosmic ray particle inside it is $\tau \sim 10^7$ years (see following section), the power required to sustain their acceleration is:

$$P_{CR} = \frac{\rho_E \pi D R^2}{\tau} \sim 10^{34} \text{ W}$$

where $D \sim 1$ kpc is the thickness and $R \sim 15$ kpc is the radius of our galaxy.
This is about 10% of the power output of supernovas in a galaxy: a single supernova event has typically an energy of $E_{SN} \sim 10^{44}$ J (Arnett, 1996) and the supernova rate in a galaxy is estimated to be about three per century, so their power input is $P_{SN} \sim 10^{35}$ W
The value of ρ_E is also comparable to the energy density of starlight (0.6 MeV m^{-3}), cosmic microwave background (0.26 MeV m^{-3}), and the galactic magnetic field (if its magnitude $B = 0.3$ nT, its energy density is $\rho_B = B^2/2\mu_0 = 0.25$ MeV m^{-3}). The energy equipartition indicates that the bulk of cosmic rays in the interstellar space is in equilibrium with these interstellar electromagnetic fields. Furthermore, the almost perfect isotropy of their arrival direction measured at most energies (Abdo et al., 2009b; Zhou and The Tibet ASγ Collaboration, 2010; Abbasi et al., 2010a) is a sign that diffusive propagation in the galactic magnetic field takes place. Only at few TeV a small ($\sim 10^{-3}$) anisotropy is found, possibly due to nearby sources.

Composition of cosmic rays

All cosmic rays measured at the top of the atmosphere consist of stable charged particles and nuclei with lifetimes of order 10^6 years or longer (Beringer et al., 2012). At GeV energies, about 98% are nuclei, the remaining 2% electrons and positrons; the nuclear component consist of 87% protons, 12% helium, 1 % heavier nuclei (Simpson, 1983).
Between 100 GeV and 100 TeV, about 79% of the primary nuclei are protons and about 70% of the rest are helium. The fractions of the primary nuclei are nearly constant over this energy range (Beringer et al., 2012), see Fig. 1.10. In the PeV range, recent evidence suggests that the fraction of the nuclei heavier than helium is greater than 70% (Amenomori et al., 2011). At ultra high energies (E 1 EeV) uncertainties on the behaviour of the proton cross section make it difficult to extract the relative composition of cosmic rays: there are conflicting experimental results on the average mass of primary cosmic-rays getting lighter (Abbasi et al., 2010b) or heavier (Hooper and Taylor, 2010) above $10^{18} - 10^{19}$ eV. It is common to distinguish between

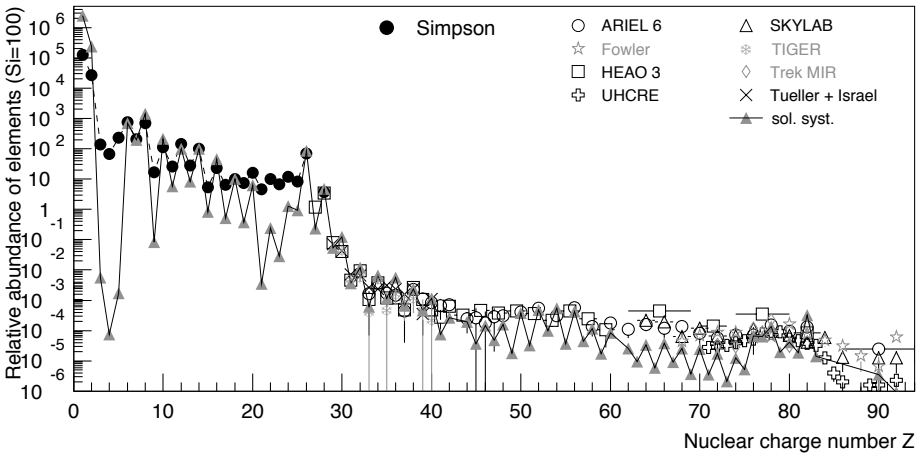

Figure 1.9
Collection of measurement of cosmic ray relative chemical abundaces at energies around 1 GeV per nucleon, normalized to Si = 100, compared to the ones found in the solar system. From BlXmer et al. (2009), and references therein. Discrepancies are found for light elements such as Li, Be, B, and for some heavier odd-numbered elements.

"primary" and "secondary" cosmic rays: primary cosmic rays are particles accelerated directly in astrophysical sources, while secondary cosmic rays are byproducts of interactions between the primary cosmic rays and the environment that surrounds their source, the cosmic electromagnetic background, or the interstellar gas. In this picture, gamma rays and neutrinos are considered "secondary" cosmic radiation. One of these interactions is spallation, the fragmentation of a high-energy primary nucleus (e.g., p, He, C, N, O, Fe) when it impinges on cold interstellar matter (mosty Hydrogen), e.g :

$$^{4}\mathrm{He} + \mathrm{p} \rightarrow {}^{3}\mathrm{He} + \mathrm{p} + \mathrm{n}$$
$$^{4}\mathrm{He} + \mathrm{p} \rightarrow {}^{3}\mathrm{H} + \mathrm{p} + \mathrm{p} \rightarrow {}^{3}\mathrm{He} + \mathrm{e}^{-} + \mathrm{p} + \mathrm{p}$$
$$^{12}\mathrm{C} + \mathrm{p} \rightarrow {}^{10}\mathrm{B} + \mathrm{p} + \mathrm{p} + \mathrm{n}$$
$$^{56}\mathrm{Fe} + \mathrm{p} \rightarrow {}^{55}\mathrm{Mn} + \mathrm{p} + \mathrm{p}$$

Nuclear species that are rare in the sources and in the solar system, such as deuterons, Li, Be, B, sub-Fe elements, are found to be more abundant in cosmic rays (see Fig. 1.9). The measurements about their composition provide important informations on the origin, distribution and the propagation of cosmic rays in our galaxy, e.g.:

- measurements of the abundance of radioactive "clock" isotopes such as ^{10}Be in the low energy cosmic radiation imply that the characteristic lifetime τ_{esc} of cosmic rays inside the galaxy is of about 15 million years (Garcia-MuGoz et al., 1975; Yanasak et al., 2001).
- the observed ratio of the abundances of the spallation products to the primaries implies that cosmic rays with energies of about 1 GeV per nucleon traverse a mean free path ⊠ between 50 and 100 kg m^{-2}.
- the observed underabundance (with respect to the solar system average) of elements with first ionization potential greater than 10 eV such as H, He, C,

N, O, S means that their acceleration at the source of is not as efficient, which in turn implies that the source environment is only partially ionized.

- The primary species, have somewhat flatter spectra than the secondary species, as can be seen in Fig. 1.10. This can be interpreted as an energy dependent decrease in lifetime of energetic cosmic rays inside the galayx as $\tau_{\rm esc} \propto E^{-0.6}$, since $\tau_{\rm esc}$ is measured from the ratio of secondary to primary nuclei (Garcia-Munoz et al., 1987; Swordy et al., 1990; Maurin et al., 2002). In the simplest "leaky box" cosmic rays propagation models this implies that that the observed cosmic ray spectrum is softer than the one found in the vicinity of the sources:

  $$\left(\frac{\mathrm{d}N}{\mathrm{d}E}\right)_{\rm obs} = \left(\frac{\mathrm{d}N}{\mathrm{d}E}\right)_{\rm src} \times E^{-0.6}$$

  this result can also be is interpreted differently, as due the contribution of a local component of freshly injected secondaries with low energies, as suggested by the antiproton/proton fraction (Moskalenko et al., 2003).

- In current galactic propagation models the abundance ratio of secondary cosmic rays to their primary progenitors also allows the determination of propagation parameters such as the diffusion coefficient and the size of the diffusion region, especially when considering fast-decaying isotopes (Strong et al., 2007).

- Also *isotopic* abundance ratios are anomalous with respect to the solar system, for example $^{22}\mathrm{Ne}/^{20}\mathrm{Ne}$ is reduced by a factor 4. This suggests that some cosmic rays originate in neutron-rich environments such as the vicinity of *Wolf-Rayet stars*.

Changes in the composition at and above the knee, with a trend towards heavy particle dominance, are expected for the reasons exposed in §1.1.1. However, discrepancies exist between measurements from different experiments, due to the indirect nature of the techinques used at these energies.

Concerning antiprotons, their spectrum shows a clear indication of kinematic suppression (Yamamoto et al., 2007), linked with their secondary nature. Presently there is no evidence of a significant antimatter composition of the primary component of cosmic rays, nor for an excess above 10 GeV similar to that measured for cosmic positrons.

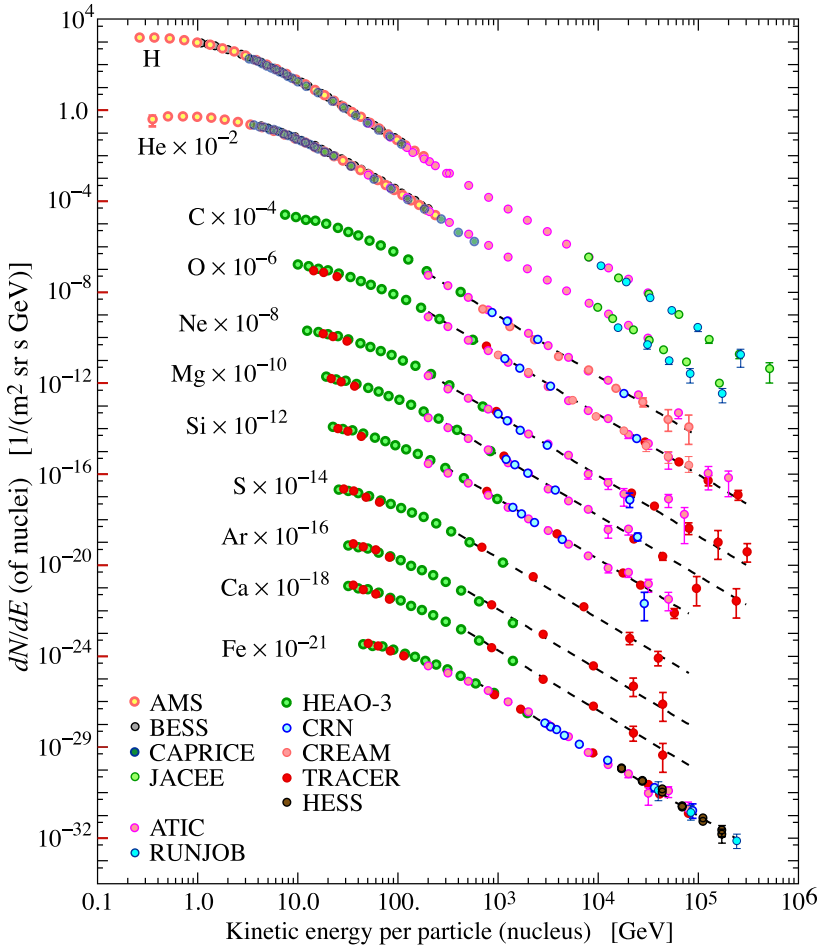

Figure 1.10
Differential energy spectrum of the major components of primary cosmic ray nuclei in the GeV-TeV energy range, from (from Beringer et al., 2012, chapter 24).

1.2 Gamma Rays

Great part of the photons that reach the Earth from the cosmos is of thermal nature, generated in hot objects like stars. The energy of this radiation, even in the most extreme cases, never exceeds a few keV. However, photons of higher energies can only be produced by non-thermal cosmic rays. They account for a minuscule fraction (less than 10^{-6} above 100 GeV) of the flux of charged cosmic rays, as can be seen in Fig. 1.11. However, compared to them, cosmic γ-rays have the advantage of propagating on straight lines throughout the universe: unlike charged particles, which curve due to Lorentz's force in intergalactic, galactic, solar, and planetary magnetic fields.

This characteristic, coupled with the ease of detection, makes them the ideal probe for high energy astrophysics, since γ-rays detected on Earth point back towards sources of non-thermal cosmic ray acceleration and can be used to locate, study and understand it.

The flux of gamma rays is determined by the density of their charged parent particles, and the density of their targets, being them matter, light photons or magnetic fields. So, not only the direction, but also the energy spectrum of gamma rays is closely related to the spectrum of the parent particles. Also, gamma-rays provide

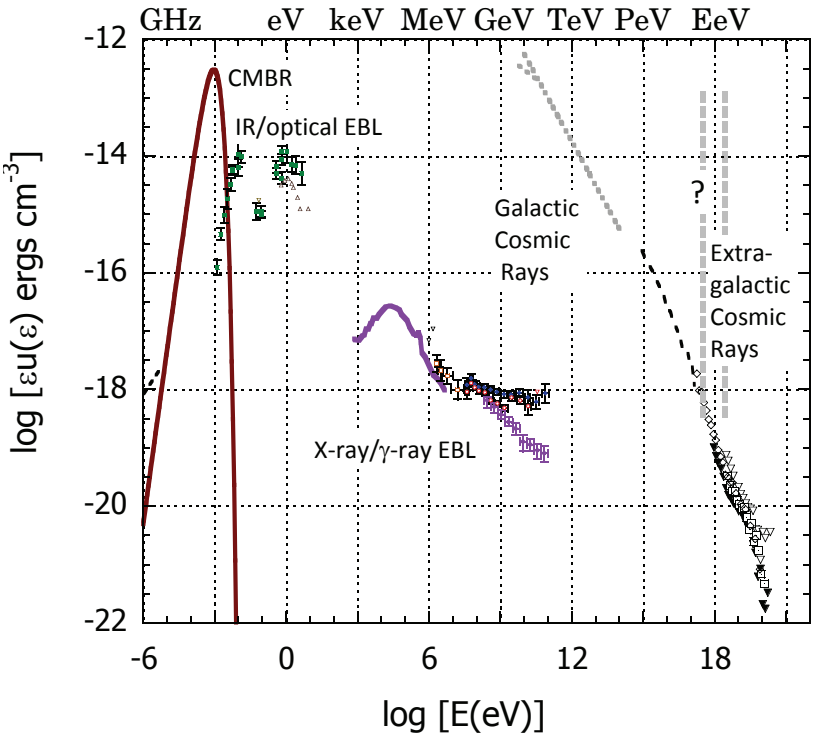

Figure 1.11
Energy density of of photons in intergalactic space and cosmic rays in outer space in the solar cavity near earth. The two datasets with different slopes in the GeV-TeV region come from two different instruments: EGRET and Fermi-LAT. The former measured a higher intensity of extragalactic cosmic rays above ~ 5 GeV, probably due to miscalibration. The question mark corresponds to the knee region in the cosmic ray spectrum, mentioned previously. From Dermer (2012) and references therein.

valuable information on the early stages of the evolution of our universe, in the context of the origin and the evolution of galaxies and large structures. In fact, about a third of the γ-ray sources are active galaxies or quasars located at cosmological

distances. Before reaching the earth, a fraction of the γrays emitted by these distant sources interact along their travel path with ambient photons of the so-called extragalactic background light (EBL), infrared and optical photons of emitted by stars and interstellar dust. The detection this phenomenon in the γ-ray spectrum of distant sources gives insight about the composition and evolution of the radiation fields of the early cosmos. More details about the EBL will be given in §2.2.6.

It is customary to divide the energy spectrum of cosmic γ-rays in three bands, which roughly correspond to the energy ranges of the detection techniques: *so* γ-rays with energies up to ~ 10 MeV and "high-energy" (HE) γ-rays are detected directly by baloon- or satellite-borne detectors, similar to those used in nuclear and particle physics.
Photons with energies above ~ 100 GeV, usually referred to as very high energy (VHE) γ-rays are the domain of ground-based detectors, which use indirect techniques, such as atmospheric Cherenkov imaging.

Detection of cosmic γ-rays

Early detections of cosmic γ-rays were performed serendipitously in the 1960 by military satellites monitoring atomic bomb testings, and since then the interest towards this observational window has never faded. The methods employed for the detection of cosmic γ-rays were originally borrowed from those of nuclear or high-energy particle physics; as the field of astroparticle physics grew in importance many novel ad-hoc techniques were developed, both for ground and space-borne detectors. Presently, two classes of instruments look for gamma rays from the sky: satellite-based detectors, ground-based atmospheric Cherenkov telescopes and direct sampling detectors.

Space-borne γ-ray detector telescopes use many detecting devices common to high-energy particle physics such as counters, spark chambers, calorimeters, silicon trackers, scintillators. Gamma rays interact *directly* with these detectors, whose response can be calibrated in advance using accelerator test beams. Their energy range is limited by their effective area and their size, and presently extends from few MeV to about 300 GeV. At the moment of the writing there are three active fifth-generation γ-ray telescopes orbiting the Earth: INTEGRAL (???), sensitive to low and medium-energy γ-rays up to 10 MeV, the GRID instrument aboard the Italian-built satellite AGILE (Tavani et al., 2008), sensitive beween 30 MeV and 50 GeV and the Fermi Gamma-Ray Space Telescope (Gehrels and Michelson, 1999; Atwood et al., 2009b, FGST, formerly known as GLAST), which hosts two instruments: LAT (sensitive between 100 MeV and 300 GeV) and GBM (sensitive between 8 keV and 40 MeV).

Atmospheric Cherenkov telescopes are essentially large, ground-based reflective dishes made of tessellated mirrors with an imaging photomultiplier camera in the

focus. They image the Cherenkov light emitted by particles in extensive air showers, and reconstruct their arrival direction, a technique known as Imaging Atmospheric Cherenkov Technique (IACT). All the major Cherenkov observatories, in order to obtain better sensitivity, are now using at least two telescopes operated stereoscopic mode. Their energy range is 0.1 - 100 TeV, and they have higher angular resolution than satellite telescopes, but they suffer from a large intrinsic systematic errors in reconstructing the particle energy. More details about the imaging atmospheric Cherenkov technique and telescopes will be given in chapter 3.

Direct sampling detectors are arrays of ground particle detectors covering extensive areas. The detectors themselves can be scintillators, resistive plate counters or water Cherenkov detectors. The latter are large pools of water of tightly spaced arrays of water tanks equipped with photomultipliers. that detect the Cherenkov light produced when cosmic rays travel through the water. Direct sampling detectors offer a method of γ-ray detection with close to 100% duty cycle and very wide (~ 1 steradian) field of view. They are therefore complementary to atmospheric Cherenkov observatories, despite the fact that their point-source sensitivity is currently almost two orders of magnitude poorer. Their background rejection is worse and ther energy threshold higher compared to Cherenkov telescopes, since they need to sample directly the shower particles: all present and future installations will be placed at high altitudes, above 4000 meters above sea level.

Gamma-ray astrophysics

The last 5 years will possibly be remembered as the "golden age" of γ-ray astronomy: the number of detected sources in the energy range between 100 MeV and 10 TeV has skyrocketed, thanks to the contribution of the above-mentioned detectors. In the high-energy γ-ray observational window already more than 1800 sources have been detected (Nolan et al., 2012), most of them associated with active galaxies or of unknown origin. The number of sources detected to emit in VHE γ-rays is around 140 (Wakely and Horan, 2012), but there is room for new discoveries, since the current generation of detectors have not reached fundamental limits yet, and a the planned next generation is expected to bring about a tenfold increase in the number of VHE sources detected.

Sources of γ-rays and cosmic rays

Apart from the already mentioned supernova remnants, a variety of astrophysical sources can be responsible for the acceleration of cosmic rays, not only by means of diffusive shock acceleration.
A well known diagram, proposed by Hillas (1984) in the context of the origin of ultra-high-energy cosmic rays, illustrates well the populations of cosmic ray accelerators in terms of their scale length and their characteristic magnetic field flux density, as

Figure 1.12
High energy and very high energy γ-ray skymaps, in galactic coordinates

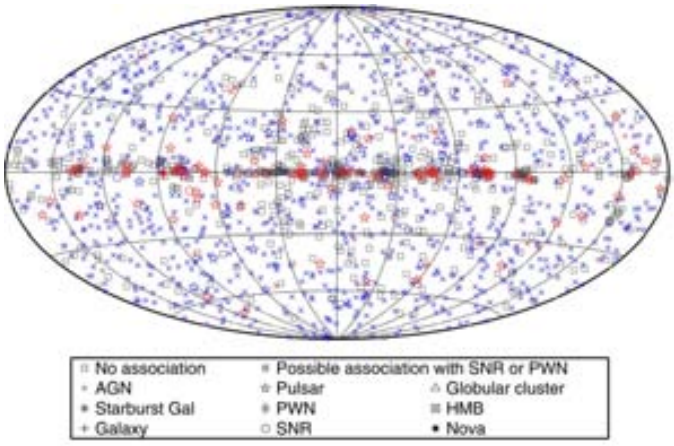

(a) HE γ-ray sources from the Fermi-LAT second catalog (Nolan et al., 2012).

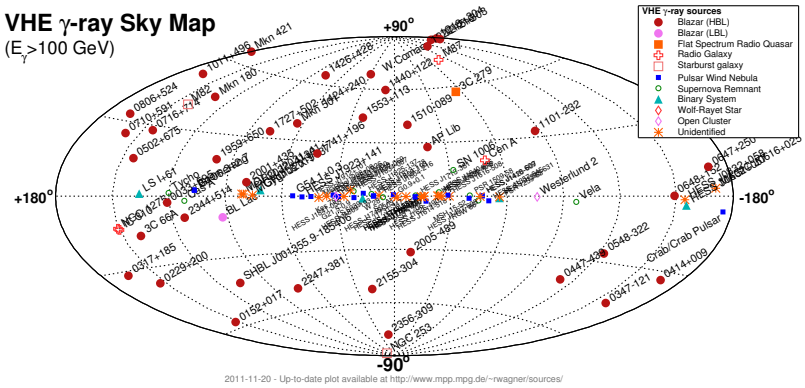

(b) VHE γ-ray sources, image from Wagner (2012)

well as the maximum energy at which particles are accelerated (see Fig. 1.13). The Hillas diagram was initially concieved to support the idea that ultra-high-energy cosmic rays are of extra-galactic origin: all sources close to the 10^{20} eV maximum energy line are indeed extra-galactic. In the following chapters more information will be given about the acceleration mechanisms of two source types relevant for the present thesis: neutron stars and active galactic nuclei. The rest of the sources appearing in Fig. 1.13 is summarized briefly here.

- **Sunspots** are regions of the photosphere of our star that appear darker than the surrounding region. They are a temporary phenomenon caused by intense magnetic activity correlated with the sun 11-year activity cycle. Most solar flares originate in the vicinity of sunspots, their source of energy being the reconnection of magnetic field lines. Particles are accelerated there either through stochastic collisions with the moving plasma, a process similar to the ones described above, or through direct acceleration in electric fields, whose strength can reach ≈ 0.02 V m^{-1} (Hudson and Ryan, 1995; Miller et al.,

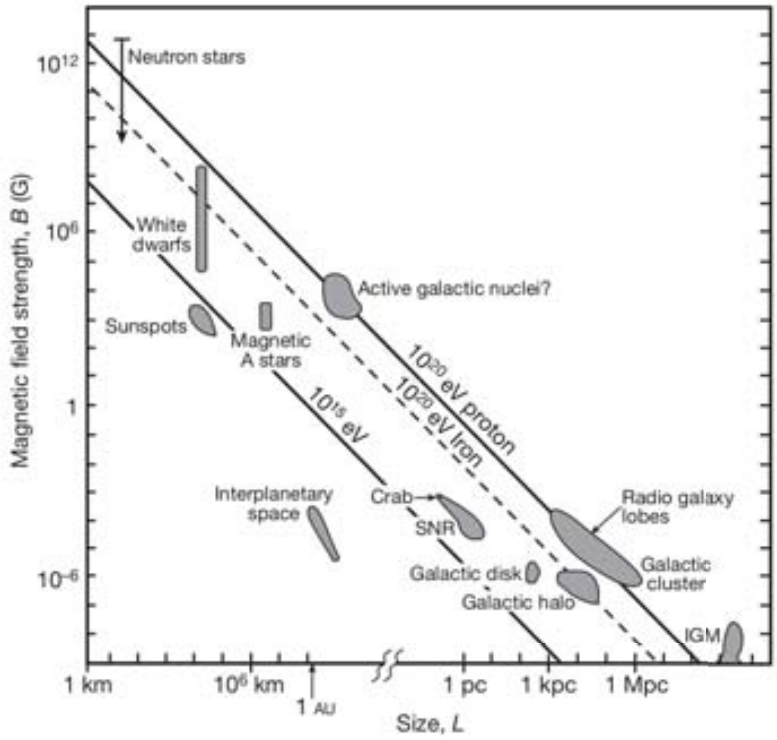

Figure 1.13
The Hillas diagram displays the characteristic magnetic field and scale length of possible sources of high energy and very high energy cosmic rays, and the cosmic rays maximum energy as in (1.5), with $U \sim c$
From Bauleo and Martino (2009).

1997). More complex scenarios, involving magnetohydrodynamic (MHD) turbulences and electron acceleration have also been suggested (Miller, 1998). The accelerated charged particles collide with matter in the atmosphere of the sun and produce (amongst other particles) neutral pions, which in turn decay into high-energy γ-rays. Recently, very bright γ-ray emission from a solar flare was detected by the Fermi-LAT satellite, it lasted about 20 hours with energies up to 4 GeV (Omodei et al., 2012).

- **Supernovae** are violent explosions following the gravitational collapse of a massive star when nuclear fusion in its interior ends, but can also be caused by the accretion of white dwarf stars, in that case are classified as Type Ia. All other types are core-collapse supernovae (Baade and Zwicky, 1934a; Woosley and Janka, 2005, for a recent review), in which the star envelope is ejected at very high velocity during the explosion, with kinetic energies of $\sim 10^{44}$ J. Supernovae can give rise to either neutron stars or black holes, very compact dead stars described in the next paragraph.
  The chief energy output of supernova are actually neutrinos: during the collapse, when the core densities surpass 10^{13} kg m^{-3}, electrons and protons in nuclei fuse into neutrons (neutronization) and a prodigious amount of neutrinos is emitted, accounting for $\sim 10^{46}$ J, or one-tenth of a solar mass. After the supernova explosion of 1987a in the magellanic cloud, few of its neutrinos were detected in several earth laboratories (Bionta et al., 1987; Hirata et al.,

1987; Alexeyev et al., 1988), essentially marking the beginning of neutrino astronomy.
When the progenitor is an extermely massive *population III* star, the energy released during its collapse can be an order of magnitude higher than that of a standard supernova. These explosions, dubbed *hypernovae*, are possibly the cause of some of the observed Gamma Ray Bursts (GRB) .

- **Supernova remnants**, which have been already described in section 1.3 as possible cosmic ray accelerators, are also well-established sources of γ-rays. At present, a strong observational proof is missing that acceleration in SNR can quantitatively account for the observed cosmic ray spectrum, so leptonic production of γ-rays cannot be ruled out. On the contrary, a strong argument in its favor is the observed similarity of the SNR morphology in γ-rays and in X-rays, as the latter trace the presence of high-energy electrons emitting synchrotron radiation. In any case, the complex morphology of the remnants, and the unknown three-dimentional distribution of molecular clouds interacting with the shocks, makes it difficult to draw any firm conclusion, and the two scenario (hadronic and leptonic) are not mutually exclusive.

- **White Dwarfs and Neutron Stars** are the end-stages in the life of stars. White dwarfes are the last stage in the life of stars in the solar mass range, whose nuclear burning doesn't continue beyond carbon. Together with neutron stars they are degenerate stars that display a stable equilibrium configuration between their gravitational force and the degeneracy pressure of electrons and neutrons, respectively. White Dwarfs were first predicted by S. Chandrasekhar in 1931 Chandrasekhar (1931b,c,a), neutron stars were envisioned by L. Landau one year after (Landau, 1932), and correctly predicted by Baade and Zwicky (1934b) after the discovery of the neutron. Due to said equilibrium condition, they all must have a mass smaller than a certain stability limit, known as Chandrasekhar limit, ($\approx$ 1.4 $M_\odot$, for white dwarfs, and $\approx$ 3 $M_\odot$ for neutron stars). Their typical radius is 5000 and 10 km, respectively.
When found in binary systems, if their companion is a main sequence star, white dwarfes are identified with cataclysmic variables and novae. If the companion is a giant star and the white dwarf is embedded in its atmosphere, it is classified as symbiotic star. In both cases matter from the companion star would accrete onto the white dwarf, causing occasional thermonuclear explosions on its surface, which in turn would create strong shocks. Recently, gamma rays at energies above 100 MeV were measured shortly after one such explosions in symbiotic-like nova Cyg 407, an evidence consistent with shock accleration of protons and electrons in the expanding nova shell (Collaboration, 2010). Neutron stars and black holes are the supposed accretors in γ-ray emitting high-mass binary systems such as PSR B1259-63/SS 2883, LSI 61+303, and LS 5039. In these enviroments, characterized by a very high radiation density, particle acceleration can happen in jets produced by accretion onto the

compact object, or in the shocks due to the collision of stellar/neutron star winds. γ-rays are then produced by inverse Compton of accelerated electrons on the very dense photon fields.
Pulsars are highly magnetized, spinning neutron stars, which accelerate electrons in their magnetosphere, and power the surrounding pulsar wind nebulae (PWN). They will be described in more detail in chapter 2.
If the mass is bugger than the Chandrasekhar limit, gravitational collapse is inevitable and the dying star becomes a black hole.

- Black Holes
- Protostellar objects
- Globular Clusters
- Galactic Center
- Galactic lobes
- Extragalactic accelerators

  Active Galactic Nuclei

  Starburst galaxies

  GRBs

1.3 Acceleration processes

In general terms the problem of acceleration of cosmic rays consists in finding plausible processes responsible for the non-thermal power-law spectrum, the extreme energies observed (up to 10^{20} eV), and the measured composition.
Most of the proposed ones have a *bottom-up* hierarchy: thermal particles are injected with low energies and are accelerated via dynamic (collisions of particles with clouds or shocks), hydrodynamic (acceleration of whole layers of plasma at high energy) or electromagnetic (action of electrical forces due to static electric fields or time-varying magnetic fields) mechanisms. *Top-down* models, in which cosmic-rays are produced by decay of very massive, long lived particles predicted by extensions of the standard model are less common, but might be of help in explaining the origin of the cosmic rays with highest energies (Busca et al., 2006). They will not be covered in this work.

γ-rays are instead produced only in the interactions of charged, accelerated particles (electrons/positrons or protons) with ambient matter of fields. The γ-ray production is an energy loss process of cosmic rays, and the production sites reflect the densities of cosmic rays and their "targets". Table 1.1 summarizes the most relevant bottom-up cosmic-ray acceleration and γ-ray production processes, which will be described in the following.

Table 1.1: Cosmic ray and γ-ray production processes

Cosmic Rays	γ-rays
Diff. shock accel.	Inverse Compton scatt.
Fermi accel.	π^0 and nuclear decays
Electric field accel.	Bremsstrahlung
Magnetic field accel.	Synchrotron rad.
	Curvature rad.
	Pair annihlation

Acceleration of cosmic rays

In the previous sections it has already been disclosed that shocks powered by supernova remnants are the most probable source of cosmic rays, through diffusive shock acceleration. In the following, an brief overview is given of this acceleration mechanism, starting from its precursor, the Fermi acceleration mechanism. Other important mechanisms of particle acceleration relevant to this work will be presented in more detail in the following chapters.

Fermi acceleration mechanism is an early theory on cosmic rays acceleration is due to Enrico Fermi (1949). It proposes a dynamical mechanism in which particles collide with clouds in the interstellar medium and are reflected elastically by *magnetic mirrors*, e.g. regions where converging magnetic field lines adiabatically invert the component of the particle momentum parallel to them (see Jackson, 1999, section 12.5). The clouds move randomly,the reflections stochastically increase the energy of the particles, and produce a power-law spectrum.

Let us assume a particle with initial energy E and momentum p hits a magnetic mirror moving at with velocity V at and angle θ to the normal of the mirroring plane. The mass is taken as infinitely large with respect to that of the particle, the center of momentum frame is that of the cloud. Then the energy of the particle in that reference frame is:

$$E' = \gamma_V \left(E + V p \cos\theta\right) \tag{1.7}$$

where $\gamma_V = \left(1 - \beta_V^2\right)^{-1/2}$ and $\beta_V = V/c$.
The component of the momentum is that is reflected is

$$p'_x = p\cos\theta = \gamma_V \left(p\cos\theta + \frac{VE}{c^2}\right) \tag{1.8}$$

In the reflection, $p'_x \to -p'_x$, and the energy is conserved: $E'_{\text{before}} = E'_{\text{a}\boxtimes\text{er}}$. Returning back to the rest reference frame after the shock we have:

$$E'' = \gamma_V \left(E' + V p'_x\right) \tag{1.9}$$

Substituting (1.7) and (1.8) in (1.9), and using $v\cos\theta/c^2 = p_x/E$ we obtain:

$$E'' = \gamma_V E\left[1 + 2\beta_V\frac{v\cos\theta}{c} + \beta_V^2\right] \tag{1.10}$$

expanding to the second order in β_V, the energy gained by the particle in the collision can be written as:

$$\boxtimes E = E'' - E = 2E\beta_V\left[\left(\frac{v\cos\theta}{c}\right) + \beta_V\right] \tag{1.11}$$

In the assumption that particles are isotropically distributed in the rest frame and that they are relativistic ($v/c \sim 1$), the probability of a collision at is proportional to the relative velocity between cloud and particle:

$$P(\cos\theta) \propto (V\cos\theta + v)/(1 + vV\cos\theta/c^2) \approx (1 + \beta_V\cos\theta) \tag{1.12}$$

As we can see, head-on collisions ($\cos\theta = 1$) are slightly more common than tail collisions ($\cos\theta = -1$) for the same reason that running in the rain gets you wetter in the front than in the back.
We can then average the first term of (1.11) over the incident angle $x = \cos\theta$ and calculate the average energy gain from every collision:

$$\left\langle\frac{\boxtimes E}{E}\right\rangle = 2\beta_V\frac{\int_{-1}^{1} x\,(1+\beta_V x)\,\mathrm{d}x}{\int_{-1}^{1}(1+\beta_V x)\,\mathrm{d}x} + 2\beta_V^2 = \frac{8}{3}\beta_V^2 \tag{1.13}$$

This results shows that the energy gain, as originally envisioned by Fermi, is only *second order* in β_V.
We proceed further to illustrate how a power-law spectrum can be obtained.
After every collision, the energy of a particle can be written as $E_i = \boxtimes E_{i-1}$, with $\boxtimes = 1 + \frac{8}{3}\beta_V^2$. Then, after k steps, the energy can be written $E_k = E_0\boxtimes^k$. If P is the probabilty that the particle remains within the collision region, then at the k-th step the particles remaining there are $N_k = P^k N_0$, and k :

$$\frac{\ln(N_k/N_0)}{\ln(E_k/E_0)} = \frac{\ln P}{\ln\boxtimes} \tag{1.14}$$

we can write N_k as the number of particles $N(\quad E)$ with energies equal or greater than $E = E_k$ since a fraction P of them will be accelerated further in their next collision. So we obtain the *integral* energy spectrum:

$$\left(\frac{N(\quad E)}{N_0}\right) = \left(\frac{E}{E_0}\right)^{\ln P/\ln\boxtimes} \tag{1.15}$$

and differentiating:

$$N(E)\mathrm{d}E \propto E^{-1+\ln P/\ln\boxtimes}\mathrm{d}E \tag{1.16}$$

which is the differential spectrum with the required power-law form.
A more complete derivation of the spectrum can be found in (Longair, 2011, section 17.4).

The original Fermi process we just illustrated has at some disadvantages: First, it is very slow: $\beta_V \ll 1$ even in supernova remnants, where $V \sim 10^7$ m/s; second, the spectral index in (1.16) can in principle assume *any* value, while the cosmic ray spectrum has indices between 2.5 and 3 (see section 1.1.1); third, the ionization energy loss rate (important at for particles injected at low energies) must be smaller than the energy gain rate in collisions. This *injection problem* is shared by other *bottom-up* processes.

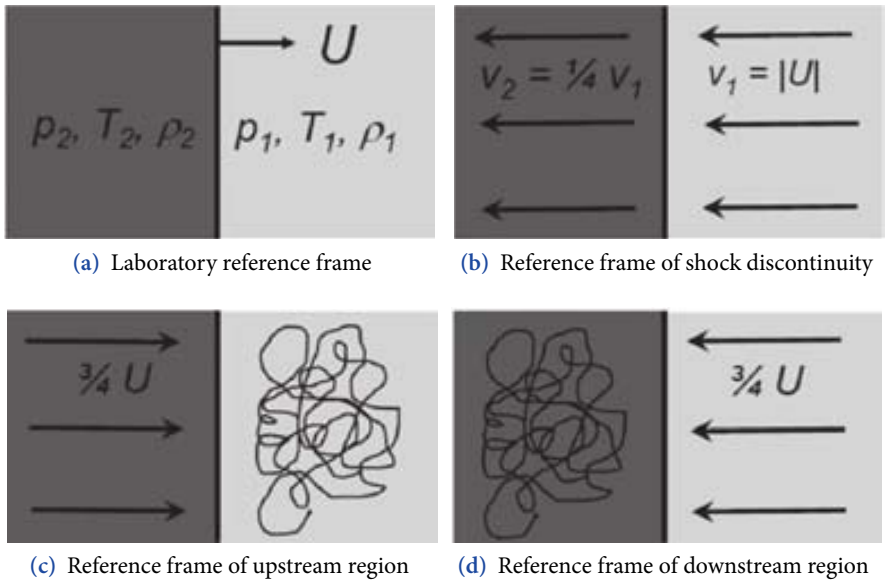

(a) Laboratory reference frame (b) Reference frame of shock discontinuity

(c) Reference frame of upstream region (d) Reference frame of downstream region

Figure 1.14
Scheme of the diffusive shock acceleration mechanism. The shock moves from left to right. The region upstream from the shock is light grey, the downstream one dark grey. Further explanations are found in the text.
From (Longair, 2011).

Diffusive shock acceleration These problems were addressed by the theory of diffusive shock acceleration (Axford et al., 1977; Krymskii, 1977; Bell, 1978; Blandford and Ostriker, 1978) in the late seventies, a *first order* Fermi process. Good descriptions of it can be found in (Vietri, 2008; Longair, 2011). The general idea is the following: a strong shock moving with speed U is surrounded with two distinct regions, one ahead of the shock (upstream) with pressure p_1, temperature T_1 and density ρ_1 and the other downstream the shock with p_2, T_2, and ρ_2 (Fig. 1.14a). In the shock reference frame, the speed of upstream particles hitting it is $v_1 = U$, is slowed down in the downstream region to v_2. The ratio $v_1/v_2 = 4$ can be calculated from continuity equation assuming fully ionised gas (Fig. 1.14b). In analogy to the collisions with a cloud in the original Fermi mechanism, particles coming from the upstream region are reflected and gain energy when crossing the shock, but the averaging done in equation 1.13 above must be carried on only for $x = \cos\theta > 0$, since they are entering the downstream region on one side only of the shock (Fig. 1.14c). Therefore

the average energy gain per particle is $\langle \boxtimes E/E \rangle \propto U/c$: a first order process.
The velocity of the particles is later isotropized in the downstream region, effectively re-creating the same situation: some particles can cross again upstream. This time, in the downstream reference frame (Fig. 1.14d), the upstream particles move at a speed $v_1 - v_2 = 3/4U = V$. The particles that cross from downstream back to upstream still gain energy, and the gain is proportional to $\beta_V = V/c$ as before. In the upstream side, the streaming of particles from the downstream of the shock into the unperturbed interstellar medium generates Alv"n waves, which grow generate turbulent motions responsible of the said isotropization of particle velocities in the regions both ahead and behind the shock.

It can be shown (Bell, 1978) that the energy gain of a full cycle is:

$$\langle \frac{\boxtimes E}{E} \rangle = \frac{4}{3}\beta_V \tag{1.17}$$

and $\boxtimes = 1 + \frac{4}{3}\beta_V$.
To work out the probability that the particle P crosses the shock again, we notice that the average flux of particles crossing the shock in either direction is $\boxtimes_{\text{in}} = \frac{1}{4}\rho_N c$, where ρ_N is the number density of particles in the shock region. The particles in the downstream region are advected from the shock with a flux $\boxtimes_{\text{out}} = \frac{1}{4}\rho_N U = \frac{1}{3}\rho_N V$. Then the fraction of particles remaining within the the shock region is $P = 1 - \boxtimes_{\text{out}}/\boxtimes_{\text{in}} = \frac{4}{3}\beta_V$.
Assuming a non-relativistic shock $\beta_V \ll 1$, we can write $\ln \boxtimes = \ln(1 + \beta_V) \approx \beta_V$ and $\ln P = \ln(1 - \beta_V) \approx -\beta_V$, therefore $\frac{\ln P}{\ln \boxtimes} = -1$ and the differential energy spectrum in equation 1.16 becomes

$$N(E)\mathrm{d}E \propto E^{-2}\mathrm{d}E \tag{1.18}$$

This mechanism shows that a power-law spectrum with an fixed index can be obtained in a variety of sources, provided that strong shocks are present. One might object that the value of 2 for the spectral index calculated is different than what is experimentally measured (around 2.7), but several further adjustments to this classic theory can account for an index $\alpha > 2$: a steepening of the spectrum could be due to lower velocity ratios, since $r = v_1/v_2 < 4$ implies $\alpha = \frac{r+2}{r-1} > 2$, or if P was energy dependent (as suggested by the differences in spallation spectrum in secondaries seen in Fig. 1.10). Further possibilities have been investigated (Ballard and Heavens, 1992, e.g.).

Simulations show that diffusive shocks acceleration process in supernova remnants is extremely efficient, up to 60% (Kang and Jones, 2006), so much in fact that the energy density of the accelerated particles influences the shock itself resulting in a intrinsically non-linear picture. The particles gives rise to Alfv"n waves and turbulences, that enhance greatly the strenght of the magnetic field, causing their acceleration up to "knee" energies.

Acceleration by electric and magnetic fields A charged particle can accelerated very efficiently by a static electric field, however such condition is not usually found in astrophysical objects. An exception are pulsars: their spinning magnetic field gives rise to charge separation in some regions of their magnetosphere. Their physics will be described in much more detail in chapter 2.

Another electromagnetic phenomenon that can accelerate charges at very high energies (up to 10^{21} eV for protons) is low frequency dipole radiation, an early model for cosmic-ray acceleration in pulsar winds, formulated by Gunn and Ostriker (1969) soon after the discovery of the Crab pulsar. Qualitatively, one can assume that at large distances from the pulsar an spherical electromagnetic wave of frequency Ω is present, with the electrical field **E** and the magnetic field **B** perpendicular to each other and to the radial direction z. Solving the relativistic equations of motion $\frac{\mathrm{d}v^\mu}{\mathrm{d}\tau} = \frac{e}{m_e c} F_{\mu\nu} v^\nu$ for a particle initially at rest at the *light cylinder radius* $r_{\rm LC} = c/\Omega$ results in a net acceleration along z (see Fig. 1.15) proportional to $\omega_{\rm LC}/\Omega$, with $\omega_{\rm LC} = eB/(mc)$ being the electron gyrofrequency in a magnetic field of intensity B at the light cylinder radius. For young pulsars like the Crab, $\omega_{\rm LC}/\Omega \sim 10^8$, assuring an acceleration so rapid that the phase of the accelerated particles is practically constant. This mechanism can happen only in the vicinity of $r_{\rm LC}$ though, since the energy lost in accelerating particles and the $1/r$ behaviour of $|B|$ and $|E|$ brings about a rapid decay of the wave. Also, the above reasoning is valid only if particles follow vacuum-field trajectories, a condition met if $\gamma_{\rm LC}\omega_{\rm LC}\Omega > \omega_p^2$, where $\gamma_{\rm LC}$ is the Lorenz factor of target particles and ω_p is the plasma frequency at the light cylinder radius. Even if the above condition is not met, the energetics of pulsar wind nebulae require the Poynting energy flux $\mathbf{E} \times \mathbf{B}$ to be transferred somehow to the particle wind by analogous mechanisms.

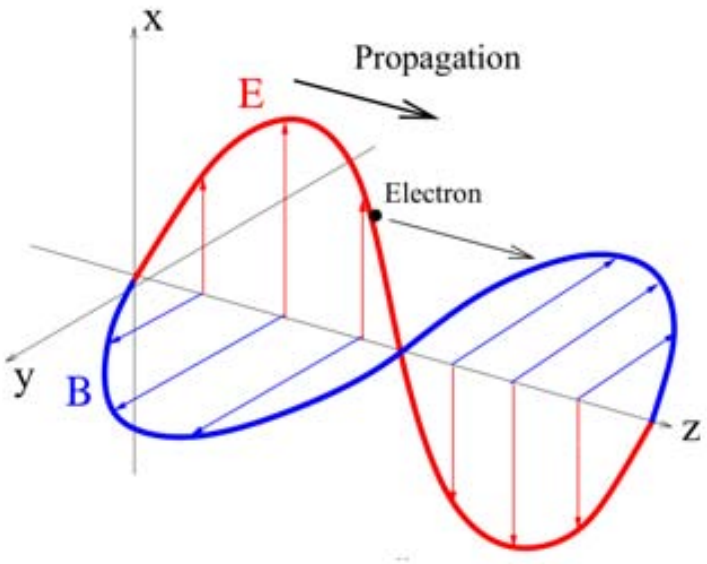

Figure 1.15
Sketch depicting the acceleration of a charge by a low-frequency electromagnetic wave. Courtesy of T. Saito.

Production of γ-rays

Compton scattering is the scattering between a photon and an electron:

$$\gamma + e^- \rightarrow \gamma + e^-$$

Observed in the frame of reference in which the electron is at rest, the photon transfers energy to the electron and the process is known as *direct* Compton scattering, otherwise, in the reference frame in which the electron is moving, the electron transfers energy to the photon and the process is called *inverse* Compton scattering. The former is the relativistic boosted version of the latter.
In classic electrodynamics, the elastic scattering of an electromagnetic wave of frequency on an electron is described by the Thomson differential cross-section:

$$\frac{\mathrm{d}\sigma_T}{\mathrm{d}\Omega} = \frac{3}{16\pi}\sigma_T \quad 1 + \cos^2\theta \tag{1.19}$$

where $\sigma_T = 8\pi r_e^2/3 \approx 6.65 \times 10^{-29}$ m^2 is the *integral* Thomson cross-section and θ is the scattering angle between the incident and scattered wave.
Taking into account the fact that photons posses a momentum h/c and an energy $\varepsilon = h$, the energy of the scattered photon ε_1 can be written:

$$\varepsilon_1 = m_e c^2 \frac{x}{1 + x(1 - \cos\theta)} \tag{1.20}$$

where $x = \varepsilon/m_e c^2$. Scatterings at $\theta = 0$ are elastic, but in general the interaction is not elastic anymore: $\theta \quad 0 \rightarrow \varepsilon_1 \quad \varepsilon$. If a very energetic photons ($x \quad 1$) is reflected ($\theta = \pi$), all of its energy but $m_e c^2/2 \sim 256$ keV is transferred to the electron.
Equation 1.19 is the classical limit of the more general Klein-Nishina differential cross section, which takes into account the quantum kinematic effects mentioned above:

$$\frac{\mathrm{d}\sigma_{KN}}{\mathrm{d}\Omega} = \frac{3}{16\pi} \frac{\sigma_T}{1 + x(1 - \cos\theta)^{\ 2}} \quad x(1 - \cos\theta) + \frac{1}{1 + x(1 - \cos\theta)} + \cos^2\theta \tag{1.21}$$

The *integral* Klein-Nishina cross section σ_{KN} can be obtained integrating (1.21) over the solid angle Ω. The asymptotic limits of σ_{KN} are:

$$\sigma_{KN} \simeq \begin{array}{ll} \sigma_T \quad 1 - 2x + \frac{26}{5}x^2 + & \text{if } x \ll 1 \text{ (Thomson regime)} \\ \frac{3}{8}\sigma_T x^{-1} \quad \ln 2x + \frac{1}{2} & \text{if } x \quad 1 \text{ (Klein-Nishina regime)} \end{array} \tag{1.22}$$

The effects of direct Compton scattering are suppressed for very energetic photons, due to the x^{-1} dependency of σ_{KN} found in the Klein-Nishina regime.
Inverse Compton scattering on the other hand is a very relevant process in high energy astrophysics, especially in the context of the production of high-energy γ-rays in environments with high photon density.

An incoming relativistic electron with Lorenz factor γ scatters on a photon of energy $\varepsilon = h\nu_\gamma$, increasing its energy by a factor $\sim \gamma^2$, provided that the scattering in the rest frame of the electron is in the Thomson regime ($\gamma\varepsilon \ll m_e c^2$). In this process the energy of the ambient photon $E_{\rm IC}$ can be increased by a factor γ^2. It is therfore the most important high-energy γ-ray emission process in the cosmos.

In a more general case, when the energy transfer in the rest frame of the electron cannot be neglected, the power transferred by the electron to an isotropic distribution of photons is (Blumenthal and Gould, 1970):

$$\langle P\rangle_{\rm IC,T} = -\left(\frac{{\rm d}E}{{\rm d}t}\right)_{\rm IC,T} = \frac{4}{3}\sigma_T c\beta^2\gamma^2 U_{\rm ph}\ \ 1 - \frac{63}{10}\frac{\langle\varepsilon^2\rangle}{m_e c^2\langle\varepsilon\rangle} + \tag{1.23}$$

where $U_{\rm ph}$ is the initial photon energy density, and $\langle\gamma\varepsilon\rangle$, $\langle\gamma\varepsilon^2\rangle$ are the mean and mean-squared photon densities.

In the Thomson regime, the characteristic inverse Compton cooling time is:

$$t_{\rm IC,T} = \frac{E}{\langle P\rangle_{\rm IC,T}} \sim \frac{3m_e c^2}{4\sigma_T c\beta^2\gamma^2 U_{\rm ph}}. \tag{1.24}$$

For the Klein-Nishina case the energy loss rate is instead:

$$\langle P\rangle_{\rm IC,KN} = -\left(\frac{{\rm d}E}{{\rm d}t}\right)_{\rm IC,KN} = \pi r_e^2 m_e^2 c^5 \int \frac{n(\varepsilon)}{\varepsilon}\left(\ln\frac{4\varepsilon\gamma}{m_e c^2} - \frac{11}{6}\right){\rm d}\varepsilon, \tag{1.25}$$

and the corresponding cooling time is longer.

In the case of relativistic electrons impinging on a monochromatic population of seed photons whose frequency is ν_0, the inverse Compton radiation emissivity is given by (see Blumenthal and Gould, 1970, for an exact derivation):

$$j(\nu)_{\rm IC} = \frac{m_e c^2 n_e \sigma_T I_0}{4\gamma^2 h\nu_0}\frac{(1+\beta)}{\beta^2}F_{\rm IC}(\nu) \tag{1.26}$$

where:

$$F_{\rm IC}(\nu) = \begin{array}{ll} \frac{\nu}{\nu_0}\ \ \frac{\nu}{\nu_0} - \frac{1}{1+\nu^2\gamma^2} & \text{if}\quad \frac{1}{1+\nu^2\gamma^2} < \frac{\nu}{\nu_0} < 1 \qquad \text{(downscattering)} \\ \frac{\nu}{\nu_0}\ \ 1 - \frac{\nu}{\nu_0}\frac{1}{1+\nu^2\gamma^2} & \text{if}\quad 1 < \frac{\nu}{\nu_0} < (1+\beta)^2\gamma^2 \qquad \text{(upscattering)} \end{array} \tag{1.27}$$

As can be seen in Fig. 1.16, in the case of downscattering $F_{\rm IC}(\nu) \propto \nu^2$, while in the case of upscattering $F_{\rm IC}(\nu) \propto \nu$, except for frequencies close to the maximum ones.

The average frequency of the photons can be calculated averaging $F_{\rm IC}(\nu)/\nu$, and it is:

$$\langle\nu\rangle = \frac{4}{3}\gamma^2\nu_0 \tag{1.28}$$

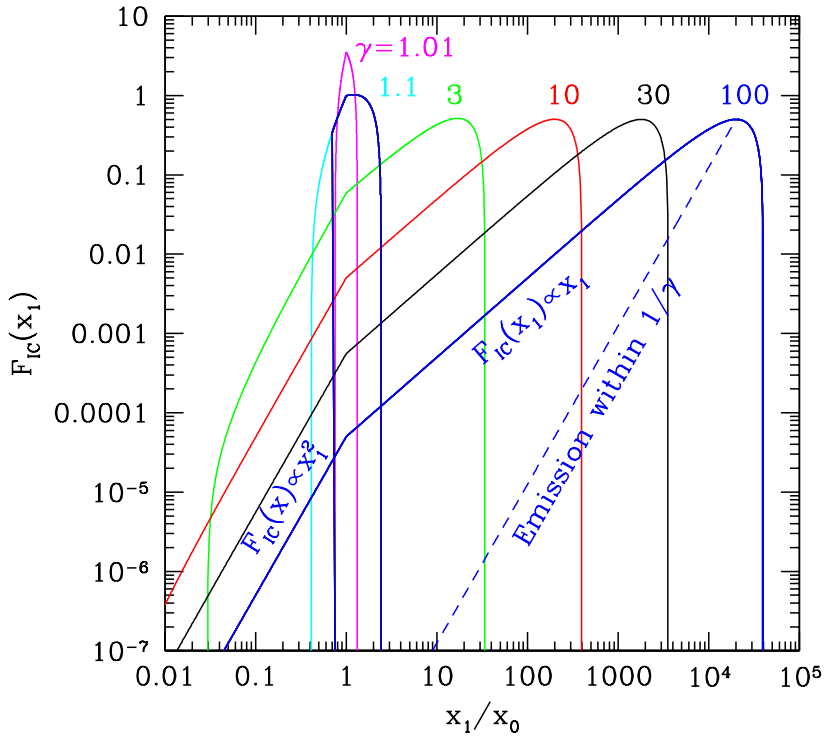

Figure 1.1 The function $F_{IC}(x)$, which describes the emissivity of the single electron inverse Compton emission (equation 1.27). From Ghisellini (2012). In the image, x_1/x_0 correspond to ν/ν_0 in the text, and the dashed line corresponds to amount of radiation emitted within the $1/\gamma$ aperture beaming cone, which always amounts to 75% of the total power, for any γ.

When the electron population is isotropically distributed and has an power-law spectrum with spectral index p:

$$n(E)\mathrm{d}E = KE^{-p}\mathrm{d}E \text{ for } E_{\min} < E < E_{\max},$$

with $n(E)$ the number density as a function of the energy and K a normalization constant, the resulting inverse Compton radiation has an emissivity:

$$J_{IC} = Q(p)\sigma_T c K \frac{U_{ph}}{h\nu_0}\left(\frac{\nu}{\nu_0}\right)^{-(p-1)/2}, \tag{1.29}$$

where $Q(p)$ is a dimensionless function of p.

The relevant relations in equation 1.48 are (setting $\alpha = (p-1)/2$): $J_{IC}(\nu) \propto K U_{ph} \nu^{-\alpha}$. The radiation has a power-law spectrum.

This result is valid for a limited range of photon energies. If $E_{\min} = \gamma_{\min} m_e c^2$ and $E_{\max} = \gamma_{\max} m_e c^2$, from relation 1.28 it can be seen that the energy spectrum does not extend much beyond $(4/3)\gamma_{\max}^2 h\nu_0$ and below $(4/3)\gamma_{\min}^2 h\nu_0$.

If the spectrum of the seed photons is not monochromatic, but has an frequency-dependent energy density $U_{ph}(\nu)$, equation 1.29 becomes (here we indicate the Compton frequency as ν_c:

$$J_{IC} = Q(p)\sigma_T c K \nu^{-\alpha} \int_{\nu_{\min}}^{\nu_{\max}} \frac{U_{ph}(\nu')}{\nu'} \nu'^{\alpha} \mathrm{d}\nu'. \tag{1.30}$$

$\nu_{\rm min}$ and $\nu_{\rm min}$, the target photon frequencies put as limits of the integration, in general depend on the observed Compton frequency ν_c, the target photon limiting frequencies ν_1 and ν_2 and the electron limiting Lorentz factors $\gamma_{\rm min}$ and $\gamma_{\rm max}$:

$$\nu_{\rm min} = \max(\nu_1, \frac{3\nu_c}{4\gamma_{\rm max}^2} \tag{1.31}$$

$$\nu_{\rm max} = \min(\nu_2, \frac{3\nu_c}{4\gamma_{\rm min}^2} \tag{1.32}$$

$$\tag{1.33}$$

In the case that the spectrum of the photons comes from synchrotron radiation, $U_{\rm ph}(\nu') \propto \nu'^{alpha}$, and the integral would depend on $\ln(\nu_{\rm min}/\nu_{\rm min})$.

One photons can suffer multiple scatterings, and this can change the inverse Compton spectrum of a source significantly. This process is called "Comptonization", and will not be covered here (the classical paper by Pozdnyakov et al., 1983, offers a detailed treatment of the problem and insights on its relevance in high energy astrophysics). Suffice it to say that the effect on the spectrum is relevant when the Comptonization parameter y, defined as the average number of scatterings times the average energy gain per scattering, is greater than one. In that case, even a population of thermal electrons (distributed as a Maxwellian or any similarily peaked function) can give rise to radiative emission with a power-law spectrum.

π^0 and nuclear decay are the most relevant hadron decays of astrophysical relevance that emit γ-rays. The neutral pion decays into gamma-rays through its two most frequent decay channels, whose branching ratios add up to 99.997%:

$$\pi_0 \rightarrow \gamma + \gamma$$
$$\pi^0 \rightarrow e^- + e^+ + \gamma.$$

Neutral pions are formed in hadronic collisions between two cosmic rays (protons or α particles) or via photo-pion production ($p + \gamma \rightarrow \nu^+ \rightarrow p + \pi^0$) by very high energy protons. They have rest mass of 135 MeV/c^2 and a decay lifetime of 8 × 10⁻17 s. The decays of strange barions into γ-rays (e.g. $\nu^0 \rightarrow \nu + \gamma$) also play a role. The bound states in the nucleus have energies in the MeV range, so the nuclear transitions present characteristic energies in this range. Many involve $gamma$-ray emission, for instance β^+ decay with a successive $gamma$-decay into a stabler state:

$${}^nX \rightarrow {}^{n-1}Y + e^+ + \nu_e, \qquad {}^{n-1}Y \rightarrow {}^{n-1}Y + \gamma.$$

These processes produce distinct line spectra, corresponding to the energy levels in the nuclei, which are very important for the analysis of the chemical composition of cosmic sources.

In general terms, if a relativistic particle (let's suppose here a neutral pion, π^0) with Lorentz factor γ and energy $E_{\pi^0} = \gamma m_{\pi^0} c^2$ decays into γ-rays, their energy E_γ will

also be boosted: $E_\gamma = \gamma E'_\gamma(1 + \beta\cos\theta')$, where E'_γ is the gamma-ray energy in the rest frame of the particle ($E'_\gamma = m_{\pi^0}c^2/2$ in the case of a neutral pion) and θ is the angle between the boost direction and the direction of the momentum of the γ-ray in the rest frame (see Fig. 1.17).

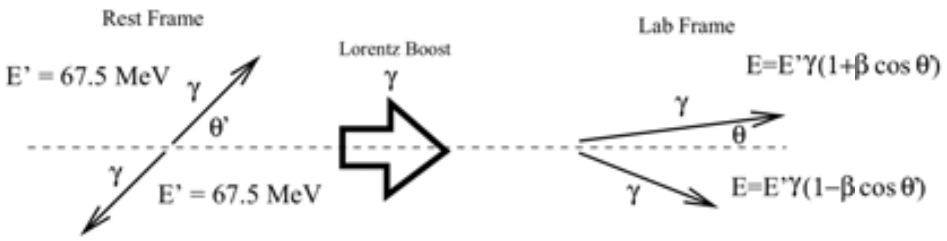

Figure 1.17
Kynematics of a $\pi^0 \to 2\gamma$ decay, when the π^0 is relativistic. Courtesy of T.Saito.

The resulting opening angle in the lab frame is much smaller: $\cos\theta = (\cos\theta' + \beta)/(1+\beta\cos\theta')$, the emission is beamed along the direction of motion of the parent particle.
If the spectrum of the parent particles is a power law with index α, e.g. $\mathrm{d}N_{\pi^0}/\mathrm{d}E_{\pi^0} \propto E_{\pi^0}^{-\alpha}$, then the spectrum of the resulting γ-rays has the same index:

$$E_\gamma = \frac{1}{2}E_{\pi^0} \quad \text{and} \quad N_{\pi^0} = 2N_\gamma \quad \to \quad \frac{\mathrm{d}N_\gamma}{\mathrm{d}E_\gamma} = 4\frac{\mathrm{d}N_{\pi^0}}{\mathrm{d}E_{\pi^0}} \propto E_\gamma^{-\alpha} \tag{1.34}$$

Bremsstrahlung also known as *free-free* emission, is the radiation of an accelerating charge in the field of another one[1]. It is the dominant energy loss process for high relativistic electrons colliding with the atmosphere, or other dense gases. A detailed treatment is outside the scope of this work; here it will be sufficient to mention that the approximate result for the energy loss per unit path length travelled in the relativistic case is (Bethe and Heitler, 1934; Jackson, 1999):

$$-\left(\frac{\mathrm{d}E}{\mathrm{d}x}\right)_{\text{brems}} = \frac{E}{x_B} \quad \text{with} \quad \frac{1}{x_B} \simeq 4\alpha r_e^2 Z(Z+1)N\left(z\frac{m_e}{M}\right)^2\left[\ln\left(\frac{233M}{Z^{1/3}m_e}\right)\right] \tag{1.35}$$

where:

α $= e^2/4\pi\varepsilon_0\hbar c^2 \simeq 1/137$ is the fine structure constant;
m_e $\approx 0.511/c^2$ MeV is the mass of the electron;
r_e ≈ 2.818 fm is the classical radius of the electron;
M is the mass of the incident particle;
z is the charge of the incident particle;
Z is the atomic number of the target material;
N $= N_A\rho/A$ is the number density of atoms in the target material;
ρ is the mass density of the target material;
A is the mass number of the target material;

[1]The particles involved have to be different, if they were identical the electrical dipole moment of the system would follow the position of their center of mass, without emission of photons.

$N_A \approx 6.022 \times 10^{23} \text{mol}^{-1}$ is Avogadro's number;

The quantity x_B is the bremsstrahlung *radiation length*, i.e. the path length that a particle must travel in a material in order to lose all but 1/e of its initial energy. In air at ambient pressure $x_B = 280$ m. The same quantity can be expressed in terms of matter travelled: $X_B = \rho x_B = 365$ kg/m^2.
It is worth noticing that the bremsstrahlung energy loss rate depends on on $1/M^2$, so the energy loss is much more important for lighter particles, such as electrons, than for protons. Also, it rises linearly with the energy of the incident particle E, so the solution to (1.35) is:

$$E(x) = E_0 \exp\left(-\frac{x}{x_B}\right) \tag{1.36}$$

therefore a relativistic particle that radiates via bremsstrahlung loses energy exponentially along its path. For cosmic rays impinging on the atmosphere, the bremsstrahlung losses are very important, since its column density is ~ 10000 kg/m^2, accounting for about 27 radiation lengths.
The energy of photons emitted by bremsstrahlung is on average a large fraction of the energy of the incident particle: if their ratio is $y = k/E$, then the the differential cross section (and probability density function) for their production is:

$$\frac{\mathrm{d}\sigma}{\mathrm{d}y} = \frac{A}{X_B} N_A \left(\frac{4}{3y} - \frac{4}{3} + y\right), \tag{1.37}$$

when $y > 0$. The probability of producing a photon with y 0.5 is greater than 60%.

Synchrotron radiation is a process that dominates energy losses in high-energy electrons, it is of extreme relevance in high energy astrophysics since it accounts for the bulk of non-thermal radio emission from the Galaxy and other extragalactic radio sources, for the optical non-thermal continuum of pulsar wind nebulae such as the Crab, for the optical and the X-ray emission of quasars. A detailed through derivation of the quantities involved in this process can be found in e.g. Rybicki and Lightman (1991) or Longair (2011), here only a brief overview of the main results will be given.
When a relativistic electron with speed $v \sim c$ and Lorentz factor γ moves in a uniform magnetic field of intensity B, the Lorentz force is:

$$\mathbf{F} = \frac{e}{c}\left(\mathbf{E} + \mathbf{v} \times \mathbf{B}\right) = \frac{\mathrm{d}}{\mathrm{d}t}(\gamma m_e \mathbf{v}). \tag{1.38}$$

The parallel and perpendicular components of **F** to the magnetic field are:

$$F_{\parallel} = \frac{e}{c} E_{\parallel} \qquad \text{and} \qquad F \;\; = \frac{e}{c}(E \;\; + v \;\; B). \tag{1.39}$$

The magnetic field only contributes to the acceleration perpendicular to its orientation. This means that in absence of electric fields the absolute value of the velocity

v does not change, only its direction does. The electron follows a helicoidal path of pitch angle α with respect to the magnetic field direction (see Fig. 1.18a). The gyration (Larmor) radius is:

$$r_g = \frac{\gamma m_e c^2 \beta \sin\alpha}{eB}, \tag{1.40}$$

and the fundamental frequency of gyration is

$$\nu = \frac{eB}{2\pi\gamma m_e c} = \frac{\nu_g}{\gamma}, \tag{1.41}$$

where ν_g is the sub-relativitstic gyration frequency.
The emitted power by a single electron is given by the Larmor formula:

$$P(\alpha) = \frac{2e^4}{3m_e^2 c^3} B^2 \gamma^2 \beta^2 \sin^2\alpha. \tag{1.42}$$

In the sub-relativistic case, the emission is dipole-shaped, however due to aberration effects, relativistic electrons emit radiation collimated in a cone of aperture angle $\Delta\theta = 1/\gamma$ in the forward direction, tangential to its motion (see Fig. 1.18b).

The radiation is linearly polarized if the magnetic field and the line of sight are perpendicular, otherwise it is elliptically polarized.

The characteristic frequency is related to the fraction of the time, for each orbit, during which the radiation is beamed towards the observer:

$$\nu_s = \gamma^3 \nu = \gamma^2 \frac{eB}{2\pi m_e c} \tag{1.43}$$

The spectral emissivity (see §A.1) of the particle in the ultrarelativistic limit can be calculated starting from the Li"nard-Wiechert potentials, and the result is:

$$j(\nu) = \frac{\sqrt{3} e^3 B \sin\alpha}{m_e c^2} \frac{c}{4\pi\varepsilon_0} F(x), \tag{1.44}$$

where:

- $x = \nu/\nu_c$ is the scaling parameter
- $\nu_c = \frac{3}{2}\nu_s \sin\alpha \approx 4.2 \times 10^{10} \gamma^2 B_{\perp\,\mathrm{T}}$ Hz is the threshold critical frequency, and $E_c = h\nu_c \approx 1.7 \times 10^{-4} \gamma^2 B_{\perp\,\mathrm{T}}$ eV is the threshold critical energy, with $B_{\perp\,\mathrm{T}}$ measured in Tesla;
- $F(x) = x \int_x^\infty K_{5/3}(z)\mathrm{d}z$ is the function displayed in Fig. 1.19, it can be well approximated to $F(x) \simeq 1.79 x^{0.3} \exp(-x)$;
- $K_{5/3}$ is the modified Bessel function of order 5/3.

The spectral emissivity is $\sim x^{1/3}$ when $\nu \ll \nu_c$, while it decays exponentially $\sim x^{1/2}\exp(-x)$ when $\nu \gtrsim \nu_c$. The bulk of the emission takes place at $E \sim 0.3 E_c$.

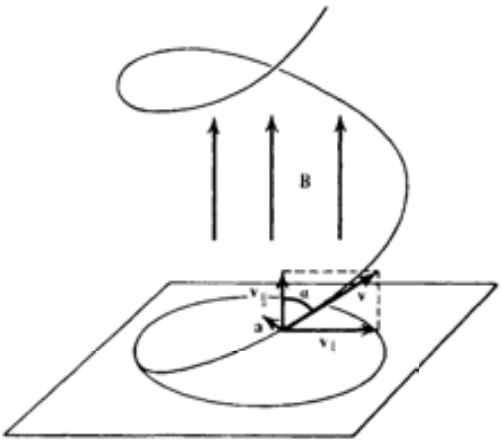

(a) A particle moving with velocity **v** in a magnetic field **B**, describing a helix, or spiral with pitch angle α.

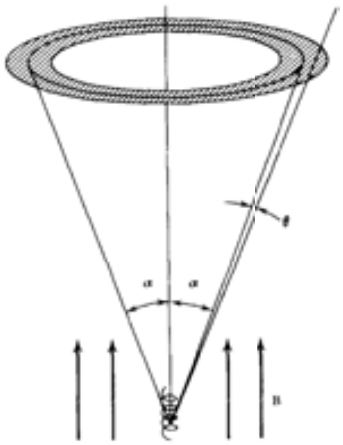

(b) Emission cone of synchrotron radiation from a single electron

Figure 1.18
Schematic illustration of the process of synchrotron radiation emission by a single electron. From Rybicki and Lightman (1991)

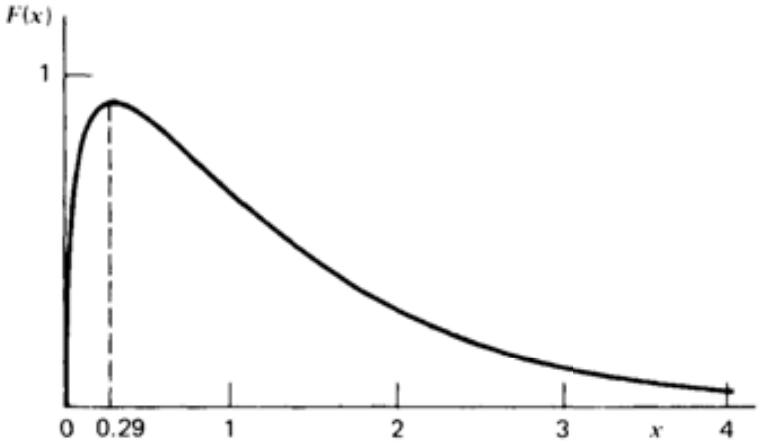

Figure 1.19
The function $F(x)$, which describes the emissivity of the single electron synchrotron emission (equation 1.44). From Rybicki and Lightman (1991).

The energy loss rate (emitted power) is:

$$P(\alpha) = -\left(\frac{\mathrm{d}E}{\mathrm{d}t}\right) = 2\sigma_T c U_\mathrm{B} \beta^2 \gamma^2 \sin^2 \alpha \tag{1.45}$$

where σ_T is the Thomson cross-section, $U_\mathrm{B} = B^2/2\mu_0$ is the energy density of the magnetic field and α is the pitch angle of the helix. Assuming α to be isotropic distributed, the average total energy loss is:

$$\langle P \rangle = -\left(\frac{\mathrm{d}E}{\mathrm{d}t}\right)_\mathrm{SYN} = \frac{4}{3}\sigma_T c \beta^2 \gamma^2 U_\mathrm{B} \tag{1.46}$$

The characteristic synchrotron cooling time is:

$$t_\mathrm{syn} = \frac{E}{\langle P \rangle} = \frac{3\gamma m_e c^2}{4\sigma_T c \beta^2 \gamma^2 U_\mathrm{B}} \approx \frac{7.75 \times 10^8}{B^2 \gamma} \text{ s}, \tag{1.47}$$

The characteristic energy of a photon emitted by synchrotron radiation is $E_{\rm sync} \sim \gamma^2 h\nu_g$, is proportional to the gyrofrequency $\nu_g = eB/(2\pi m_e)$, while the energy of a photon upscattered by inverse Compton is $E_{IC} \sim \gamma^2 h\nu$,where ν_γ is the frequency of the target photon.

It is interesting to compare the two γ-ray production methods in realistic conditions, e.g. those thought to be present inside the shocks of a supernova remnant: electrons have Lorentz factor $\gamma = 10^7$ (corresponding to an energy of 5.1 TeV), IC target photons are cosmic microwave background photons with frequency $\nu_\gamma \approx 10^{11}$ Hz, and the magnetic field is $\sim 3\times10^{-8}$ T, corresponding to a gyrofrequency of $\sim 10^3$ Hz. The energy of the inverse Compton upscattered photons would then be 41 GeV, while that emitted via synchrotron would only be 400 eV.

It also is important to note that the average energy loss in the case of synchrotron radiation (equation 1.46) in the case of inverse Compton scattering (in the Thomson regime, equation 1.23) differ only in the energy density term U: in the presence of seed photons and magnetic fields, the luminosity ratio of the two processes will be:

$$\frac{L_{\rm syn}}{L_{\rm IC}} \approx \frac{U_{\rm B}}{U_{\rm ph}},$$

however this relation breaks at high energies, due to the lower inverse Compton cross-section in the Klein-Nishina regime (equation 1.25).

For an isotropic population of electrons with a power-law spectrum with index p: $n(E)\mathrm{d}E = \nu E^{-p}\mathrm{d}E$, the synchrotron emissivity $\nu J_{\rm syn}(\nu)$ is:

$$J_{\rm syn}(\nu) = \frac{\sqrt{3}e^3 B\nu C(p)}{4\pi\varepsilon_0 m_e c}\left(\frac{2\pi\nu m_e^3 c^4}{3eB}\right)^{-(p-1)/2} \tag{1.48}$$

where $C(p)$ is a dimensionless function of p.

Setting $\alpha = (p-1)/2$ simplifies the proportionality relations, and for the intensity (using equation A.5) they are:

$$I_{\rm syn}(\nu) \propto R\nu B^{\alpha+1}\nu^{-\alpha}; \tag{1.49}$$

the emitted synchrotron radiation has a power-law distribution whose slope α is harder than the slope of the injected electron population p, as in the case of inverse Compton scattering (equation 1.29).

It is important to mention that a specular process exists: that of synchrotron absorption. At low energies (radio wavelengths for typical radio sources where $\alpha \approx 1$) the spectrum of the radiation changes because of self-absorption. This starts to happen

ν In this case it is the power per unit solid angle per unit volume emitted by the whole population of electrons,

$$J(\nu) = \int_0^+ j(\nu)n(E)\mathrm{d}E$$

when the brightness temperature of the synchrotron radiation T_b approaches the kinetic temperature of the electrons T_e.

T_b is defined as:

$$T_b = \frac{\lambda^2}{2k_B} I_\nu \propto \nu^{-}(2+\alpha) \tag{1.50}$$

where λ is the wavelength of the radiation, k_B is Boltzmann's constant and I_ν is the flux intensity, proportional to $\nu^{-\alpha}$.

Assuming that photons with frequency ν are produced and absorbed by electrons with Lorentz factor γ, T_e can be written as a function of ν:

$$T_e = \frac{\gamma m_e c^2}{3k_B} \approx \frac{m_e c^2}{3k_B} \left(\frac{\nu}{\nu_g}\right)^{1/2}, \tag{1.51}$$

When $T_b \quad T_e$, the photons are reprocessed thermically by the electrons, and the resulting flux intensities is that of black-body radiation in the Rayleigh-Jeans limit:

$$I_\nu \approx \frac{2k_B m_e c^2}{\lambda^2} \left(\frac{\nu}{\nu_g}\right)^{1/2} \propto \frac{\nu^{5/2}}{B^{1/2}} \tag{1.52}$$

The self-absorption frequency ν_t marks the transition from the optically thin case, where the spectrum is proportional to $\nu^{-\alpha}$, to the optically thick case, when the synchrotron radiation is absorbed by the same electrons that emit it, and the spectrum is $\nu^{5/2}$.

At ν_t, the two cases overlap. Then, if R is the size of the emitting region, and θ_s is its angular size, and $F_t = F(\nu_t)$ is the synchrotron flux at the self absorption frequency, both the magnetic field B and the Thomson optical depth $\tau_c = \sigma_T \int \nu \mathrm{d}x \approx \sigma_T \nu R$, of the source can be determined from equations 1.49 and 1.52:

$$B \propto \frac{\theta_s^2 \nu_t^5}{F_t^2} \tag{1.53}$$

$$\tau_c \propto \frac{F_t \nu_t^\alpha}{\theta_s^2 B^{1+\alpha}} \tag{1.54}$$

Curvature radiation is in many ways analogous to synchrotron radiation: it's the electromagnetic radiation of charged particles moving along a curved path. However, it is relevant in the case of very intense, curved magnetic fields $|\mathbf{B}| \sim (10^{11} - 10^{13}$ G): in this case the path of the particles is forced along the magnetic field lines because of the fast (synchrotron) radiative damping of their perpendicular oscillations (Chugunov et al., 1975, see), and their motion can be effectively approsimated as happening along de direction of **B** and not perpendicular to it.

If the curvature radius of the magnetic field line is R_c, the power radiated will be:

$$\left(\frac{\mathrm{d}E}{\mathrm{d}t}\right)_c = \frac{2}{3}\frac{e^2}{c}\left(\frac{v_\parallel}{R_c}\right)^2 \frac{E}{mc^2}, \tag{1.55}$$

where $v_{\parallel}$ is the particle velocity along the curved magnetic line, E the particle energy, and m its rest mass.
The mean energy for a photon emitted by a curving electron with Lorentz factor γ is:

$$E_{CR} \simeq 2.96 \times 10^{-3} \frac{\gamma^3}{R_c}, \tag{1.56}$$

where E_{CR} is given in eV and R_c in m. Since γ/R_c can reach very high values this is a much more energetic radiation than other electromagnetic processes, producing γ-rays up to energies of a few GeV. It arises mainly around compact objects with very intense magnetic fields, such as pulsars, and it is probably to responsible for the bulk of their emission in radio (Benford and Buschauer, 1977; Wang et al., 2012) up to γ-rays (see chapter2).
It is important to remark that if a small parallel electric field $E_{\parallel}$ is present, it can steadily accelerate the particle along the magnetic field lines, but the particle energy reaches a limit due to curvature radiation losses.

1.4 Interaction of cosmic rays and γ-rays with matter

The atmosphere of the Earth is for cosmic rays much like the target in an accelerator beam. High energy cosmic rays and γ-rays interact there with atoms, nuclei and electrons, undergoing several energy loss processes, summarized in the following table: Some of these processes (Bremsstrahlung, Compton scattering, nuclear

Table 1.2: Cosmic ray and γ-ray energy loss processes

Cosmic Rays	γ-rays
Bremsstrahlung	$e^{\pm}$ pair creation
Ionization	Direct Compton scatt.
Synchrotron rad.	Photonuclear absorpion
Inverse Comption scatt.	Photoelectric effect
Nuclear interactions	
Cherenkov rad.	
Curvature rad.	

interactions) were already described in section 1.3.2 in the context of high-energy gamma-ray production, since they are relevant also in the enviroments around the astrophysical sources. Others (ionization energy loss, particle and pair production losses) are more relevant at lower energies and will be briefly summarized in the following paragraph, more extended treatments can be found in (Rybicki and Lightman, 1991; Jackson, 1999; Vietri, 2008; Longair, 2011; Ghisellini, 2012)
As previously disclosed, if the primary particle has enough energy it can create extensive cascades of particles, or *extensive air showers*. All the above mentioned energy loss processes are involved.

Ionization energy losses occur as a result of the collisions between charged particles and atomic electrons, leading to the ionization of their atoms. For moderately relativistic heavy particles of mass M, charge z traversing at a velocity v a material or a gas with density ρ (kg/m^3), atomic number Z, atomic weight A (kg/mol), the ionization energy loss per unit path length, is given by the well-known Bethe-Block equation (From Beringer et al., 2012, chapter 30)

$$-\left(\frac{\mathrm{d}E}{\mathrm{d}x}\right)_{\text{ion}} = K\rho z^2 \frac{Z}{A}\frac{1}{\beta^2}\ \ \frac{1}{2}\ln\left(\frac{2m_e c^2\beta^2\gamma^2 T_{\max}}{\bar{I}^2}\right) - \beta^2 - \frac{\delta(\beta\gamma)}{2} \tag{1.57}$$

where:

K $= 4\pi N_A r_e m_e c^2 \approx 3.0707 \times 10^{-5}$ MeV^2 m mol^{-1} is a constant;

β and γ are the usual dynamic varibles of special relativity;

$\bar{I}$ $\approx Z \times 10$ eV is the weighted mean of the ionization potential of all electron states of the atoms of the traversed matter (85.7 eV for air);

$\delta(\beta\gamma)$ is a density-effect correction due to the polarization of the medium, which limits the energy loss at very high energies: $\delta(\beta\gamma) \to \ln(\hbar\omega_p/\bar{I}) + \ln\beta\gamma - 1/2$, with $\hbar\omega_p$ being the plasma energy of the medium (0.71 eV for air).

$T_{\max}$ $= (2\gamma^2 M^2 m_e v^2)/(m_e^2 + M^2 + 2\gamma m_e M)$ is the maximum kinetic energy transfer to the electrons. In case of electron-electron collisions, $T_{\max} = (\gamma^2 m_e v^2)/(1+\gamma)$

and the other quantities are defined as in equation 1.35.

In units of matter traversed $\chi = \rho x$ (kg m), the minimum ionization loss rate is $\approx \rho z^2 \times 0.2$MeV^2 m kg^{-1} and occurs when the kinetic energy of the particle is approximately equal to its rest mass energy, i.e. it has Lorenz factor $\gamma \approx 2$. At higher energies, the ionization loss rate increases logarithmically eventually reaching a plateau at 2MeV^2 m kg^{-1}; also, since $Z/A \sim 1/2$ for most nuclei, it depends little on the medium traversed. Is also worth noticing the fact that electrons and protons have the same ionization loss per unit path length when they are relativistic.

In the atmosphere, charged particles not only ionize, but also excite atoms, and part of the ionized atoms recombine in excited states, whose decay results in the phenomenon of fluorescence. Nitrogen molecules for instance emit fluorescent light in the blue wavelength region (300–450 nm), with a typical intensity of 5000 photons per km of track length. This fluorescent light is emitted isotropically.

Coulomb scattering is the electromagnetic elastic scattering of the incident particle on the nuclei of the medium. It is a relevant process for low-energy electrons and protons, its differential cross section is given by the well-known Rutherford formula:

$$\frac{\mathrm{d}\sigma_s}{\mathrm{d}\Omega} = \left(\frac{2zZe^2}{pv}\right)^2 \frac{1}{(2\sin\theta/2)^2} \tag{1.58}$$

where z,p and v are the charge, momentum and velocity of the incident particle. At small scattering angles θ electron screening prevents singularity and the sine term in (1.58) can be approximated as $1/(\theta^2+\theta^2_{\rm min})^2$, with $\theta_{\rm min} \approx \frac{Z^{1/3} m_e c}{192 p}$ (Jackson, 1999). When the particle is scattered multiple times over a path x, the distribution of the final scattering angle is well described by Molière's theory of multiple scattering (Molière, 1947, 1948; Bethe, 1953). For most applications the angular distribution can be approximated with a Gaussian with variance:

$$\langle \Theta^2 \rangle \simeq \frac{4\pi}{\alpha}\left(\frac{z m_e c^2}{pv}\right)^2 \frac{x}{X_S} \tag{1.59}$$

where X_S is the multiple scattering characteristic length:

$$\frac{1}{X_S} = 4\alpha r_e^2 Z(Z+1) N \ln\left(\frac{183}{Z^{1/3}}\right) \tag{1.60}$$

Pair production is the result of photon-photon interactions between cosmic γrays and ambient target photons. In the atmosphere the target photons are typically those of the intense electric field in the vicinity of a nucleus.

The interaction can happen only if the center-of-mass energy is above the production threshold of $E_{\rm thr} = 2 m_e c^2$, that is

$$s_{\gamma\gamma} = E_1 E_2 (1-\cos\theta)^2 > E^2_{\rm thr} \tag{1.61}$$

where E_1 and E_2 are the energies of the incident photons and θ their collision angle.

As can be seen from Fig. 1.20, the cross section for head-on collisions has its maximum when $s_{\gamma\gamma}/E^2_{mathrmthr} \approx 2$.

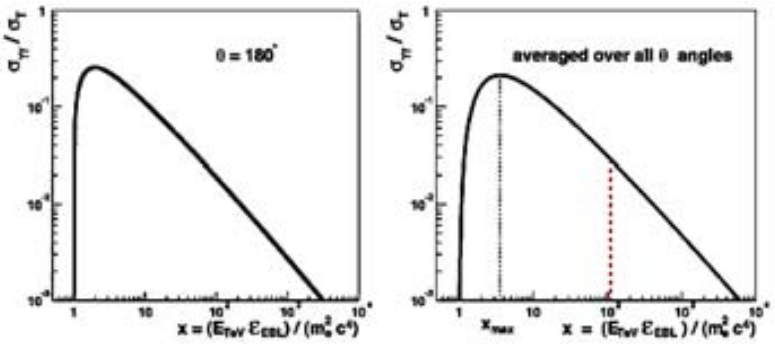

Figure 1.20
The integral photon-photon pair production cross section $\sigma_{\gamma\gamma}$ as a function of $x = E_1 E_2/(m_e^2 c^4)$. The angle θ is the collision angle.

Pair production is closely related to bremsstrahlung, since their Feynman diagrams are variants of one another.

In fact, when the energy of the incident photon ε is above 1 GeV its differential cross-section can be approximated as (Tsai, 1974; Beringer et al., 2012):

$$\frac{{\rm d}\sigma_p}{{\rm d}x} = \frac{A}{X_B} N_A \left[1 - \frac{4}{3}x(1-x)\right] \tag{1.62}$$

where X_B is the bremsstrahlung radiation length of equation 1.35, $x = E/\varepsilon$ is the ratio between the energy transferred to the pair E and that of the incident photon. Notice the similarity between equation 1.62 and 1.37.
Integrating over x, the total cross section is

$$\sigma_p = \frac{7}{9} A/(X_B N_A); \tag{1.63}$$

therefore the conversion length (the mean distance travelled by a photon before converting to a pair in a medium) is $X_p = \frac{9}{7} X_B$. The opening angle of the electron-positron pairs of the order of $m_e c^2/2E$, down to very small compared to the deviations due to multiple Coulomb scattering.

Photoelectric Effect is a dominant process when the incoming photon energy is much less than the electron rest mass ($h\boxtimes \ll m_e c^2$): the photon is absorbed by an atomic electron, which acquires enough energy to escape the atomic structure , leaving behind a ionized atom. The cross section for the process is approximately:

$$\sigma_{PE} = 4\alpha^2 \quad \overline{2}\boxtimes_0 Z^5 \left(\frac{m_e c^2}{h\boxtimes} \right)^{7/2}, \tag{1.64}$$

where $\alpha = e^2/4\pi\varepsilon_0 \hbar c \approx 1/137$ is the fine structure constant, $\boxtimes_0 = 6.651 \times 10^{-31}$ m^2 and Z is the atomic number.

Cherenkov Radiation was first discovered in 1934 by Cherenkov (1934), and understood few years later by Frank and Tamm (1937); in the following only a qualitative explanation of this phenomenon and some quantitative results are given, a fully detailed description be found in Jackson (1999),
Cherenkov Radiation is the coherent radiation emitted by a dielectric medium when a particle of charge z and mass m traverses it at velocity v greater than the phase velocity of light in it (super-luminal motion):

$$\beta > 1/n(\omega),$$

where $\beta = v/c$, $n(\omega)$ is the frequency-dependent refractive index of the medium, and ω is the frequency of the light. Related to this inequality are the quantities:

$$\beta_t(\omega) = \frac{1}{n(\omega)} \quad and \quad E_t(\omega) = \frac{mc^2}{\sqrt{1-\beta_t^2}}, \tag{1.65}$$

the minimum velocity and energy at which the particle starts to radiate Cherenkov radiation. Therefore Cherenkov emission varies with the refractive index (closely related with the local atmospheric conditions), and for a given β, the radiation is emitted only in frequency bands that fulfill $n(\omega) > \beta^{-2}$.
From (1.65) it is also clear that lighter particles such as electrons are favoured over

heavier ones, since their threshold energy is much lower: in air at ambient pressure $n \approx 1.0003$, the threshold energy for an electron is $E_t \approx 21$ MeV, while for a muon is ≈ 4.3 GeV.

Qualitatively, the cause of Cherenkov radiation can be understood as follows: the passage of a charged particle through a dielectric medium locally polarizes its molecules (Fig. 1.24a), which then return to unpolarized state shortly thereafter. The shift in the distribution of charges causes them to emit dipole radiation, which is in general incoherent: all energy is deposited near the path. Only in the case of super-luminal motion the radiation adds up coherently on a narrow cone of angle $\sim 2\theta_C$ around its trajectory (see Fig. 1.24b). This Cherenkov angle θ_C is then given by:

$$\cos\theta_C(\omega) = \frac{1}{\beta n(\omega)}, \tag{1.66}$$

where $\beta = v/c$.

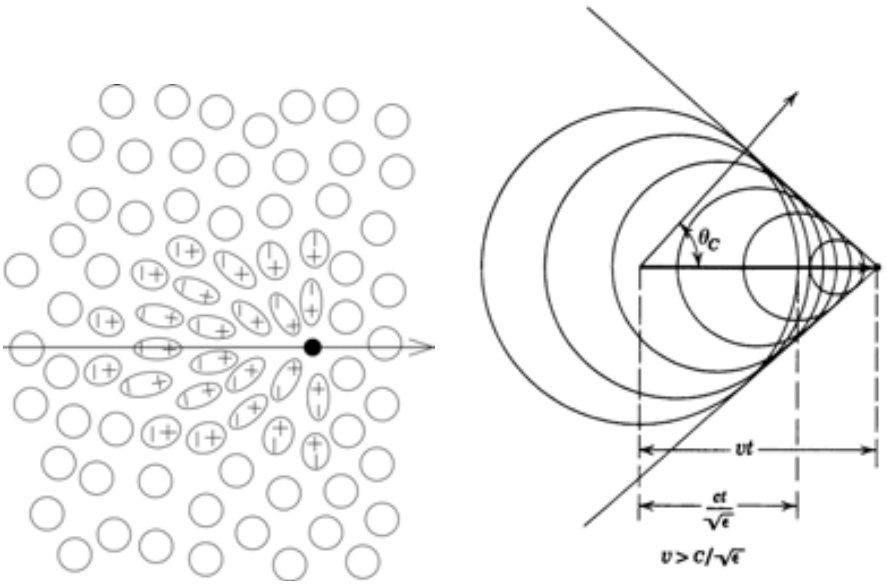

(a) Polarization of particles in a dielectric medium by a moving charge

(b) Huygens construction for the emission of Cherenkov light in a cone by a particle in super-luminal motion

Figure 1.24
Cherenkov radiation generation by super-luminal charged particle: polarized molecules emit dipole radiation that adds up coherently on a Cherenkov cone.

The number of photons produced per unit length and unit energy interval of the photon is (Frank and Tamm, 1937; Beringer et al., 2012):

$$\frac{\mathrm{d}^2N}{\mathrm{d}x\mathrm{d}\varepsilon} = \frac{\alpha z^2}{\hbar c}\sin^2\theta_C(\varepsilon) = \frac{\alpha^2 z^2}{r_e m_e c^2}\left(1 - \frac{1}{\beta^2 n^2(\varepsilon)}\right) \approx 3.7 z^2 \sin^2\theta_C(\varepsilon)\ \mathrm{eV}^{-1}\,\mathrm{m}^{-1}, \tag{1.67}$$

where $\varepsilon = \hbar\omega$ is the energy of the emitted photons. Integrating (1.67) over wavelengths between 300 and 600 nm ($\varepsilon = hc/\lambda$ between 2.06 and 4.13 eV) it turns out

that a relativistic particle above threshold generates about 100 photons of wavelength per meter of path near ground level; at 10 km height this number is reduced to $\simeq 8$, because there the air density, pressure and refractive index are lower.

2. VHE γ-rays from Pulsars and Blazars

2.1 Pulsars

General characteristics

Mass, Radius and Structure Pulsars are highly magnetized rotating neutron stars (Gold, 1968), resulting from the final collapse of a massive parent star M_{parent} $M_\odot$.
In general, neutron stars originate when the mass of the parent's core is between the critical Chandrasekhar mass of $\simeq 1.44 M_\odot$ and $\approx 3.8 M_\odot$: in this case the Fermi pressure of its degenerate electron gas cannot balance out its own gravity, causing it to further collapse reaching a density of $\rho \approx 10^{14}$ g cm^{-2} and a radius of about 10 km. In this process most of the core's matter undergoes *neutronization*: $p + e^- \rightarrow n + \boxtimes_e$.
The collapse is then stopped by the Fermi pressure of the degenerate neutron gas, provided that the core is less massive than $\approx 3.8 M_\odot$.
The resulting neutron star rotates very rapidly due to the conservation of angular momentum. Let's assume a parent star with initial radius $R_{in} \approx 10^9$ m and a period $P_{in} \approx 10^6$ s of about two weeks: the resulting neutron star (assuming $R_{fin} \approx 10^4$ m) will have a period of $P_{fin} \approx P_{in} \left(R_{fin}/R_{in}\right)^2 = 10^{-4}$ s.
A similar process gives rise to the star's strong magnetic fields: after the collapse the plasma currents in the stellar interior increase by the factor $\left(R_{in}/R_{fin}\right)^2 \approx 10^{10}$, and so does the magnetic field, reaching magnitudes of $\approx 10^{12}$ G. These estimates are in good agreement with the observed emission properties.
Determining the radius of a neutron star is not an easy task: observations of the thermal emissions in optical and X-rays can be used, however the presence of a strong gravitational field, a plasma atmosphere and luminosity alterations due to the strong magnetic field complicate the calculations. Most theoretical models predict a radius of 10-12 km. An upper limit for the radius can be derived from stability arguments against break-up due to centrifugal forces:

$$R_{max} \simeq \left(\frac{GMP^2}{4\pi^2}\right)^{\frac{1}{3}} = 16.8 \left(\frac{M}{M_\odot}\right)^{\frac{1}{3}} \left(\frac{P}{\text{ms}}\right)^{\frac{1}{3}} \text{ km} \tag{2.1}$$

where P is the period and M the star's mass.
The structure of a neutron star is composed by several layers with increasing densities, and is determined mainly by its equation of state. One of the most common models is displayed in Fig. 2.1.
The presence of *glitches* in the pulsar pulsations suggests that its outer layer (the "crust") is composed by iron nuclei and degenerate electron gas, with a density of $\rho \approx 10^6$ g cm^{-3}. Neutronization happens in the inner crust, where an abundance of neutron-rich nuclei are also present. Below the neutron drip point at $\rho \approx 4 \cdot 10^{11}$ g cm^{-3} the relative number of neutrons increases sharply. For the inner core there are several theoretical speculations, some of which involve quark plasma or exotic matter. As a whole, the average neutron star density calculated with conventional values, $\rho \approx 6.7 \cdot 10^{14}$ g cm^{-3} is higher than that of nuclear matter $\approx 2.7 \cdot 10^{14}$ g cm^{-3}.

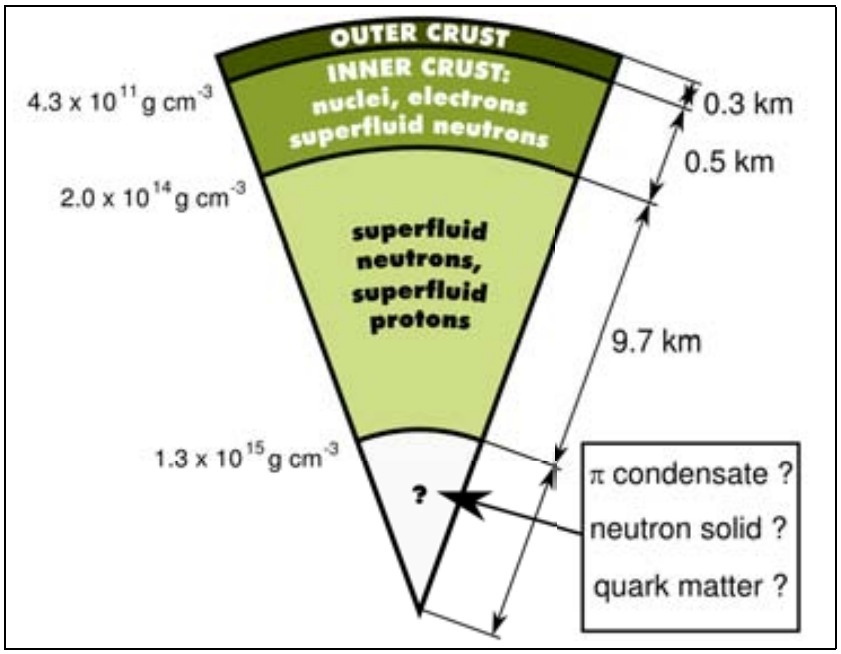

Figure 2.1
A model of the internal structure of a 1.4M$_\odot$ neutron star. From Shapiro and Teukolsky (1983).

Spin down The frequency of the pulsed emission is observed to be constantly decreasing. This *spin down* $\dot{P} = dP/dt$ implies a loss of rotational energy E_{rot}, called *spin-down luminosity*.

$$\dot{E} = -\frac{dE_{rot}}{dt} = 4\pi^2 I \dot{P} P^{-3} = I\dot{\Omega}\Omega =\simeq 3.95 \times 10^{31} \left(\frac{\dot{P}}{10^{-15}}\right)\left(\frac{P}{\mathrm{s}}\right)^{-3} \ \mathrm{erg\ s^{-1}} \quad (2.2)$$

where $I = 10^{45}$ g cm^2 is the moment of inertia of the pulsar, $I = kMR^2$, with typical values for M and R and $k = 0.4$ (uniform sphere).

$\Omega = 2\pi/P$ is the angular frequency of rotation.

Knowing the pulsar's distance d, one can calculate the *spin-down energy flux*: $\dot{E}/(4\pi d^2)$ Only a small fraction of this spin-down luminosity is converted in electromagnetic emission, the rest goes into to accelerate particles of the *pulsar wind*. A general description of the spin-down that takes into account the different dissipation mechanisms is the following:

$$\dot{\Omega} = -K\Omega^n \tag{2.3}$$

where K is a constant;

n is the *braking index*. If we were to model the pulsar spin-down as due only to the electromagnetic emission of a dipole, $n = 3$. It is possible to measure n using the second derivative of Ω : $n = \Omega\ddot{\Omega}/\dot{\Omega}^2$: the results range from $n = 1.4$ to $n = 2.9$.

Age estimates, birth period, time evolution Equation 2.3 can be rewritten in terms of the period, leading to $\dot{P} = KP^{2-n}$. This is then further integrated leading to the determination of the age T (Manchester and Taylor, 1977):

$$T = \int_{P_0}^{P} \frac{1}{KP'^{2-n}} dP' = \frac{P}{(n-1)\dot{P}} \left[1 - \left(\frac{P_0}{P}\right)^{n-1}\right] \tag{2.4}$$

where P_0 is the period at birth. One can define the *characteristic age* τ_c of a pulsar by assuming $n = 3$ and $P_0 \ll P$:

$$\tau_c = \frac{P}{2\dot{P}} \tag{2.5}$$

This equation often overestimates the true age of the pulsar, indicating that P_0 is not much smaller than P.

If n is constant, one can invert equation 2.4 and find the time evolution of the period P:

$$P = P_0 \left[1 + \left(\frac{n-1}{2}\right)\frac{t}{\tau_C}\right]^{\frac{1}{n-1}} = P_0 \left(1 + \frac{t}{\tau_0}\right)^{\frac{1}{n-1}} \tag{2.6}$$

with τ_0 representing the timescale of the spin down process:

$$\tau_0 = \frac{2\tau_C}{n-1} \tag{2.7}$$

The magnetic field and the spin-down luminosity evolve similarly:

$$B(t) = B_0 \left(1 + \frac{t}{\tau_0}\right)^{\frac{n-1}{2n-2}} \tag{2.8}$$

$$\dot{E} = \dot{E}_0 \left(1 + \frac{t}{\tau_0}\right)^{-\frac{n+1}{n-1}} \tag{2.9}$$

where $\dot{E}_0$ is the initial spin-down luminosity of the pulsar.

Emission in Radio and Optical and X-Rays The pulsar radio emission is very strong: the first pulsar was in fact discovered in radio in 1967, and the name *pulsar* is an abbreviation of *Pulsating Radio Source*. This emission is believed to be of non-thermal origin, and its intensity for the pulsars in the ATNF Catalog (Manchester et al., 2005) measured at 1.4 GHz, ranges from 20 μJy to 5 Jy. When radio waves propagate through ionized interstellar medium, they undergo a frequency dependent dispersion: this phenomenon can serve as a probe to investigate the integrated density of the free electrons along the line of sight.
The optical emission is on the contrary very feeble: only a handful of pulsars (Crab, Vela, Geminga, PSR B0540-69 and PSR 1929+10) are detected in the frequency range between 10^{12} Hz and 10^{16} Hz. The optical emission is not spectrally correlated to the high-energy emission, as both thermal and non-thermal processes can play a role in it.
In the X-ray band the latest space observatories have discovered 15 "regular" pulsars and six *millisecond* pulsars. The emission spectrum shows a power-law component probably due to non-thermal emission in the magnetosphere, and a black-body component probably associated with the hot rotating polar caps.
The *millisecond* pulsars are a class of older pulsars that start accreting matter from a companion star, this accelerates their rotation and greatly enhances their high-energy emission.

The pulsar magnetosphere

Magnetic field strength it is possible to estimate a pulsar's surface magnetic field intensity B_S by modeling it as a simple rotating magnetic dipole (see figure 2.2) and assuming that the electromagnetic braking due to radiation is the dominant way of energy dissipation. One proceeds from the classical equation for a rotating magnetic dipole **m** inclined by an angle α from the rotation axis (Jackson, 1999):

$$\mathbf{m} = \frac{1}{2} B_S R^3 \left[\mathbf{j} \cos\alpha + \mathbf{i} \sin\alpha \cos(\Omega t) + \mathbf{k} \sin\alpha \sin(\Omega t) \right] \tag{2.10}$$

where **i**, **j**, **k** are three unitary vectors, perpendicular to one another and with **j** parallel to the rotation axis. The radiation power emitted by this magnetic dipole is:

$$\frac{dE_{EM}}{dt} = -\frac{2}{3} \frac{|\ddot{\mathbf{m}}|^2}{c^3} = -\frac{B_S^2 R^6 \Omega^4 \sin^2\alpha}{6c^3} \tag{2.11}$$

By equating this to the spin-down luminosity equation 2.2, one obtains an order of magnitude estimate for B_S:

$$\frac{dE_{EM}}{dt} = \frac{dE_{rot}}{dt} \rightarrow B_S = \sqrt{\frac{3c^3}{8\pi^2} \frac{I}{R^6 \sin^2\alpha} P\dot{P}} \tag{2.12}$$

using the standard values for $I = 10^{45}$ g cm^2, $R = 10$ km and $\alpha = 90$, from equation 2.12 one obtains the following estimate: $B_S = 3.2 \times 10^{19} \sqrt{P\dot{P}}$ G.

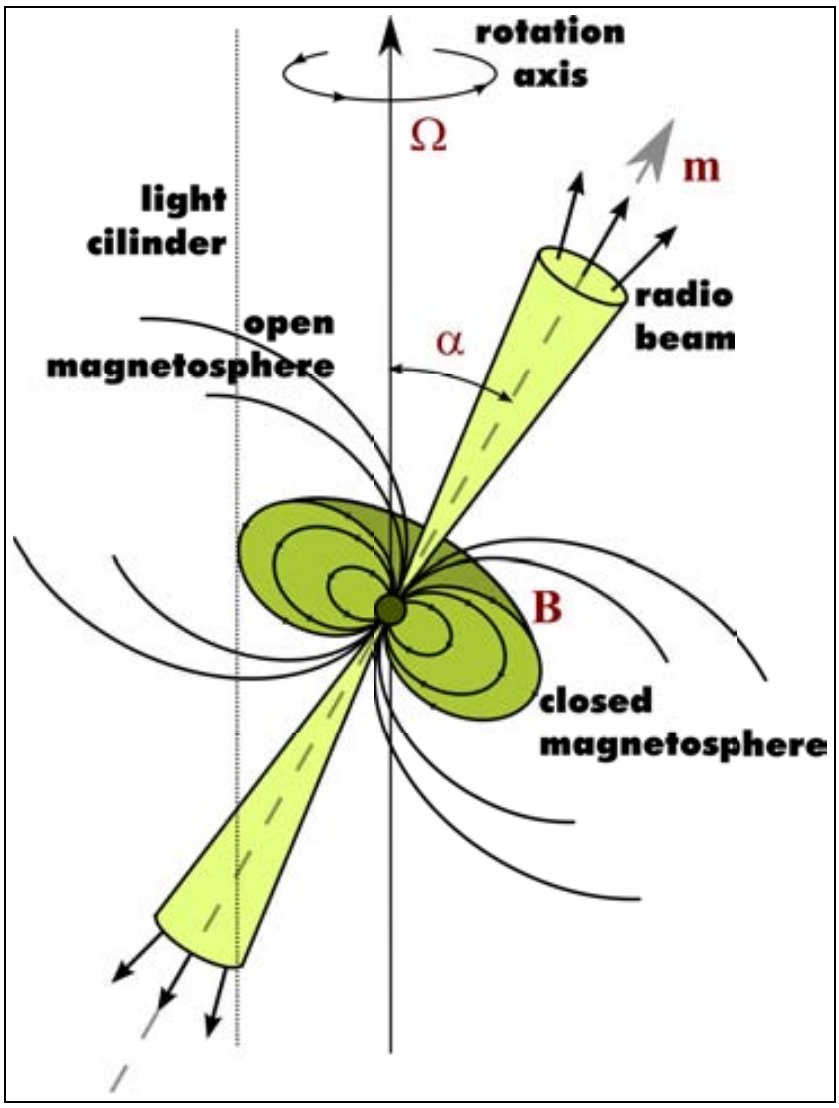

Figure 2.2
Simple model for the magnetic field of a pulsar. Ω is the angular velocity, **m** the magnetic moment and α the angle between **m** and the rotation axis. The light cylinder has a radius of $R_L = c/\Omega$.

It is possible to give an immediate representation of the pulsar population by plotting for each pulsar its period derivative $\dot{P}$ versus its period P. This P-$\dot{P}$ diagram, shown in figure 2.3, is very powerful for classification purposes: the dashed blue and solid green lines represent the values for τ_C and B_S , calculated using equations 2.5 and 2.12, respectively.

The Goldreich - Julian Pulsar Magnetosphere The magnetic dipole model that was used to derive B_S in equation 2.12 does not take into account a possible plasma-filled magnetosphere, on the contrary, it requires a vacuum-surrounded pulsar. It was shown by Goldreich and Julian in 1969 (Goldreich and Julian, 1969) that pulsars cannot be surrounded by vacuum. Their proof assumes a rotating, infinitely

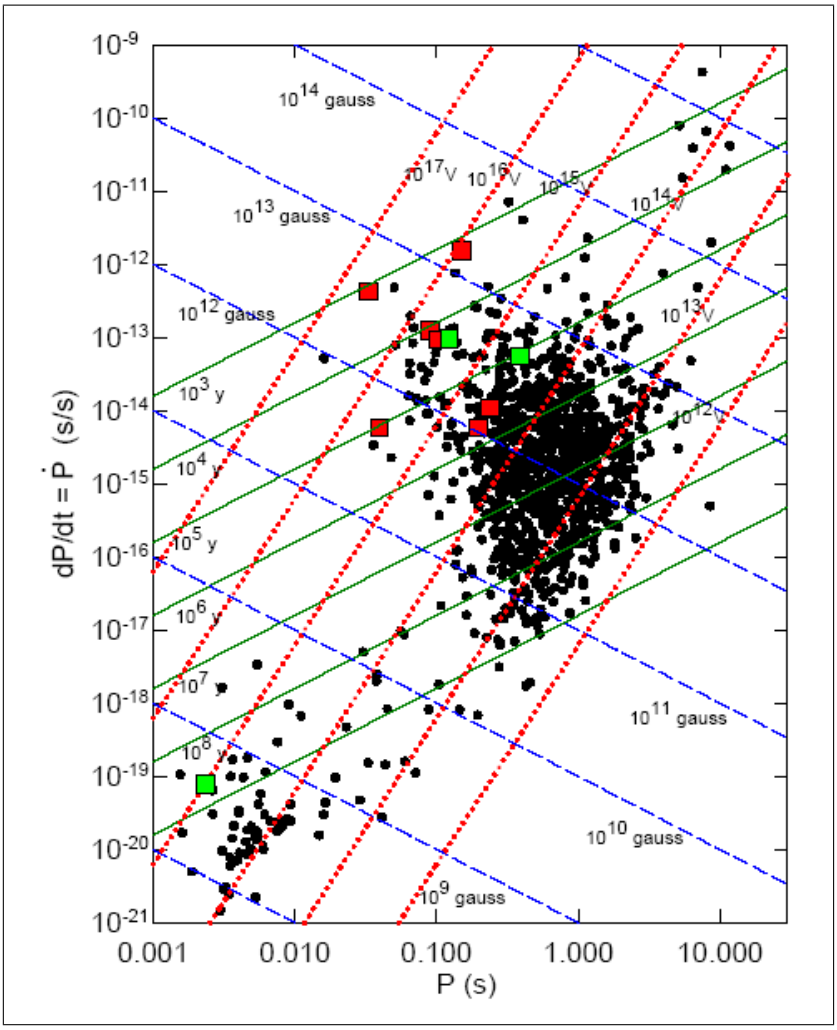

Figure 2.3
P-$\dot{P}$ diagram for the pulsars in the ATNF Catalog. The red squares are the seven confirmed high-energy gamma-ray pulsars of the EGRET era, the green squares are low-confidence detections . From Thompson (2003)

conductive magnetized neutron star, whose rotation axis is aligned to the magnetic dipole axis, and whose magnetic field can be approximated to a dipole, continuous at the stellar surface.
Then the electric and magnetic fields satisfy the following:

$$\mathbf{E} + \frac{1}{c}(\Omega \times \mathbf{r}) \times \mathbf{B} = 0 \tag{2.13}$$

The external electrostatic potential is obtained by solving Laplace equation:

$$(r, \theta) = 0 \rightarrow (r, \theta) = \frac{B_S \Omega R^5}{6cr^3} P_2(\cos\theta) \tag{2.14}$$

where $r, \theta,$ are the usual polar coordinates;
P_2 is the Legendre polynomial of second degree;

B_S is the surface polar magnetic field.

Assuming a dipolar magnetic field, equation 2.14 leads to the value of $\mathbf{E} \cdot \mathbf{B}$ outside the star:

$$\mathbf{E} \cdot \mathbf{B} = -\left(\frac{\Omega R}{c}\right)\left(\frac{R}{r}\right)^2 B_S^2 cos^2\theta \tag{2.15}$$

The electric field parallel to the magnetic field at the surface of the star is:

$$E_{\parallel} = \frac{\mathbf{E} \cdot \mathbf{B}}{B} = \frac{\Omega R}{c} B_S \cos^2\theta \simeq 6 \times 10^{10} \left(\frac{B}{10^{12}\ \mathrm{G}}\right) P^{-1}\ \mathrm{V\ cm^{-1}} \tag{2.16}$$

Near the outer edge of the polar charge layer the magnitude of the Lorentz force due to $E_{\parallel}$ 0 would exceed the gravitational force, causing an outflow of charged particles into the magnetosphere.
The general description of the structure of the inner pulsar magnetosphere following Goldreich-Julian is shown in figures 2.4 and 2.5. The model distinguishes between a *near zone*, a *wind zone* and a *boundary zone*.

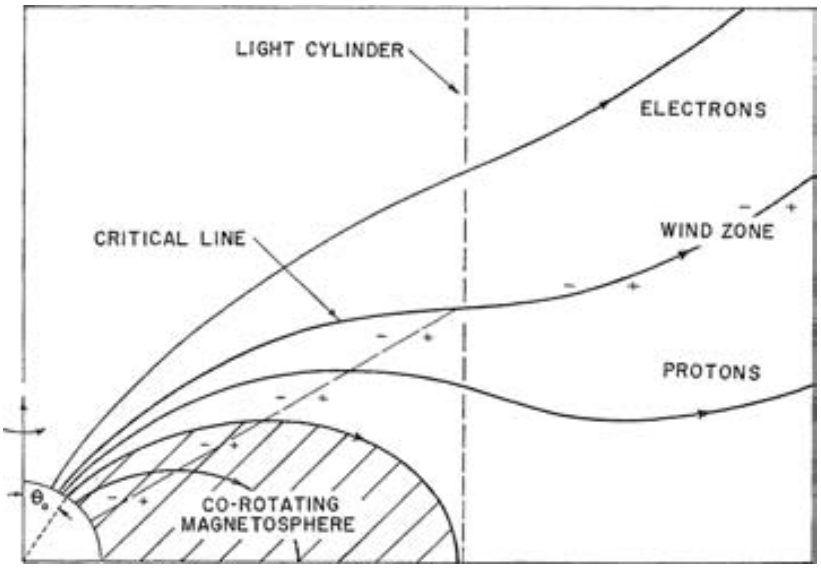

Figure 2.4
Schematic diagram showing the Goldreich-Julian model: the near zone extends until the light cylinder and is enclosed in the wind zone. Particles stream out of the near zone following open lines at $\theta < \theta_0$. The closed lines form the *co-rotating magnetosphere*. From Goldreich and Julian (1969)

The **near zone** is contained within the light cylinder ($r \sin\theta = c/\Omega$). Its magnetic field is in prevalence poloidal and is determined by the currents inside the star. The field lines are very nearly electric equipotentials, so charged particles slide along them: the ones attached to the closed field lines co-rotate, the ones that follow the open magnetic lines that pass through the light cylinder escape into the wind zone. The boundary between the closed and open lines is placed at $\theta_0 \simeq (\Omega R/c)^{1/2}$.
In the case of an "aligned rotator" ($\Omega \cdot \mathbf{B} > 0$), electrons escape along the field lines closest to the poles (*electron lines*) and protons along lower latitude open lines (*proton lines*). The proton lines cross a co-rotating cloud of electrons, and viceversa:

otherwise they would not be equipotential field lines. These open field lines subsequently close in the boundary zone.
The electric charge in the *co-rotating* part of the magnetosphere (where $\mathbf{E} \cdot \mathbf{B} = 0$) is given by:

$$\rho_{GJ} = \frac{1}{4\pi} \boxtimes \cdot \mathbf{E} = -\frac{1}{2\pi c} \frac{\Omega \cdot \mathbf{B}}{1 - (\Omega r/c^2)^2 \sin^2 \theta} \simeq 7 \times \frac{B_z}{P} \text{ cm}^{-3} \tag{2.17}$$

The **wind zone** encloses the near zone and extends to $r < D/10$, where D is the radius of the supernova shell that encloses the neutron star, outside of which there is the conductive interstellar medium. All charges at a given point in space have the same velocity since they have been accelerated along the same field lines. In this region there cannot exist co-rotating charge clouds, so there is only a sign of charge for every given point in space.
At the light cylinder the poloidal and toroidal components of the magnetic field are comparable, so they penetrate it at an angle of about 45°. Further out the toroidal magnetic field, determined by the poloidal outflowing current distributions, dominates over the poloidal magnetic field as:

$$-\frac{B_t}{B_p} = \frac{1}{\beta_p} \left[\left(\frac{\Omega r}{c} \right) \sin \theta - \beta_t \right] \rightarrow \left(\frac{\Omega r}{c} \right) \sin \theta \quad 1 \tag{2.18}$$

where B_t and B_p are the toroidal and poloidal components of the magnetic field $\mathbf{B}$;
β_t is the toroidal component of the charge velocity $\beta = \mathbf{v}/c$;
β_p is the poloidal components of β, which is found to approach unity as $\Omega r \sin \theta \quad c$.

The charge density in this zone follows from Maxwell equations, assuming a vanishing Lorentz force on the particles ($\mathbf{E} + \beta \times \mathbf{B} = 0$):

$$\rho_{GJ} = -\frac{1}{2\pi c} \frac{\Omega \cdot \mathbf{B}}{1 - (\Omega r/c) \beta_t \sin \theta} \tag{2.19}$$

The **boundary zone** is where the magnetic field lines that emerge from the star into the wind zone must close. All of them must do so within the supernova cavity because of the high electrical conductivity of the interstellar field. The magnetic field lines cannot be equipotentials anymore, and charges are further accelerated along them. This is where they receive most of their acceleration. A schematic illustration of the boundary zone is given in figure 2.5.
In the inner part of the boundary zone, the electric and magnetic fields are still determined by the outflowing relativistic particles, while the current and charge distributions of the interstellar medium play and increasingly decisive role near the supernova shell. Thus any spatial irregularity in the evolution of the supernova remnant influences the magnetic fields in the outer boundary zone.

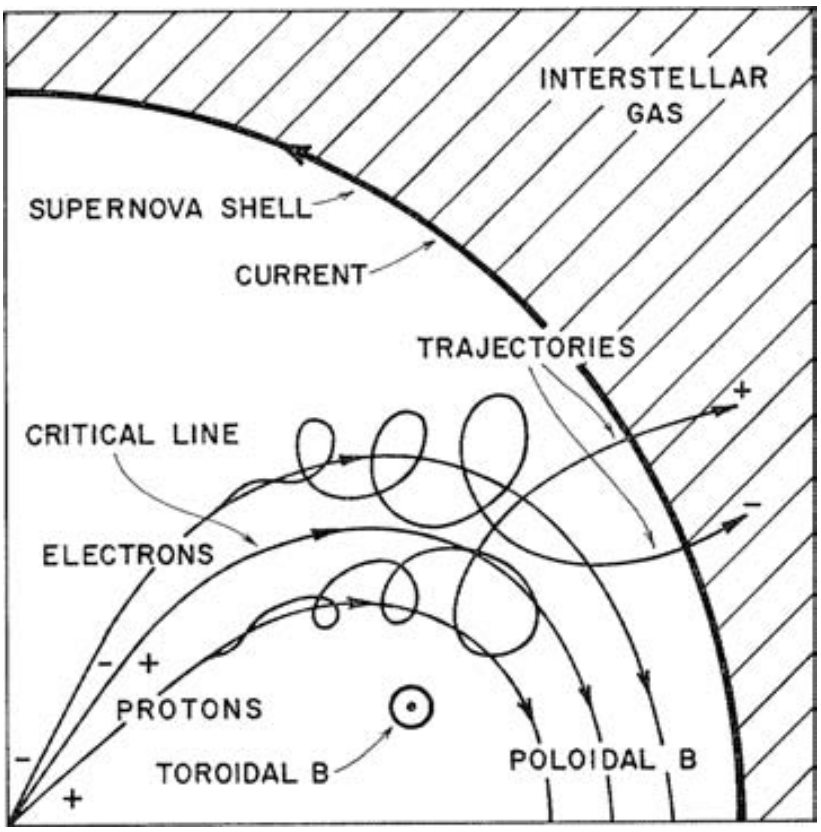

Figure 2.5
Goldreich-Julian model for the outer magnetosphere: inside the supernova cavity the field lines along which particles leave the pulsar close. The particles decouple from them and escape into the interstellar medium. From Goldreich and Julian (1969)

Note that on the cavity boundary there must exist macroscopic surface currents in order to maintain $\mathbf{E} = \mathbf{B} = 0$ in the interstellar gas, and thermal currents to cancel out the relativistic currents and charges that escape the supernova cavity.
Both the tangential component of the electric field and the toroidal component of the magnetic drop to zero for $r \rightarrow D$. The energy and angular momentum fluxes previously carried by the electromagnetic fields are transmitted to the particles, and there is an approximate equipartition of the energy density.

The Goldreich-Julian model predicts an energy loss rate comparable to that of the simple dipole model, but assuming a plasma filled magnetosphere and a much more complex scenario:

$$\dot{E} = -4\pi R_L^2 S_L \simeq -\frac{B_0^2 R^6 \Omega^4}{c^3} \tag{2.20}$$

where $R_L = \Omega/c$ is the radius of the light cylinder and S_L the Poynting flux at the light cylinder.

There are some inconsistencies in the model, such as charges of one sign having to flow through regions of the opposite sign, and the disappearance of the charge-extracting parallel field $E_\parallel$ in the inner magnetosphere. Nevertheless, it lays out the theoretical framework on which all present-day pulsar emission models rely.

Gamma Ray Emission

The gamma-ray emission from pulsars is of non-thermal nature: charged particles are extracted from the surface of the pulsar into a Goldreich-Julian plasma-filled magnetosphere and there accelerated up to high energy. They emit gamma rays through either synchrotron radiation or curvature radiation in the magnetic field of the pulsar or through inverse Compton scattering with the ambient and cosmic background photons.
The current theoretical models for γ-ray emission can be divided into two main categories: the *polar cap* (PC) models (after Sturrock (1971) and Ruderman and Sutherland (1975)) and the *outer gap* (OG) models (after (Cheng et al., 1986)). They both need a region of space were $\mathbf{E} \cdot \mathbf{B}$ 0 so that charged particles can be accelerated by Lorentz forces. They assume the presence of *vacuum gaps* around the pulsar where this condition is met.
They differ in describing its location and the proprieties of the emission: the PC model predicts an emission at low altitudes, near the polar cap (however variants exist that include high altitude emission from the so-called *slot gaps*); the OG model predicts an emission further out from the star, extending to the light cylinder.
The spectral shapes predicted by these two model classes also differ: because of different attenuation mechanisms, the PC model has a sharper *super-exponential* cutoff (proportional to $\exp\left(E/E_{cut}\right)^{\alpha}$ with $\alpha > 1$) than the simple exponential cutoff ($\alpha = 1$) of the OG model (Harding, 2000). Another point where the two models differ is the predicted γ-ray luminosities: in PC models, the luminosity is proportional to the current of primary particles: $N_0 \propto B_S\Omega^2$; in OG models N_0 depends on the fraction of the open field lines spanned by the outer gap accelerator, which differs from source to source.
OG models also predict a maximum age for γ-ray pulsed emission, while most PC models do not, and a higher ratio radio-quiet pulsars to radio-loud pulsars.

Polar Cap Model Polar cap models were the first models to be developed by relaxing the Goldreich-Julian conditions on the alignment of the magnetic field axis with the axis of rotation and on $\mathbf{E} \cdot \mathbf{B} = 0$ in the near and wind zones (Sturrock, 1971). The Sturrok model assumes the presence of a radial electric field situated at at low altitude above the polar caps, over an height h comparable to the radius of the polar cap. The particle acceleration takes places there, and the accelerated particles (notably electrons) emit in radio and in gamma rays through *curvature radiation* following their path along the curved magnetic-field lines. There is little synchrotron radiation because of the transverse kinetic energy of the extracted particles is negligible, and the inverse Compton scattering is not taken into account.

The electric potential responsible of the acceleration at the polar cap calculated by Sturrock is $\propto Bh^2/P$: its period-dependence means that pulsars stop emitting charged particles as they get older because the value of becomes too low. The critical value (*dead-line*) is about $P \simeq 1$ s for electron extraction and $P \simeq 0.02$ for proton

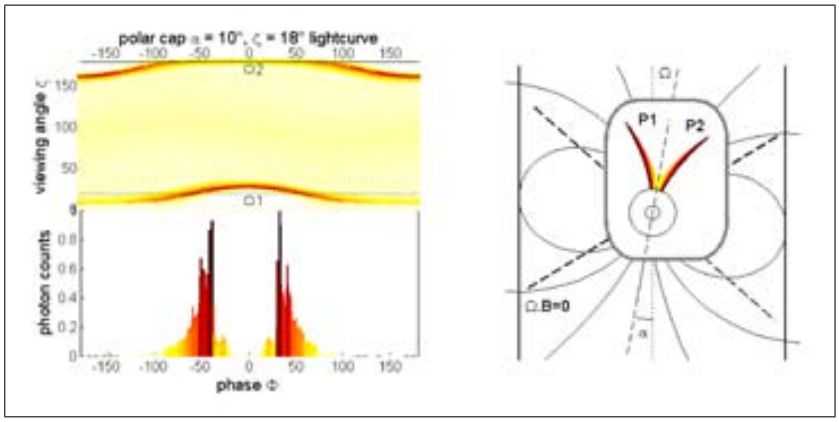

Figure 2.
Model of the emission of a pulsar whose inclination angle is 10°, following the polar cap model. The diagram on the right shows the predicted acceleration regions for the model, the one on the upper left hand side shows how the appearance of the pulse profile changes with the viewing angle, and the one on the bottom left hand side shows the pulse profiles. The regions on the pulse profile and viewing angle plot are matched to the acceleration regions that originate the emission using different colors. From Grenier and Harding (2006)

extraction.
The peak energy of the emitted curvature radiation is $E_\gamma \propto E_e^3/R_C$, where E_e is the electron energy and R_C its curvature radius. Because of the presence of an intense magnetic field B above the caps, the curvature γ-rays are converted into pairs by *magnetic absorption*: $\gamma + B \rightarrow e^+ + e^-$. These secondary pairs also emit synchrotron and curvature radiation and thus initiate an electromagnetic cascade, giving rise to an unstable non-stationary plasma outflow in the form of *charged sheets* of plasma, that is at the origin of the observed high brightness temperature in the radio emission. The simulated high-energy signal for a polar cap pulsar with 10° inclination is shown in Fig. 2.6.

The Sturrock model was expanded and enhanced by Ruderman and Sutherland (Ruderman and Sutherland, 1975). They pointed out that at the polar cap, the positive ions remain bound to the surface while the electrons escape and never return: this gives rise to a polar magnetospheric *vacuum gap* with a potential difference of 10^{12} V. This is in turn constantly discharged by sparks, which initiate EM showers. This model well explains the micropulse structure, the phenomenon of the *drifting subpulses* and the coherent microwave emission.
Another contribution to the polar cap model is that of Arons and Scharlemann (Arons and Scharlemann, 1979): they also assume the presence of a vacuum gap above the polar caps maintaining a potential difference of 10^{12} V, limited by a pair formation front, above which the potential is screened. This allows for a steady upward flux of relativistic electrons (and a small downward flux of positrons), and maintains $\mathbf{E}\cdot\mathbf{B} \simeq 0$ in the pair formation front and in the above region. They also introduced the idea of another vacuum region at high altitude above the polar cap and at the boundary of the open field lines: the *slot gap*, shown in figure 2.7. This region was not originally not considered a viable candidate for high-energy emission.

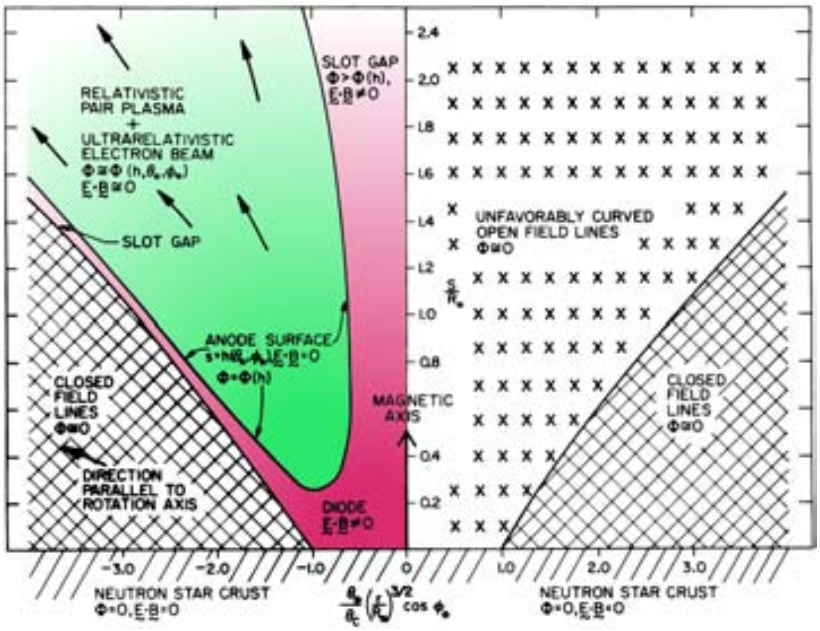

Figure 2.7
Arons and Scharlemann's model for a pulsar's polar cap. They propose that electrons are accelerated (because of $\mathbf{E} \cdot \mathbf{B} \neq 0$) in a vacuum gap (highlighted in magenta) extending above the polar cap. They introduce the idea of high-altitude slot gaps. The vacuum gap is delimited by a pair formation front, after which secondary particles are created (highlighted in green). γ-ray emission comes from both the vacuum gap accelerated electrons in the form of curvature radiation, and from the secondary particles, mainly through synchrotron radiation. The region with favorably curved field lines simply corresponds to that of electron acceleration, (for normal polarity), and the region with unfavorably curved field lines corresponds to that with of positive charge acceleration. Note that for the reversed polarity pulsar ($\Omega \cdot \mathbf{B} < 0$) the sign of accelerating particles reverses. From (Arons and Scharlemann, 1979)

A more recent model (Sturner and Dermer, 1994), has the pair cascade initiated by inverse Compton scattering of the charged particles on thermal X-rays emitted by the neutron star's surface. This model could explain the observed harder spectral indexes in the inter-pulses of some younger pulsars such as the Crab. It also requires a lower Lorentz factor for the primary electrons of $\gamma \approx 10^5$, so it could explain the γ-ray emission from older, less energetic pulsars beyond the curvature radiation deadline. Recent calculations (Harding and Muslimov, 2002) show that in this case the pair formation front produced does not suffice in creating a screening and primary particles keep accelerating to high altitudes.

Regarding the characteristics of the gamma-ray emission in the polar cap scenario, one of the first calculations (Harding, 1981) showed that the emission above 100 MeV is due to curvature radiation from accelerated primaries. Synchrotron radiation from secondaries plays a negligible role.
More recently detailed descriptions of the slot gap electrodynamics have been devel-

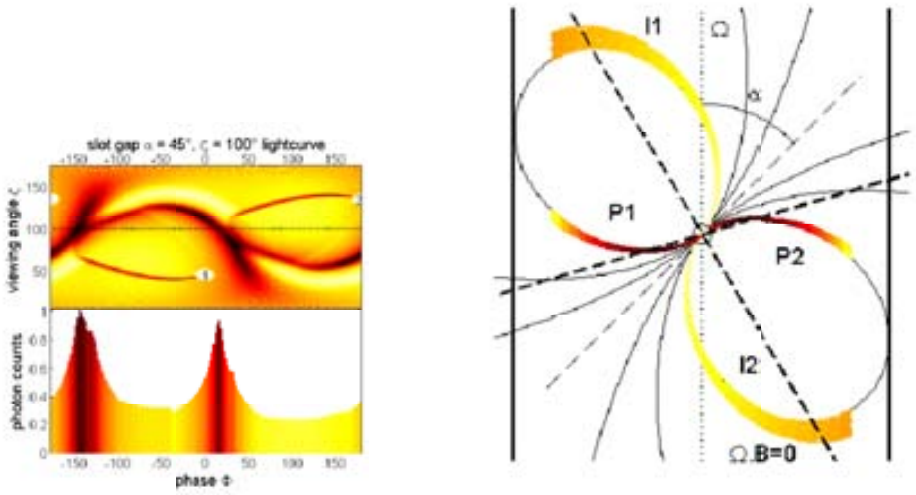

Figure 2.8
Slot gap emission of a pulsar whose inclination angle is 45°, plotted as in Fig. 2.6. From Grenier and Harding (2006)

oped (Muslimov and Harding, 2004), showing that the accelerating electric field $E_\parallel$ across the slot gap approaches a constant value at high altitudes. This residual field is indeed capable of accelerating electrons up to Lorentz factors of $\gamma \approx 10^7$, which result in emission of high-energy curvature photons up to the light cylinder. The simulated high-energy signal from a slot gap emission in a 45° inclined pulsar is shown in figure 2.8

Outer Gap Model The outer gap model of Cheng et al. (1986) takes a completely different approach, and tries to explain the emission mechanisms of young pulsars with a large spin-down energy loss. It's worth to be considered because it succeeds in explaining observational results for that pulsar class. The starting point is always an oblique rotator (in this case $\Omega \cdot \mathbf{B} < 0$) characterized by a magnetosphere whose density ρ doesn't differ significantly from the Goldreich-Julian density ρ_{GJ} of equation 2.17, except for the regions in which $\rho = 0$. These neutral regions in turn could not survive in if $\Omega^2 B$ is very high (as in the case of high spin-down energy loss, from equation 2.11), since they would be threaded by such a high $\mathbf{E} \cdot \mathbf{B}$ that the $e^\pm$ production mechanism would replenish them with a pair plasma that would restore $\rho \simeq \rho_0$.

The outer gap model thus allows for $\mathbf{E} \cdot \mathbf{B} \simeq 0$ almost everywhere within the light cylinder, except that along an almost slab-like vacuum gap called the *outer gap*. This region is limited on one side by a charge layer on the boundary of the closed field lines and on the other by a charge layer on the surface of an "open" magnetic field line, as one can see in figure 2.10. The presence of such a gap is justified by an assumed model of the magnetospheric current flow, shown in Fig. 2.11. In particular, the negative charge of the regions labelled "A" in figure 2.11 tends to flow out from the light cylinder, leaving out a negative-charge depleted region which acts as

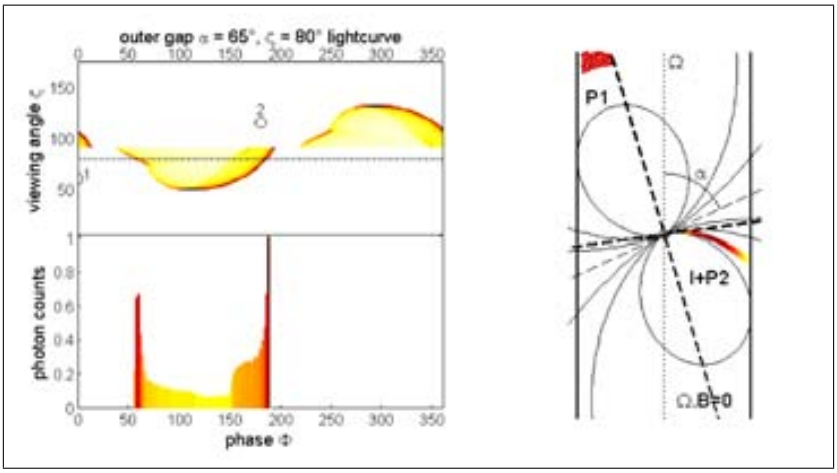

Figure 2.9
Outer gap emission of a pulsar whose inclination angle is 45°, plotted as in Fig. 2.6. From Grenier and Harding (2006)

a positively charged region. This in turn effectively pushes towards the star the positive, charge-separated plasma on the other side of the null surface (the layer where $\Omega \cdot \mathbf{B} = 0$), and a growing vacuum gap arises.

A potential drop along B and a large $\mathbf{E} \cdot \mathbf{B} \quad 0$ are induced in a gap by the local deviation of ρ from ρ_{GJ}. Negative charges from the star are continuously accelerated outwards and positive charges pulled in from the light cylinder are accelerated inwards. γ-rays from these primaries come mainly from curvature and synchrotron radiation along the curved magnetic field lines and from inverse Compton on strong soft photon fluxes, and propagate tangentially to **B**. These gamma rays are magnetically attenuated by in the surrounding magnetic field, providing the $e^{\pm}$ pairs that ultimately prevent total charge depletion, quench the potential difference and limit the extension of the slab.
The geometry of the beaming is depicted in figure 2.10, and explains not only the double γ-ray pulse profiles of the Crab and Vela pulsars, but also the fact that emission from both of these pulsars is observed, where in the case of conical, narrow-beamed emission, the probability of observing it from both would be ~ 1/25.

2.2 Blazars

Blazars (blazing quasars) are a minor subclass of Active Galactic Nuclei (AGN, Robson, 1996; Kembhavi and Narlikar, 1999), a class of galaxies hosting a very luminous, compact and massive central region, emitting across a large part of the electromagnetic spectrum.
AGNs make up for about 1% of the observed galaxies, and Blazars account for less than 5% of all Active Galactic Nuclei. With 50 known sources (at the time of writing, source: TeVCat, Wakely and Horan, 2012) they are however the most numerous class of extra-galactic sources emitting VHE γ-rays, and make up for a little less than one-third of all the known VHE γ-ray sources.

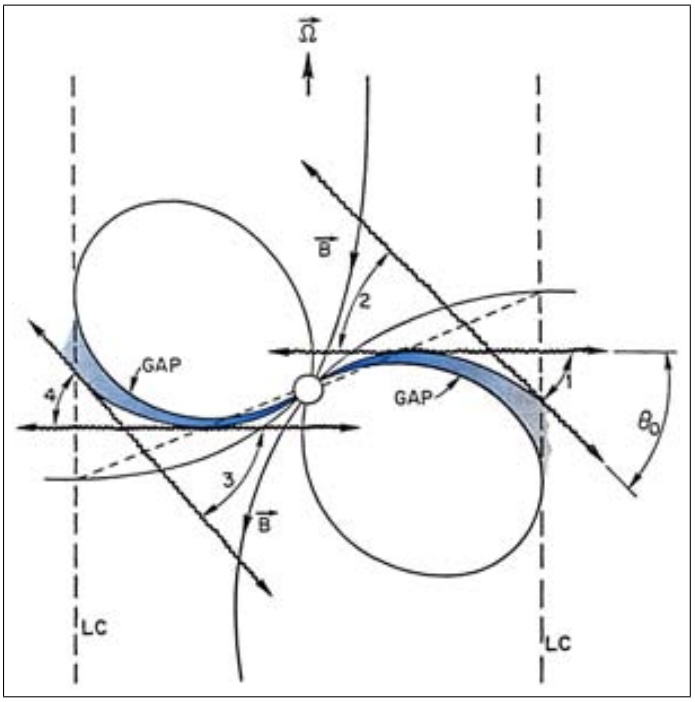

Figure 2.10
Sketch of the magnetosphere following the outer gap model from Cheng et al. (1986). Only two of the four gaps are highlighted. γ-rays stream out of the cones 1,2,3 and 4.

Classification

The classification scheme of Active Galactic Nuclei is shown in Fig. 2.12. It starts with a division based on the *radio-loudness* parameter $R = F_5/F_B$, where F_5 is the radio flux at 5 GHz and F_B the optical flux in the B band.
About 80–90% of the AGN sample is "radio-quiet" with $R \approx 1$, while the other 10–20% is "radio-loud" with $R \approx 100$.

A further division is based on morphology: elliptical versus spiral galaxies. Radio-quiet spiral AGNs with strong optical emission lines are called Seyfert galaxies (Seyfert, 1943) and can be further divided depending on the width of their optical emission lines: broad-lined Seyfert-I and narrow-lined Seyfert-II.

Radio-loud and radio-quiet elliptical AGNs showing emission lines are called "radio Quasars" and "radio-quiet Quasars", respectively; the former can be further divided into "flat-spectrum radio Quasars" (FSRQ) , and "steep-spectrum radio Quasars" (SSRQ) , depending on the steepness of their spectrum in radio.

Radio-loud elliptical AGNs having no or weak optical emission lines are called "Faranoff-Riley" galaxies when they display radio lobes, with a further subdivision into Type-I and Type-II based on the ratio of the distance of hotspots in the lobes to the total extent of the radio source (Fanaroff and Riley, 1974).

BL-Lac objects, finally, are radio-loud elliptical AGNs named after their prototype galaxy, BL Lacertae. They show no radio lobes, a flat radio spectrum, optical polarization up to 20%, strong variability on all wavelengths and timescales and γ-ray

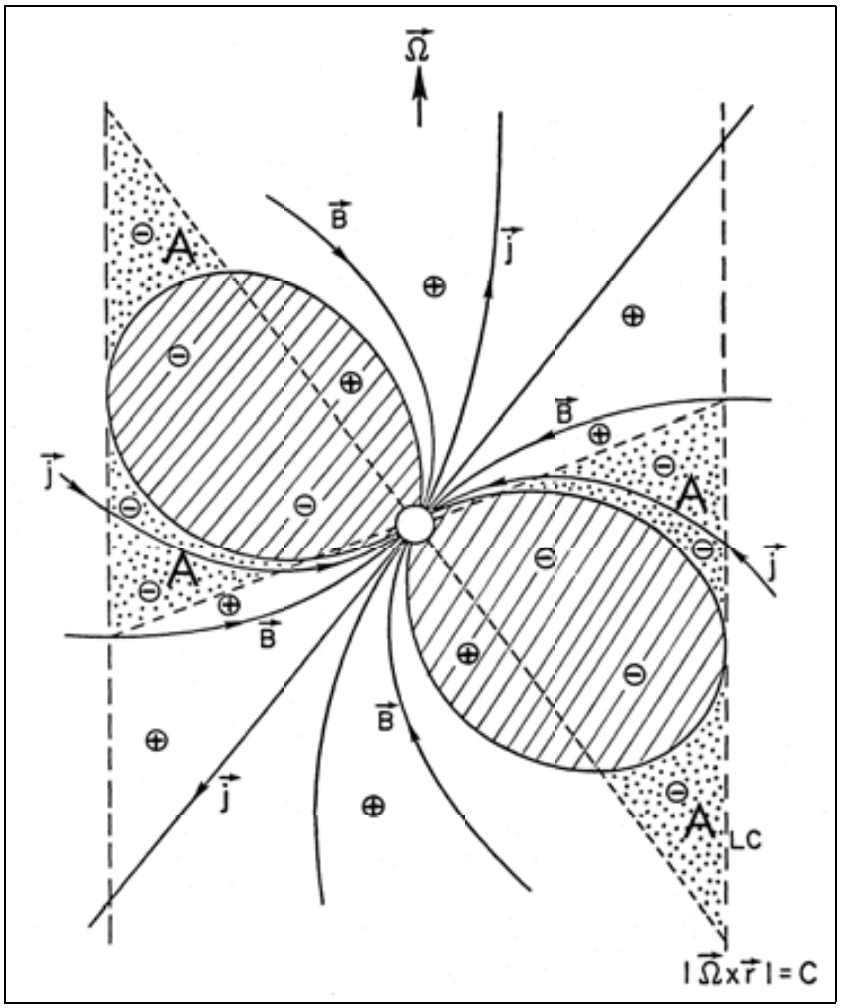

Figure 2.11
The assumed charge distributions and current flow patterns on open field lines of a spinning magnetized neutron star following the outer gap model from Cheng et al. (1986). In this case $\Omega \cdot \mathbf{B} < 0$ above the polar caps. The regions labelled "A" are the ones where negative current outflow form the light cylinder happens.

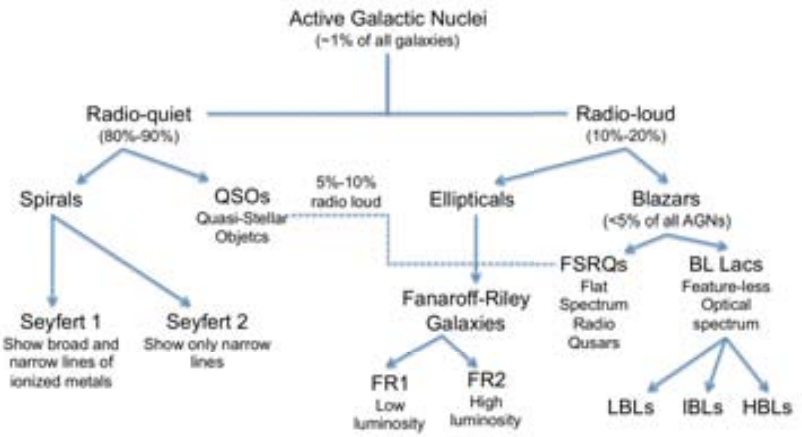

Figure 2.12
Classification scheme of AGNs, more details can be found in the text.

emission. Their spectral energy distribution (SED) consists of two broad peaks, or "bumps", one located at low energies (infrared to X-ray range) and the other at high energies (X-ray to VHE γ-ray range), as can be seen in Fig. 2.15. Depending on the energy at which the low energy peak is found, one can divide BL-Lac objects into low-peaked (LBL), intermediate-peaked (IBL) and high-peaked (HBL) (Nieppola et al., 2006).

BL-Lac objects share many of their characteristics with FSRQs, with the sole exception of the presence of strong optical emission lines. Therefore the two source types are often reunited into one class, the blazar source class.

The unified model

It is believed that the differences between blazars and all other AGN source classes can be explained by a common scenario: the so-called "unified model" (Antonucci, 1993; Urry and Padovani, 1995).

The structure of the AGN in the unified model can be seen if Fig. 2.13. It consists of 7 main components:

Central Black Hole (BH)

A supermassive black hole (SMBH, Lynden-Bell, 1969), with mass between 10^6 and 10^9 $M_\odot$, and a radius of $\sim 3 \times 10^{11}$ m, or about 5 light-minutes. It is the "engine" of the AGN, accreting matter from the surroundings, converting gravitational energy in kinetic energy. Already in 1963 it was speculated that black holes powered quasars, due to the high energy efficiency of the mass accretion process (Zel'dovich and Novikov, 1964; Salpeter, 1964). Most or all massive galaxies are believe to host a supermassive black hole in their center: the mass M of the black hole correlates well with the velocity dispersion σ of the galaxy bulge (the M-σ relation). A SMBH becomes active when sufficient material starts accreting onto it.

Accretion Disk

The accreting matter distributes itself on a rotating disk around the BH. The rotation velocity and the temperature of the disk both increase closer to the BH: the entire emission of the disk is thermal, and is a superposition of black body spectra from matter at different temperatures, peaking in the optical and UV bands, the so-called "blue bump" (Shields, 1978; Malkan and Sargent, 1982). The radius of the emitting region is estimated to be between 10^{12} and 3×10^{13} m, or between 1 light-hour and 1 light-day. There is observational evidence supporting its existence (Marscher et al., 2002).

Electron Corona

A spherical shell of extremely hot (tens up to hundreds keV) electrons surrounds the accretion disk. The electrons upscatter UV photons from the disk via the inverse Compton process, leading to X-ray emission (Haardt and Maraschi, 1991; Zdziarski et al., 1994, 1995).

Broad Line Region (BLR)

The BLR is a fast-moving (1–25 $\times 10^6$ m s^{-1}) cloudy gas shell, located close to the central region, at 2–20 10^{14} m (few light-weeks) away. The gas is illuminated by the disk, and emits Doppler-broadened photo-ionization lines. Estimates of the mass of the BLR run as high as 10^3–10^4 $M_\odot$ (see Alloin et al., 2006, chapter 3, for a review).

Dusty Torus

A thick dusty region with a toroidal shape located 1 to 10 parsec away from the central black hole. It mainly emits in infrared, and absorbs most of the light coming from the disk, the corona and the broad line region. In the unified model, the absence of broad emission lines in Seyfert-II galaxies and Faranoff-Riley radio galaxies is due to the torus blocking our line of sight to the BLR.

Narrow Line Region (NLR)

It is a region of slowly moving gas located at about 100 parsec from the center. The gas emits photo-ionization lines just like the BLR, however Doppler widening is less pronounced in this case due to the slower motion, and the lines are narrower.

Jet

By far the most prominent structure in an AGN, the jet is a relativistic, collimated plasma outflow, extending few kiloparsec to megaparsec into the intergalactic space. Twin jets extending from both sides of the AGN can be appreciated only when the jet points at a large angle to the line of sight, otherwise only the approaching jet is visible.

Jets are thought to be composed mainly of electrons, with a smaller proton (and pion/muon) population. The bulk of AGN non-thermal emission across the whole electromagnetic spectrum is believed to come from the jet. In

blazars, jet emission almost completely masks the thermal emission from the surrounding galaxy, and most of the energy output (which for blazars is of the same order of magnitude than the Eddington luminosity, $\sim 10^{41}$ W) is emitted as γ-rays.

Due to its relevance, the physics of the jet is summarized in more detail in §2.2.3

In the unified model, the most important parameter in determining the differences between the AGN types is the viewing angle under which the AGN is observed. As shown in Fig. 2.13, this orientation effect is mainly due to the optically thick dusty torus surrounding the central region. Further relativistic beaming effects become important for jet emission when the viewing angle is small. In this picture, BL-Lac objects are at the AGNs whose jet is most collimated to the line of sight: we observe them "down the barrel", an idea put forward originally by Blandford and KHnigl (1979). FSRQs instead are seen under greater angles.

Other relevant parameters in this model are the mass and rotation of the black hole, and its accretion rate, especially in connection to the physics of the jet outlined in the next section. Table 2.1 shows a possible ordering of the AGN classes based on the viewing angle and the BH spin.

Table 2.1: Different AGN classes as predicted in the unification model suggested by Urry and Padovani (1995), in which viewing angle and spin of the black hole are the defining parameters.

	Optical emission line proprieties		
	Broad	**Narrow**	**Unusual**
Radio quiet	Seyfert-II, Narrow line X-ray galaxies	Seyfert-I, Radio-quiet Quasars	Broad line radio-quiet Quasars ?
Radio loud	Narrow line radio galaxies, Faranoff-Riley I & II	Broad line radio galaxies, SSRQ, FSRQ	Blazars, BL-Lac objects, FSRQ

↓ BH spin ? ↓

→ Decreasing angle to line of sight →

The lack of radio-loud spiral AGNs could be explained by a different relative orientation (or lack) of the torus, disk and jet in these galaxies: since elliptical galaxies are thought to originate from the merging of spiral galaxies. It is conceivable (Barnes and Hernquist, 1991) that these mergers "activate" the galactic nuclei, however the primary mechanism responsible for it is still under debate, as observational evidence do not seem to support this hypothesis (Kocevski et al., 2012).

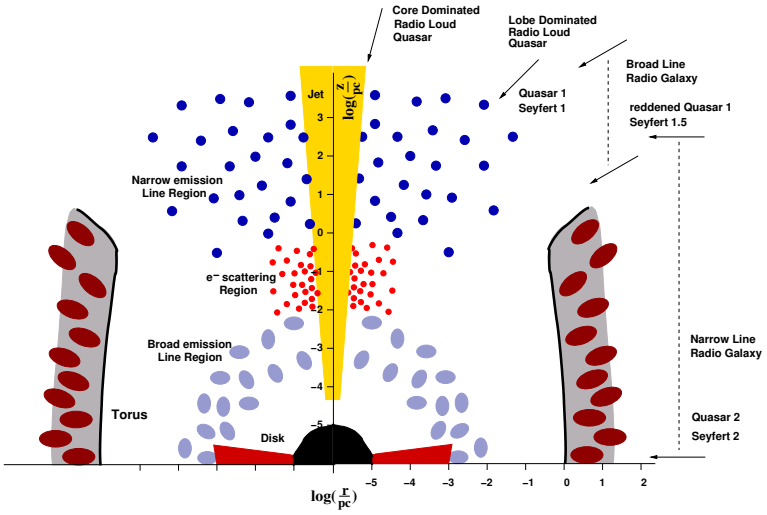

Figure 2.13
Structure of an AGN following the unified model. The geometry is not consistent with the scale, it is just to aid the eye. More details can be found in the text. Image from Biermann et al. (2002).

Jets

The physics of relativistic jets is still relatively poorly understood. In this section only a brief outlook is given; for an up-to-date monograph see e.g. Boettcher et al. (2011)

The formation of jets is the central problem, and still an open one. However some aspects of it are well established: it is believed to happen naturally in presence of a magnetized compact object accreting material, and an accreting disk with differential rotation: in current understanding, jets are a general feature of rotating, gravitationally confined plasma.

A widely accepted model of jet formation is due to (Blandford and Znajek, 1977): they show that energy and angular momentum can be electromagnetically extracted from the BH rotation, in a process that is similar to the ones found in pulsars.
Other magneto-hydrodynamic models have the angular momentum magnetically removed from the accretion disk (Blandford and Payne, 1982). Another model still (Blandford and Rees, 1974) ascribes the origin of the jet to the dynamical expulsion of material from the extremely dense regions surrounding the BH.

Jets extend for distances up to ten orders of magnitude bigger than the dimension of their engine, yet observational evidence show that they remain bright in spite of the expected adiabatic and radiative losses that their plasma should suffer along its path. They also remain remarkably collimated. A process responsible for acceleration of particles emitting radiation and collimation of the bulk material along a considerable portion of the jet is therefore required.

One of the possibilities is that the jet energy density and angular momentum is *Poynting-dominated*: acceleration would happen due magnetic driving (Vlahakis and Konigl, 2004; Sikora et al., 2005) in reconnection events. The jet would self-

collimate due to the toroidal component of the magnetic field (see e.g. the *Poynting outflow* model of Lovelace and Romanova, 2003), which follows the jet along at least part of its length with a helical field structure.

Another possibility is that jets are dominated by kinetic energy. The collimation would be consequence of the plasma propagating unperturbed in a ballistic regime for large distances in the intergalactic space. Particle acceleration would happen at in-jet shocks resulting from the interaction with denser external medium. Such shock-in-jet models could explain jet substructures such as the knots and hotspots observed at several wavelengths.

Due the relativistic nature of the jet, important effects arise. They can be understood in terms of the Lorentz factor γ, the angle between the direction of motion of the jet and the observer's line-of-sight θ, and the Doppler factor $\delta = \gamma(1 - \beta\cos\theta)^{-1}$ (in the case of a jet pointing towards the observer).

Aberration: just like for the synchrotron emission in §1.3.2, the light emitted from the jet in the observer's frame of reference is further collimated due to aberration effects: the solid angle of the emission is reduced by a factor δ^{-2} with respect to the co-moving frame: $d\Omega = d\Omega'/\delta^2$. The higher the Doppler factor of the jet, the narrower its emission cone. For solid angles, the emission

Time contraction: time intervals in the reference frame of the observer are different by a factor δ^{-1}: $\delta t = \delta t'/\delta$: event duration is shortened when the jet is pointing towards the observer, lengthened if it is pointing away.

Frequency shift: the above time contraction affects the frequency of electromagnetic waves emitted by the source (δ' in the co-moving frame): they are red-shifted or blue-shifted when the emission zone is moves away or towards the observer, respectively. In both cases $\delta = \delta\delta'$. If a source is located at cosmological distances, the frequency (and energy) is red-shifted due to Hubble's law: $\delta = \frac{\delta\nu}{z+1}$, where z is the redshift parameter.

Superluminal motion: in some cases, the components of the jet appear to travel with speeds greater of light. This superluminal motion is of course only apparent, and happens because the emission region almost "catches up" with its own emission. If the absolute velocity of the emitting region is v, its transverse component is: $v = \gamma\delta v \sin\theta$

The above effects explain why some AGNs show two jets structures, while in other ones only one jet is visible. If the jet emission in the co-moving frame has a power-law spectrum $L(\delta') \propto \delta'^{-\alpha}$ with spectral index α, and the all AGNs have twin jets emitted at the same angle in different directions, then the emission from the receding jet is less luminous by a factor $(1 - \beta\cos\theta)/(1 + \beta\cos\theta)^{n+\alpha}$, with $n \approx 2 - -3$. If the viewing angle θ is sufficiently small, the luminosity of the receding jet can be lower than the detection threshold, explaining the observational evidence of one-sided structures.

Blazar VHE γ-ray emission models

Blazar electromagnetic emission is dominated by non-thermal γradiation coming from the jet. While the low-frequency peak of the spectral energy distribution is commonly attributed to synchrotron radiation, the modeling of the high energy peak can follow two different approaches, depending on the type of particles responsible for the emission: *leptonic* models assume them to be electrons and positrons, while in *hadronic* models protons are the interaction partners. Mixed, *lepto-hadronic* models also exist.

Leptonic models In leptonic models the γ-ray peak is explained in terms of inverse Compton scattering of lower energy photons by relativistic electrons (and positrons) in the jet. Depending on the origin of the seed photons, leptonic models can be further divided into *external* inverse Compton (EIC) , and *self-synchrotron* Compton (SSC, Maraschi et al., 1992) .

In EIC models the seed photons can be infrared, optical and UV photons from thermal radiation of the disk, illuminating directly the jet or scattered on surrounding gas and dust clouds. Also photons of the cosmic microwave background can play a role (IC-CMB model, Tavecchio et al., 2000). Observational evidence (in the form of lack of strong emission lines) suggests that these ambient photon fields are not so important, at least for BL Lac objects. Therefore the EIC contributions are expected to be relevant only for FSRQs.

In SSC models the same population of electrons produces via synchrotron radiation the seed photons that it will later scatter via inverse Compton (Jones et al., 1974). In this model the electrons "work" twice: if the electron distribution is a power-law with normalization factor ⊠, $n(E)\mathrm{d}E = \boxtimes E^{-p}\mathrm{d}E$, it is expected that the SSC spectrum depends on $\boxtimes^2$.

The SSC emissivity is found substituting $U_{\mathrm{ph}}(\boxtimes)$ in equation 1.30 with the energy density of synchrotron radiation, proportional to the synchrotron emissivity (equation 1.48) times the average photon source crossing time R/c, where R is the size of the source. The general result is:

$$J_{\mathrm{SSC}}(\boxtimes) \propto \sigma_T \boxtimes^2 \boxtimes^{-\alpha} RB^{\alpha+1} \int_{\nu_{\mathrm{min}}}^{\nu_{\mathrm{min}}} \frac{\mathrm{d}\boxtimes'}{\boxtimes'}, \tag{2.21}$$

where $\alpha = (p+1)/2$, and the predicted dependence on $\boxtimes^2$ is apparent.

Writing the result of the integral in the above equation as $\ln\boxtimes$, and the Thomson optical depth as $\tau_T = \sigma_T R\boxtimes$, the ratio of synchrotron to SSC emissivity in the Thompson regime is $\sim \tau_T \ln\boxtimes$, as can be seen in Fig. 2.14.

The high energy peak is displaced by a factor γ^2 with respect to the low energy peak. A rough mapping of the peaks is given in Krawczynski et al. (2004):

$$\frac{E_{\mathrm{IC}}}{1\,\mathrm{TeV}} \approx \left(\frac{\boxtimes/10}{B/5\times10^{-6}\,\mathrm{T}}\right)^{1/2} \left(\frac{E_{\mathrm{syn}}}{1\,\mathrm{keV}}\right)^{1/2}, \tag{2.22}$$

where E_{SSC} and E_{syn} are the self synchrotron Compton energy measured in TeV and the synchrotron energy measured in keV, respectively. In the Klein-Nishina part of the Compton peak, the luminosity is suppressed, since the limits of the integration in equation 1.33. This affects the interpretation of the luminosity ratio of the two bumps L_{syn}/L_{IC}, and correlation between the frequency of the low energy peak and L_{syn}/L_{IC} is expected.

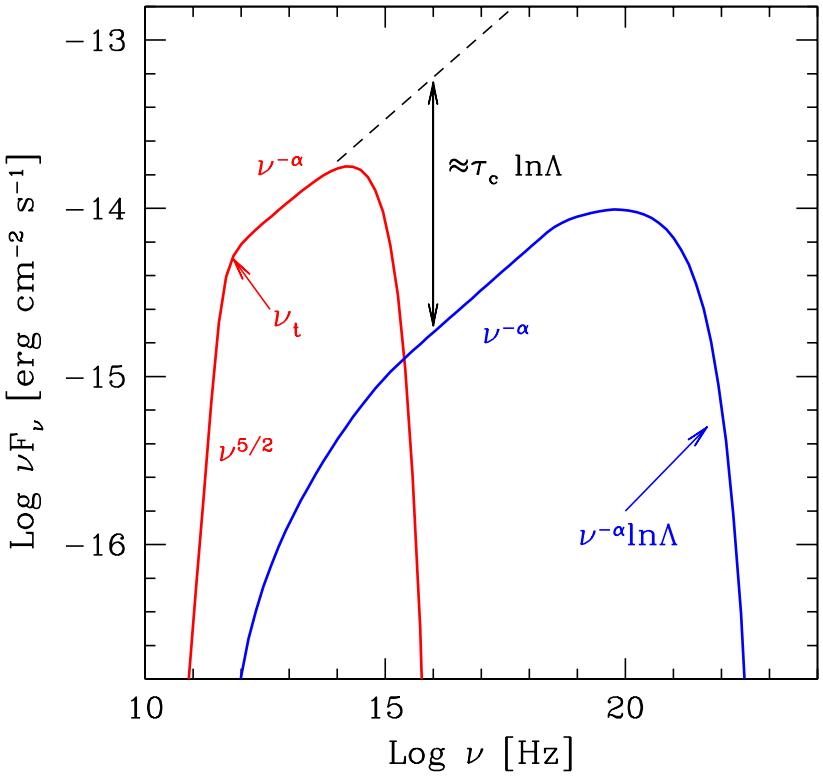

Figure 2.14
An example of SSC spectrum. Plotted is νF_ν representation, the self absorption frequency ν_t (found in eqn. 1.52) and the ratio between the synchrotron (red) and the SSC peak (blue) $\tau_c \ln\Lambda$ are indicated, together with the spectral indexes of the respective fluxes F_ν found in the text. The figure is from Ghisellini (2012).

SSC models have been successful in explaining the TeV γ-ray emission of many BL-Lac objects (see e.g. Tavecchio et al., 2001, and chapter 4), even though they underestimate the VHE emission of FSRQ (where EIC contributions are important).

In the simplest case of a one-zone SSC model, observations of both the synchrotron flux and the SSC flux are in principle enough to constrain some of the parameters of the source: for instance, the Doppler factor δ of the jet can be obtained from equations 1.49 and 1.52, which after taking into account the proper dependencies, become:

$$F^{syn}_{thin} \propto \theta^2 R \delta B^{1+\alpha} \delta^{-\alpha} \delta^{3+\alpha} \tag{2.23}$$

$$F^{syn}_{thick} \propto \theta^2 \frac{\nu_t^{5/2}}{B^{1/2}} \delta^{1/2} \tag{2.24}$$

therefore the SSC flux at Compton frequencies is:

$$F_{SSC}(\nu) \propto F_t^{22+\alpha} \nu_t^{-\ 5+3\alpha}\ \theta_s^{-2\ 3+2\alpha}\ \nu^{-\alpha} \delta^{-2\ 2+\alpha}\ , \tag{2.25}$$

comparing the synchrotron and the SSC flux, one can therefore estimate the Doppler factor . More details on the relationship between SSC model parameters and the SED of the sources is given in §2.2.5

Hadronic models In hadronic models (e.g. Mannheim and Biermann, 1992) the particles responsible for the high-energy peak of the spectrum are protons, accelerated in the jet together with electrons up to extremely high energies (E 10^{18} eV). The low energy emission is still synchrotron radiation from electrons, but the processes responsible for the high-energy emission are hadronic.

The most important interaction processes of protons with photons, and/or matter are:

- Photo-meson production: $p + \gamma_{\rm tgt} \rightarrow p + n, \pi, K, \rho, \ldots$;
- Bethe-Heitler pair production: $p + \gamma_{\rm tgt} \rightarrow p + e^+ + e^-$;
- p p inelastic interactions: $p + p_{\rm tgt} \rightarrow p + p + n, \pi, K, \rho, \ldots$;
- Proton synchrotron: $p + B \rightarrow p + \gamma s$

Typically the relative importance of the above interaction processes depends on the photon density and the magnetic field density (and the matter density for the inelastic interactions). If the target photon fields are dense, the protons give rise to lepto-hadronic cascades and to purely synchro-Compton pair cascades. In both cases charged particles in the cascade emit the bulk of HE/VHE γ-rays to synchrotron radiation (the synchrotron proton blazar model MXcke and Protheroe, 2001). In the case of target photon fields with low densities, it is possible that most HE/VHE γ-rays come from proton synchrotron radiation. This is thought to be the case for extreme BL-Lac objects. The target photons field can be internal to the jet, or external. In the latter case (Bednarek and Protheroe, 1999, e.g.), the threshold would be lower because the external radiation field would be blue-shifted in the frame of reference of the jet.

In some cases (e.g. for 3C 279, see BHtcher et al., 2009; Aleksi et al., 2011b) hadronic models are appealing because the understanding of the spectral energy distribution in terms of a one-zone SSC model is problematic. However their overall significance in a broader view is that they would offer an excellent explanation for the presence of ultra-high energy cosmic-rays.

A common characteristic of hadronic models is that they require extreme conditions, with jet powers of the order of 10^{41} W, and usually very intense magnetic fields much greater than 1 mT, high target radiation densities, or both. Another inconvenience is their inability to account for correlation between X-rays and γ-rays emissions, and the fast variability observed in some blazars (e.g. Aharonian et al., 2009).

A possible solution of the above issues is the merging of both models, since an admixture of hadronic and leptonic acceleration could be present in blazar jets at the same time. In these *lepto-hadronic* models, the hadronic component provides the base flux, while the leptonic accounts for the fast variability.

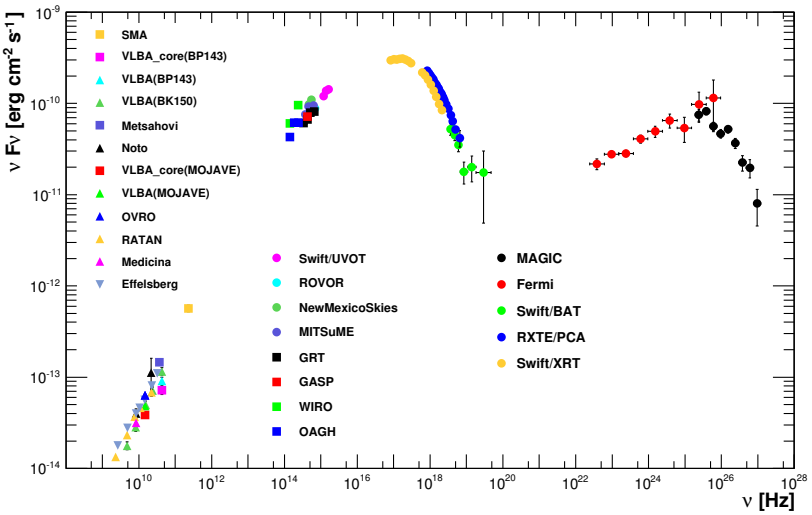

Figure 2.15
Multi-wavelength spectral energy distribution of one of the brightest TeV blazar, Markarian 421, from (Abdo et al., 2011) and references therein.

SSC models of the Spectral Energy Distribution of Blazars

As already mentioned, the twin peaked structure that characterizes the SED of TeV blazars is generally interpreted in the framework of the SSC models. The simplest version of this model (Tavecchio et al., 1998; Kino et al., 2002), dubbed "one-zone" SSC, considers a single, homogeneous region inside the jet as source of γ-ray photons. This region is approximated as a spherical "blob" filled with relativistic electrons with a number density ρ, with radius R and a bulk Doppler factor ⊠. This region is responsible for both the synchrotron and the inverse Compton emission.

In order to take into account synchrotron cooling effects, the spectrum of electron population inside the blob is modeled as a broken power law between a minimum and a maximum energy ($E_{\rm min}$ and $E_{\rm max}$), with break at $E_{\rm b}$ (to these energies correspond the Lorentz factors $\gamma_{\rm min}$, $\gamma_{\rm max}$ and $\gamma_{\rm b}$):

$$N_e(\gamma) = \begin{array}{ll} ⊠\gamma^{-n_1} & \text{if} \quad \gamma_{\rm min} < \gamma < \gamma_{\rm b} \\ ⊠\gamma^{-n_2} & \text{if} \quad \gamma_{\rm b} < \gamma < \gamma_{\rm max} \end{array} \tag{2.26}$$

The index before the break is $n_1 \approx 2$ (corresponding to the expected value for shock acceleration processes, see §1.3.1), and after the break it changes by one unit becoming $n_2 \approx 3$, a steepening due to the radiative cooling. The spectrum normalization ⊠ can be calculated from $\rho = \int_{\gamma_{\rm min}}^{\gamma_{\rm max}} N_e(\gamma) {\rm d}\gamma$.

In the simplest models γ_b can be taken as a free parameter, but it can also be calculated from the equilibrium of electron injection, cooling and escape rate, given some assumptions on the electron transport processes (see Tavecchio et al., 1998).

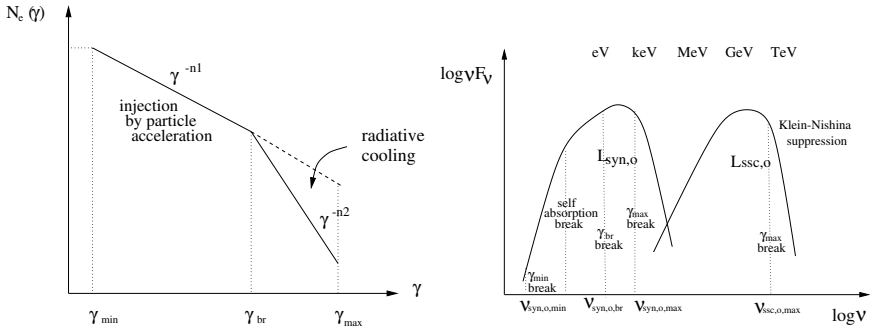

Figure 2.1 Electron spectrum and resulting photon spectrum for a simple one-zone SSC model, such as From (Kino et al., 2002).

(a) Injected electron spectrum **(b)** Resulting photon spectrum

This model is completely described by eight parameters relative to the "blob": R, ρ, B, n_1 ,n_2, $\gamma_{\rm min}$, $\gamma_{\rm max}$, $\gamma_{\rm b}$), one relative to the source, the Doppler factor δ, and one relative to its distance, the redshift z.

SSC models can be constrained by the observations of the following blazar SED observables (see also Fig. 2.14):

- the spectral index α of the "left" part of the two peaks;
- the peak frequencies of the synchrotron bump $\nu_{\rm syn}$ and of the Compton bump $\nu_{\rm SSC}$;
- the self-absorption frequency ν_t, that can constrain magnetic field and (equation 1.54) and the Doppler factor, as in equation 2.24;
- the luminosities of synchrotron and the SSC peaks, whose ratio $L_{\rm syn}/L_{\rm SSC}$ is connected to the ratio of the densities of magnetic field and synchrotron photons $\frac{U_{\rm B}}{U_{\rm syn}}$,
- the indexes at both sides of the Compton peak, when measured at GeV and TeV energies, can help constrain the redshift z of blazars of unknown distance (see Prandini et al., 2010).

The trends that the SSC model predicts are:

- a correlation between the peak frequencies $\nu_{\rm syn}$ and $\nu_{\rm SSC}$ as: $\nu_{\rm SSC} \approx (4/3)\gamma_{\rm b}^2 \nu_{\rm syn}$;
- $\nu_{\rm syn}$ should correlate with the luminosity ratio $L_{\rm syn}/L_{\rm SSC}$, as more synchrotron photons suffer Klein-Nishina suppression.

A third trend that was noted in the past was the anti-correlation between blazar luminosity and the position of the synchrotron peak, interpreted in the framework of the so-called *blazar sequence* (Fossati et al., 1998; Ghisellini et al., 1998) as an effect due to the increased cooling efficiency of more luminous sources. The classification between LBL, IBL and HBLs stems from this idea. Later works however ascribe this

effect to a sampling bias (Padovani et al., 2003; Caccianiga and March•, 2004; Ant⊠n and Browne, 2005).

An important aspect of blazar physics in general is variability. From causality arguments it is possible to constrain the size of the emitting region R from the minimum variability timescale $t_{\rm var}$:

$$R < c t_{\rm var} ⊠/(1+z)$$

Also, the contemporaneity of flares at different wavelengths (e.g. X-ray and γ-ray) would point to a common origin of the radiation, thereby confirming the predictions of SSC models;

A requirement which is implicitly present in the model and that can constrain the Doppler factor is that of γ-ray transparency: the photons must be able to leave the source. What impedes them to do so is internal absorption due to the production of pairs (see §1.4).

The energy threshold of this process (equation 1.61) can be surpassed in case of VHE γ-rays impinging on infrared photons: in the case of head-on ($\theta = \pi$) collisions, the cross section for pair production of γ-ray photons of energy E_γ on target ambient photons of energy $E_{\rm trg}$ becomes maximal when

$$E_{\rm trg} = E_{\rm max} = \frac{(2 m_e c^2)^2}{E_\gamma}, \tag{2.27}$$

corresponding to a wavelength of:

$$\lambda_{\rm max} \ ⊠{\rm m} \ \approx 1.24 E_\gamma \ \ {\rm TeV} \ . \tag{2.28}$$

There is however not a perfect one-to-one relationship, since the probability of interaction with target photon of shorter wavelength is not negligible, as can be seen in Fig. 1.20.

Relativistic aberration reduces however the chances of a head-on collision, since γrays can only interact with the ambient photons that lie within the narrow beaming cone of angle $\sim 1/⊠$. Therefore, the requirement of source transparency for VHE γ-rays implies a lower limit on ⊠, as shown in Dondi and Ghisellini (1995).

Oftentimes, a simple one-zone SSC modeling fails, especially in when considering multiple flares of a single blazar. In fact, it might be an oversimplification of the problem, since the emitting region can be non-homogeneous: it can for instance have different magnetic field intensities, or varying Doppler factors, with the jet having a fast spine a slower sheath (Celotti et al., 2001). While appealing, these models have more free parameters, therefore less predictive power. They can be constrained only by long-term simultaneous multi-wavelength observations.

The Extragalactic Background Light

γ-ray absorption processes due to pair creation can happen outside the source: high-energy photons can interact with photons of the cosmic background radiation (CBR)

covering most of the electromagnetic spectrum with varying intensities, as can be seen in Fig. 2.17.

.

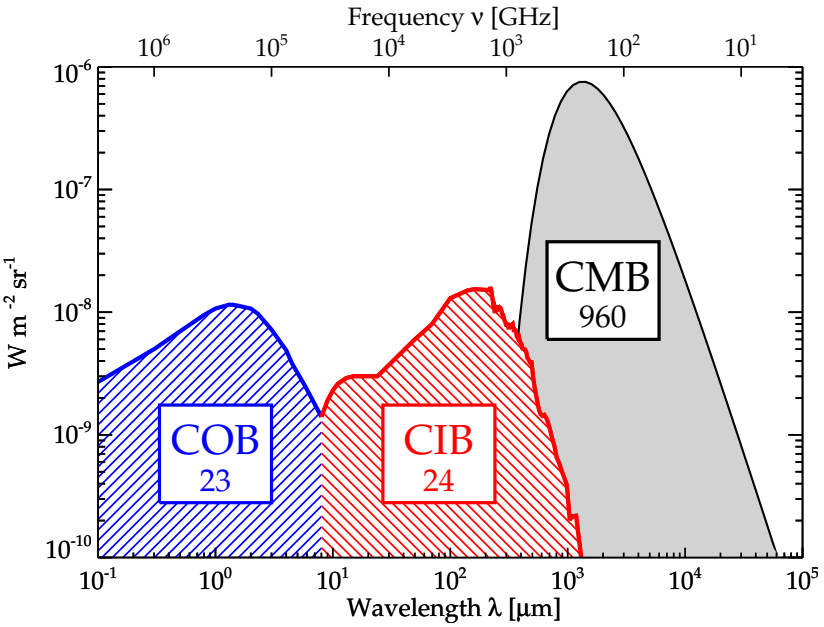

Figure 2.17
Schematic spectral energy distribution of the most important components of the CBR, the Cosmic Optical Background (COB), Cosmic Infrared Background (CIB), and the Cosmic Microwave Background (CMB), with the corresponding approximate brightness in units of nW m sr^{-1}. COB and CIB together form the EBL, and are thought to be due to starlight and dust-reprocessed starlight. From Dole et al. (2006).

The wavelength range of CBR photons responsible for the attenuation of VHE γrays can be estimated from equation 2.28: γrays with energies above 80 GeV are absorbed predominantly by background photons in the ultraviolet to infrared wavelength range, commonly referred to as extragalactic background light (EBL), . The higher the γ-ray energy, the greater the wavelength of the EBL photons responsible for most of the absorption[1].

A good knowledge of EBL is important to understand how this absorption affects the spectrum of distant sources seen in VHE γrays; conversely, observations of VHE sources can be used as a probe for the EBL.

The EBL spectrum extending from 0.1 to 1000 m is the second most energetic component of diffuse cosmic background radiation, with an intensity of about 5-10% that of the cosmic microwave background (CMB, see figure 2.17). Its spectrum, shown in Fig. 2.18, has two peaks: one in the optical and near infrared bands peaking at ~ 1 m, another in the far-infrared peaking at 100 m. The former is thought to be due to direct starlight, the latter to the thermal reprocessing of starlight by dust. Light from AGNs can contribute as well to both by about 10 20%, and possibly more in specific wavelength regions.

The EBL is difficult to measure directly, both because of the technical difficulty of determining the absolute diffuse sky brightness (which relates to the problem of de-

[1] As mentioned earlier, this dependency is not sharp, as the probability of photons of shorter wavelength to absorb the γray is not negligible

termining an absolute zero-flux level eliminating all instrumental background), and because of the presence of brighter local foreground sources, such as the zodiacal emission in the infrared from interplanetary dust, or the light from very dim stars in our milky way.

Currently the measured EBL spectrum has an uncertainty that varies between 20% and 80%. Comprehensive reviews of EBL measurements and limits can be found in e.g. Hauser and Dwek (2001) and Kashlinsky (2005).

Direct measurements of EBL to date have been carried on by dedicated satellite-borne detectors flown in the 1990s, the DIRBE and FIRAS instruments on board the COBE satellite (Boggess et al., 1992) and the NIRS spectrometer on the Japanese IRTS (Murakami et al., 1994).

Lower limits on EBL have been extracted by source counts in deep infrared field observations, or stacked analysis of extensive infrared surveys, while upper limits on the EBL are given by the detection of HE and VHE γrays from distant blazars, and the measurement of attenuation signatures on their spectra.

EBL models The EBL is an integrated measure of cosmic activity, since the diffuse spectrum at the present time contains the photons produced along the history of the cosmos since the epoch of re-ionization[] at roughly $6 < z < 20$.

Therefore most of the present models try to infer the EBL luminosity density as a function of z. The models differ mainly on the treatment of the luminosity function, number evolution, spectral evolution of galaxies, since stars in galaxies are the most important contributors to the EBL:

Backward evolution models extrapolate the well-measured spectra of local galaxies backwards in time, as a function of $(1 + z)$. The parametrization for the extrapolation makes no assumption on the underlying physics, instead uses averaged spectral galaxy templates. The galaxy luminosity functions are instead taken from observations. A recent examples of a backward evolution model is that of Franceschini et al. (2008).

Forward evolution models simulate the temporal evolution of galaxies in redshift space using models for both the galaxy luminosity function and spectral evolution that rely on several cosmological conditions and a wide body of computational and observational data stretching across many areas of astrophysics. Due to uncertainties on many of the parameters involved, these models lack the predictive power of simpler models, however they are appealing since they provide for a self-consistent picture of the origin of the EBL. Recent examples of these type of models include Kneiske and Dole (2010) (inferred evolution) and Gilmore et al. (2012) (semi-analytical).

[]The second phase transition that occurred during the evolution of the universe, when the light of the first stars was energetic enough to ionize monoatomic hydrogen

Observed evolution models are, as the name suggests, models in which the evolution of galaxies is interpolated from observed data. The spectra of observed galaxies are divided in several types, whose relative fraction evolves with the redshift. Extrapolations are used for redshifts higher than ~ 1, when data starts to be missing. The obvious advantage of this models is that they stem only from observations, however they cannot offer direct constrains on other fields. An example is the model by Dom¯nguez et al. (2011)

Most of the recent models agree well (within 20%) in the near infrared region of the spectrum, but disagreements can be as high as a factor 2 in the far infrared region, as can be seen from Fig. 2.18.

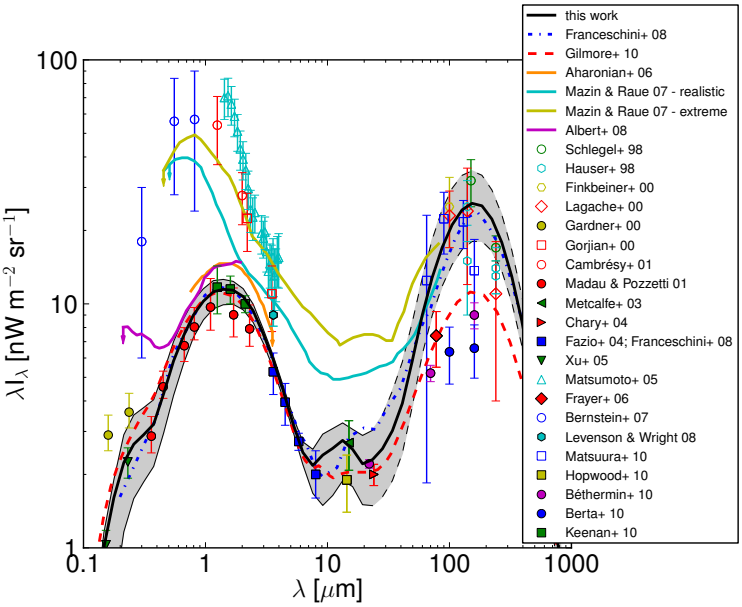

Figure 2.18
A comparison of recent EBL models, with data from source counts and direct measurements. It is believed that the older measurements in the near infrared (empty markers) suffer from a poor subtraction of the background (Mattila, 2006). From Dom¯nguez et al. (2011).

EBL and VHE γrays The effect of EBL on observed VHE spectra $I_{\rm obs}(E)$ can be described as an exponential attenuation of the intrinsic one $I_{\rm intrinsic}(E)$:

$$I_{\rm obs}(E) = I_{\rm intrinsic}(E) \times \exp(-\tau(E,z)). \tag{2.29}$$

$\tau(E,z)$ is the optical depth; and it is a function of the γ-ray photon energy $E$and of the source redshift z:

$$\tau(E,z) = \int_0^z \frac{\mathrm{d}\boxtimes(z')}{\mathrm{d}z'}\mathrm{d}z' \int_{-1}^{+1} \mathrm{d}\mu \frac{1-\mu}{2} \int_{\boxtimes_{\rm thr}} \mathrm{d}\varepsilon' n_{\rm EBL}(\varepsilon', z')\sigma_{\gamma\gamma} \quad E', \varepsilon', \mu \quad . \tag{2.30}$$

The first integral takes into account the distance travelled (which depends on the cosmological parameters one assumes), the second the interaction angle ($\mu = \cos\theta$) and the third the interaction probability, proportional to the product of the EBL photon number density in the comoving frame $n_{\rm EBL}(\varepsilon, z)$, and the pair production

cross-section $\sigma_{\gamma\gamma}$, integrated over the EBL photon energy ε starting from the integration threshold of $\varepsilon'_{\rm thr} = \varepsilon_{\rm thr}(E', \mu)$. Primed quantities correspond to redshifted values, so in the third integral $E' = E(1 + z')$.

It is very important to note that while direct measurements give constrains on the local background, VHE γ-ray measurements can probe also its evolution with the redshift since the observed spectra bear the signature of the EBL density integrated along z.

The VHE γ-ray spectrum of a far away blazars can constrain the EBL: upper limits can be calculated excluding EBL intensities that would cause the intrinsic spectrum $I_{\rm intrinsic}(E)$ (obtained inverting equation 2.29, a process known as de-absorption) to be unphysical.

One common requirement (see e.g. Mazin and Raue, 2007) is that the intrinsic spectrum must have a spectral index α 1.5: in fact VHE γ-ray measurements of blazars probe the falling (Klein-Nishina) slope of the inverse Compton bump, which must (in case of SSC models) be steeper than the synchrotron slope $\alpha = (1 + p)/2$, where p 2 is the spectral index for electrons accelerated in diffusive shock acceleration.
In more recent works (e.g. Meyer et al., 2012) tighter limits are obtained by requiring that the spectrum spanning from HE to VHE is concave, and that the total integral flux in the VHE region is smaller than the Eddington luminosity.

In summary, EBL modifies the measured spectra of distant blazars in the VHE γ-ray range; conversely, VHE γ-ray observations of blazars can be used to probe both the local and distant intensity of EBL, giving insights on the process of galaxy formation and evolution.

3. The MAGIC telescopes

This chapter will briefly describe the atmospheric imaging Cherenkov technique, starting from a description of the physics of particle showers in the atmosphere. An overview of the hardware and software pieces that make up the MAGIC telescopes is then given. Finally, the steps in the analysis of MAGIC data are listed and explained.

3.1 Air showers

An extensive air shower is a cascade of particle initiated by a very high energy cosmic and gamma rays interacting with the upper atmosphere. The nature of the primary particle (hadron or gamma-ray/electron) has a strong influence on the development of the shower in the atmosphere, since the interaction processes are fundamentally different.

Description of the atmosphere and shower equations

The atmosphere can be described in terms of X, the *slant depth*, a measure of the amount of matter a shower sees along its path l. As can be seen from Fig. 3.1, if the shower is vertical, the slant depth is equal to the vertical depth X_v of the atmosphere:

$$X_v(h) = \int_h \rho(z)\mathrm{d}z \tag{3.1}$$

where $\rho(z)$ is the density of the air at a height z. If we approximate $\rho(z)$ it with the exponential barometric formula $\rho(x) \approx \rho_0 \exp(-z/H)$, with $\rho_0 \sim 1.2$ kg/m^3 and the scale height $H \sim 8600m$, then the vertical depth is

$$X_v(h) \approx 10300 \exp(-\frac{h}{H}) \text{ kg/m}^2. \tag{3.2}$$

The slant depth can be calculated similarly as $X = \int_l \rho(h(l'))\mathrm{d}l'$ knowing that the relationship between h and the distance up the trajectory l,

$$h(l) = \cos\theta + \frac{1}{2}\frac{l^2}{R_\oplus}\sin^2\theta,$$

valid for $l \ll R_\oplus$, where $R_\oplus$ is the radius of the earth and θ is the zenith angle.

The probability P that a particle of energy E interacts in traversing an infinitesimal $\mathrm{d}X$ depth is $P\mathrm{d}X = \mathrm{d}X/\lambda(E)$, where $\lambda(E)$ is the mean *interaction length*, which relates to the total cross-section σ as:

$$\lambda(E) = \frac{\rho}{\rho_N \sigma(E)} = \frac{Am_p}{\sigma(E)},$$

where ρ and ρ_N are the mass and number density of the air, A its average mass number (approximately 14.5) and m_p the mass of the proton ($\sim 1.67 \times 10^{-27}$ kg. Then the number of particles interacting per unit height is:

$$\frac{\mathrm{d}N(E)}{\mathrm{d}X} = -\frac{N}{\lambda(E)}. \tag{3.3}$$

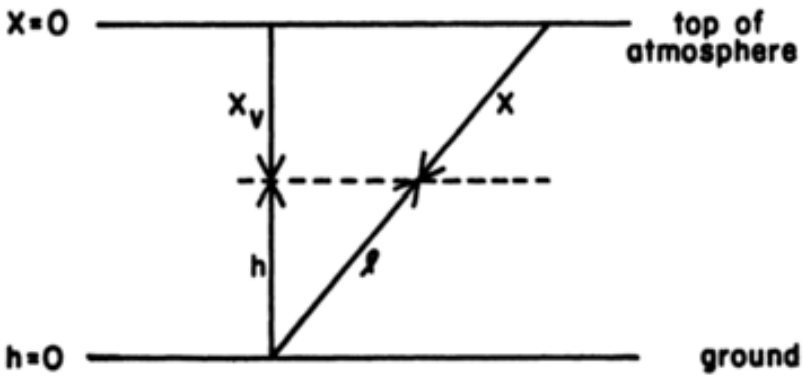

Figure 3.1
Parameters of the atmposhere relevant for the description of showers, from Gaisser (1990).

Equation (3.3 however does not tell the whole story: it does not take into account particle decay, particle production by previous interactions and the presence of multiple production and decay channels. In general terms showers can be described with a set of coupled differential equations:

$$\frac{\mathrm{d}N_i(E,X)}{\mathrm{d}X} = -\left(\frac{1}{\lambda_i} + \frac{1}{d_i}\right) N_i(E,X) + \sum_j \int \frac{F_{ji}(E_i,E_j)}{E_i} \frac{N_j(E_j)}{\lambda_j} \mathrm{d}E_j, \tag{3.4}$$

where:

- $N_i(E,X)$ is the number of particles of type i of energy E at a depth X;
- λ_i is the interaction length of a particle of type i;
- d_i is the *decay* depth, the mean depth X at which a particle with mean life τ_i undergoes decay, it is found inverting equation 3.2 for $h = \beta\gamma c\tau_i$
- $F_{ji}(E_i,E_j)$ is the dimensionless inclusive cross-section for a particle of type i with energy E_i to collide with an air nucleus and produc particle of type j outgoing with energy E_j, having an interaction length λ_j.

Further complications, such as the effect of the magnetic field of the earth on particle propagation and secondary energy loss processes quickly render the problem very difficult to treat analytically: for practical purposes it is customary to resort to Monte Carlo simulations, such as those shown in Fig. 3.3. In the following a brief qualitative description of hadronic and γ-ray-induced extensive air showers is given; more emphasis is given on results relevant for ground-based Cherenkov telescopes in the context of gamma-ray astronomy. A good, recent review on high energy hadronic showers is the one by Engel et al. (2011).

Hadronic showers

are dominated by hadronic iterations, such as pion and light meson production. A schematic illustration is shown in Fig. 3.2a. In the case of proton-proton interaction, the cross-section when the energy of the incident particle is between 3 GeV and 1 TeV can be approximated to $\sigma_{pp} \sim 40$ mb, which becomes $\sigma_{pA} \sim 45 A_2^{0.691}$ mb when the impinging particle is a proton and the target is a nucleus with mass number A_2. In the general case of nucleus-nucleus interaction, $\sigma_{AA} \sim 65(A_1^{1/3} + A_2^{1/3} + 1.12)^2$ mb, where A_1 is the mass number of the impinging nucleus.
In air ($A_2 \sim 14.5$) a cosmic proton in this energy range has a cross-section of 280 mb, and a corresponding interaction length of 850 kg/m^2, about twice the radiation length of bremsstrahlung X_B found in equation (1.35). Only one or two nucleons participate in proton-nucleus collision, leaving the nucleus in a highly excited state. The multiplicity N of a proton-proton collision as a function of the energy E is well approximated by $N \approx 1.97(E/1\ \mathrm{GeV})^{1/4}$ between few GeV and 10 TeV (Carruthers and Duong-Van, 1972), so a 1 TeV proton produces on average about 20 secondaries in a collision, with a typical, almost energy indipendent transverse momentum of ~ 0.3 GeV/c.
Most of the particles produced are pions and kaons: neutral pions decay almost immediately ($c\tau_{\pi^0} = 25$ nm) into two photons $\pi^0 \to \gamma + \gamma$, while charged pions undergo other nuclear interactions before decaying $\pi^\pm \to \mu^\pm + \nu_\mu/\bar{\nu}_\mu$, once $E_\pi \quad 30$ GeV. Kaons have shorter lifetime than pions and decay at higher energies. The shower has a high-energy *hadronic core*, composed predominantly by baryons and long-lived mesons with high forward momentum, and an electromagnetic component continuously fed by neutral pion decay. The hadronic component of the shower and its decay products have a wider lateral distribution than the electromagnetic one (see Fig. 3.2b), because that the transverse momentum of secondary hadrons is typically 0.3 GeV/c, indipendently of energy. The lateral spread of electrons and positrons is determined by multiple Coulomb scattering.
Muons and neutrinos are the components of the shower that suffer less energy losses and propagate to the surface of the earth and below it, and because of that are known as "hard" component, in contrast to the easily stoppable "soft" electromagnetic component. Neutrons are also produced in these interactions, but mostly via spallation or decay of the leftover nucleus, so they are emitted isotropically in the frame of

reference of the target nucleus. This is not true when the impinging particle is not a proton but a heavy nucleus: in that case the spallation product travel relativistically with it, and give rise to air showers with multiple hadronic cores.

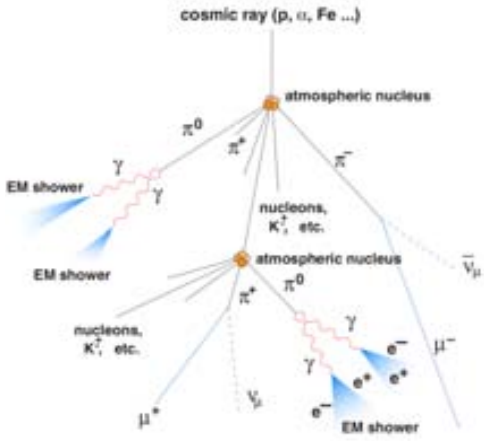

(a) Diagram of a proton-induced hadronic shower.

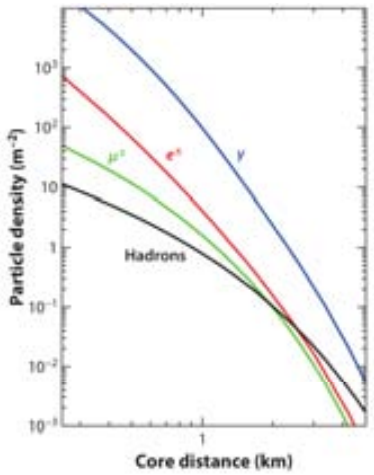

(b) Lateral shower profile

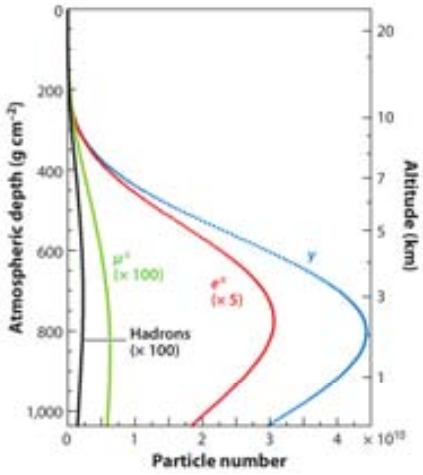

(c) Longitudinal shower profile

Figure 3.2
Schematic diagram (Wagner, 2006, 3.2a, from) and profiles of the development of a proton-induced hadronic shower. The particle shower profiles in 3.2b and 3.2c, are from Engel et al. (2011) and were obtained from a Monte Carlo simulation of an incident proton of energy $E = 10^{19}$ eV done with CORSIKA (Heck et al., 1998).

Electromagnetic showers

are initiated by a γ-ray or a high energy electron and differ from hadronic showers in a number of ways. If the incoming particle is a γ-ray of sufficient energy, it has a certain probability of interacting with the intense Coulomb field in the vicinity of a nucleus to give rise to an electron-positron pair. If it's an electron, it most probably radiates high-energy photons via Bremsstrahlung. The two processes alternate each other and give rise to a cascade exclusively composed by electrons, positrons and photons, until the electron (photon) energy becomes lower than the

critical energy E_c, defined as the energy at which the ionization losses (equation 1.57) equal the bremsstrahlung (pair production) losses (equation 1.35): for electrons in air $E_c \approx 87$ MeV, while for photons $E_c \approx 80$ MeV. Due to the small opening angles of pair production and bremsstrahlung, the electromagnetic cascade is slender and approximately axially symmetric about the direction of the primary.

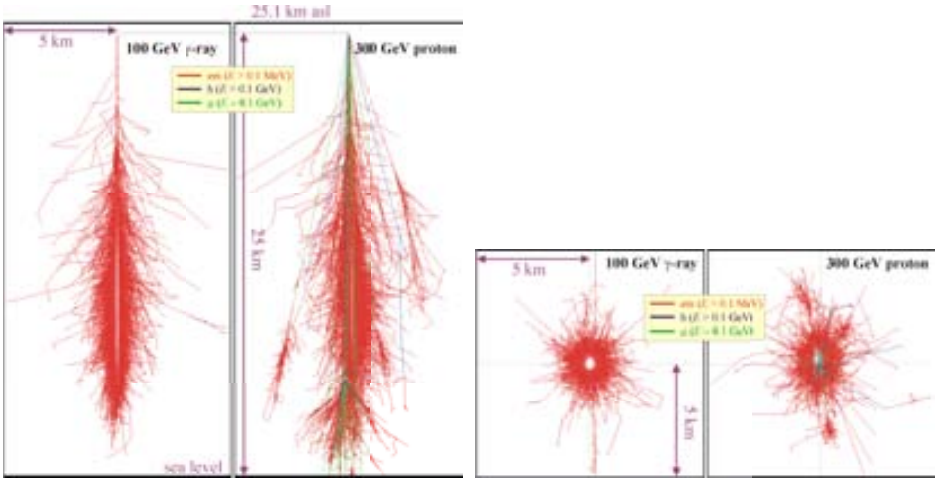

(a) Longitudinal development.

(b) Lateral development.

Figure 3.3
Simulations of electromagnetic (left) and hadronic (right) showers, with zero incident angle, and initial energy of 100 and 300 GeV, respectively. Shown are single particle tracks, in red the electromagnetic particles with energies above 0.1 MeV; in blue hadronic particles above 0.1 GeV and in green muons above 0.1 GeV. The height of the first interaction is 25 km a.s.l. (Hrupec, 2008; Schmidt, 2012).

Shower models

Most of the relevant features of an extensive air shower such as particle multiplicity and longitudinal development can be understood by a simple scaling model due to Carlson and Oppenheimer (1937), known as the Heitler model (Heitler, 1954). The model approximates bremsstrahlung and pair production as *splitting* events (see Fig. 3.4a): an incident electron with energy E undergoes splits into two photons after it travels a distance $\lambda_e = X_B \ln 2$ where X_B is the bremstrahlung interaction length in air (equation 1.35). A photon splits into a pair after travelling a similar length: it was shown in equation 1.63 that the ineraction length of pair production is longer than X_B by a factor $\frac{9}{7}$, but in first approximation this difference is negligible.
After one splitting, 2 particles are produced, whose energy is $E/2$, and the process is then repeated, until it abruptly stops at when the electron energy equals the critical energy $E = E_c$. At a given atmospheric depth X, the number of particle *generations* is $n = X/\lambda_e$, the particle multiplicity is $N(X) = 2^n$, and their energy is $E = E_0 2^{-n}$, where E_0 is the energy of the primary. Maximum particle number $N_{\max}$ and shower depth $X_{\max}$ are reached when $E = E_c$:

$$N_{\max} = \frac{E_0}{E_c} \quad \text{and} \quad X_{\max} = \lambda_e \ln(N_{\max}).$$

The model overestimates the actual ratio of electrons to photons (as was noted by Heitler). predicting that after a few generations $N_e/N_\gamma \to 2/3$, because it neglects

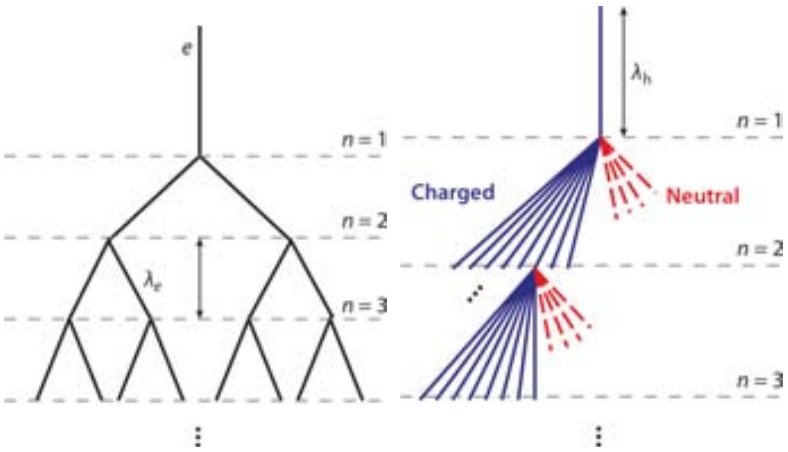

(a) Electromagnetic shower (Heitler model). (b) Hadronic shower (Heitler-Matthews model).

Figure 3.4
Simplified cascade model of electromagnetic and hadronic showers. The horizontal dashed lines show the generations, black lines represent electrons and photons, blue lines charged hadrons, and red dashed lines neutral pions. Figures from Engel et al. (2011).

multiple photon radiation during bremsstrahlung, and it doesn't describe too well the developmento of the muliplicites, nevertheless its predictions for the size of the shower and the position of its maximum are reasonable.
A more detailed analytical approach, due to (Rossi and Greisen, 1941), shows that the particle multiplicity along the particle axis first increases up to a maximum and then decreases. A modern approximation for the number of electrons in air N_e is:

$$N_e(t, E_0) = \frac{0.31}{\sqrt{\ln(E_0/E_c)}} \exp(t - 1.5t \ln s); \tag{3.5}$$

$$s = \frac{3t}{t + 2\ln(E_0/E_c)}; \tag{3.6}$$

$$t = \frac{X}{X_0}; \tag{3.7}$$

where t is the shower depth in units of X_0 and s is the shower *age*: $s = 0$ is the start, $s = 1$ (and $t = \ln(E_0/E_c)$) is the shower maximum, and $s = 2$ the end. All the above quantities are plotted in Fig. 3.5a.
More exactly, the longitudinal profile of the energy deposition for a certain particle type (γ, e) is well approximated by (Longo and Sestili, 1975; Beringer et al., 2012, see):

$$\frac{\mathrm{d}E}{\mathrm{d}t} = E_0 b \frac{(bt)^{a-1} e^{-bt}}{\Gamma(a)} \tag{3.8}$$

where b and a are fit parameters related by the maximum shower depth by

$$t_{\max} = \frac{a-1}{b} = \ln \frac{E_0}{E_c} \pm 0.5, \tag{3.9}$$

with '+' for γ-rays and '–' for electrons. This latter approach agrees well with numerical simulations, as can be can be seen in figure 3.5b

Shower fluctuations (in number of electrons) can be described by:

$$\boxtimes N_e(s) = \frac{9}{14} N_e(s)(s - 1 - 3\ln s). \tag{3.10}$$

The lateral development of the shower is instead influenced mainly by multiple scattering, as mentioned before; it is characterized by the Molière radius $r_M = x_B E_s / E_c$, where x_B is the bremsstrahlung radiation length (in meters) in the material and $E_s \approx 21$ MeV. In air $r_M \approx 79$m. The lateral distribution of electrons for $1 \quad s \quad 1.4$ is given by the Nishimura-Kamata-Greisen (NKG) formula:

$$\rho_e(r, t, E) = \frac{\Gamma(4.5 - s)}{2\pi\Gamma(s)\Gamma(4.5 - 2s)} \frac{N_e(t, E)}{r_M^2} \left(\frac{r}{r_M}\right)^{s-2} \left(1 + \frac{r}{r_M}\right)^{s-4.5}. \tag{3.11}$$

For hadronic showers, a generalization (Matthews, 2005) of the Heitler shower model can give some insights: in this model a hadron with energy E interacts and splits into n_{tot} particles, each with energy E/n_{tot}. Two thirds of the products are charged pions that continue travelling, while one third is neutral pions which decay immediatly into two photons, originating an electromagnetic (EM) shower (see Fig. 3.4b). The charged pions interact with other particles in the air after having travelled the mean hadronic interaction length λ_h, and the process repeats itself until the pions have reached a typical decay energy E_{dec}, after which they decay into muons.
At each splitting, about one third of the energy is transferred to the EM shower; after n splitting the energies in the hadroninc and EM components therefore are, respectively:

$$E_h = \left(\frac{2}{3}\right)^n E_0 \quad \text{and} \quad E_e = \left[1 - \left(\frac{2}{3}\right)^n\right] E_0.$$

At the sixth generation $n = 6$, about 90% of the initial energy is transferred to the EM component; and the EM sub-showers produced in the first interactions determine the depth of the shower maximum:

$$X_{\max,h} = \lambda_h + X_{\max,e} = \lambda_h + \lambda_e \ln\left(\frac{E_0}{n_{\text{tot}} E_c}\right).$$

The maximum number of generations is given by the hadronic component, similarly to the Heitler model:

$$E = \frac{E_0}{(n_{\text{tot}})^n} = E_{\text{dec}} \to n_{\max} = \frac{\ln(E_0/E_{\text{dec}})}{\ln n_{\text{tot}}}.$$

At the shower end the total number of electrons is the sum of all the EM sub-showers:

$$N_{\max,e} = \sum_{k=1}^{k=n_{\max}} \frac{E_0}{3^k E_c} = \frac{E_0}{E_c}\left(\frac{1 - 3^{-n_{\max}}}{2}\right),$$

while the number of muons is given by:

$$N_\mu = \left(\frac{2}{3} n_{\text{tot}}\right)^n_{\max} = \left(\frac{E_0}{E_{\text{dec}}}\right)^\alpha \quad \text{with} \quad \alpha = \frac{\ln \frac{2}{3} n_{\text{tot}}}{\ln n_{\text{tot}}} \approx 0.82 \ldots 0.94$$

This model can be applied to heavier nucleons quite straightforwardly: a shower induced by a nucleon with mass number A and initial energy E_0 is treated as the superposition of A hadronic showers with initial energy E_0/A. In this way it is possible to infer that the number of muons should be higher by a factor $A^{1-\alpha}$, so iron nuclei would produce 40% more muons than protons of the same energy.

Atmospheric Cherenkov Radiation

At ground level, the Cherenkov light from electromagnetic showers is observed in elliptical homogeneous distributions (*light pools*) with radii of 80-150 m and characteristic durations of few nanoseconds. Hadronic showers exhibit more widespread, heterogeneous structures.
The spectrum of this light has a maximum around 330 nm, shorter wavelengths are suppressed by different scattering processes and ozone absorption. The flux depends on the initial energy of the shower, a gamma-ray of 1 TeV results in around 100 photons/m^2 at 2000 m asl.

The atmosphere is not completely transparent for Cherenkov photons, so a certain fraction of them cannot reach the ground. Firstly, ozone exists in the atmosphere and absorbs ultraviolet photons. The absorption spectrum shows a broad peak around 250 nm and most of the Cherenkov photons with a wavelength below 300 nm are lost. Secondly, the air molecules cause Rayleigh scattering. It has a λ^4 dependency and mainly short wavelength photons are affected. Thirdly, aerosols such as dust and water droplets cause Mie scattering, which has a weak wavelength dependency and all the wavelengths are affected. The Cherenkov light spectra at 10 km (before absorption) and 2200 m a.s.l. (after absorption) are shown in Fig. 3.8.

3.2 The MAGIC telescopes

The Florian Goebel MAGIC Telescopes are two 17 m imaging atmospheric Cherenkov telescopes or IACTs, located at Roque de Los Muchachos on the Canary Island of La Palma. MAGIC-I started routine operation after commissioning in 2004. Construction of MAGIC-II has been completed in early 2009.

The MAGIC telescopes were designed with performance in mind: they have a very low energy threshold, thanks to their very big mirrors and the sensitivity of their photosensor camera, together with the selectiveness and small latency of the trigger system. They can sample showers using timing information, due to the synchonicity of the mirror surface and the high sampling speed of the Data Acquisition System. They can move very fast, because of the carbon fiber structure and the fact that the readout electronics is separated from the camera, making it very light.

The MAGIC telescopes are possibly the most technologically advanced atmospheric imaging Cherenkov telescopes currently operating, with the exception of HESS-II.

The structure

The telescope structure supporting the mirrors is a space frame of octagonal shape with 7 m side length, based on carbon fiber-epoxy tubes joined by aluminium knots. The structure is joined at two sides onto the vertexes of two pyramidal towers, in a alt-azimuth mount. This structure is rigid, lightweight (~ 5.5 ton without mirrors), has negligible thermal expansion and an excellent oscillation damping.

The camera is sustained by a metallic arch, stabilized by 10 pairs of 8 mm steel cables tied to the main frame. Following a circular shape, the arch continues also over the back of the dish becoming a rail for the altitude drive and a support for the couterweights. Simulations show that the structure deformation under load is less than 3 mm.

Drive System

Two types of servo-motors (Bosch Rexroth MHD112C-058) move the telescope in the azimuth (**??**) and in the altitude directions (**??**). The allowed movement covers the interval from 100° to -70° in declination and from -90° to 318° (0° corresponds to the North) in azimuth. For the azimuth motion around the fixed central joint (**??**), two 11 kW motors are mounted in opposite positions on two out of the six bogeys connected on the space frame base, resting on the metal circular rail. Fixed chains form a mechanical drive link for the motors, which are engaged by toothed wheels. The third motor, for the elevation motion, is installed on the arch base, a couple of metres out of its lower apex to increase the declination on the side towards the camera access tower. The elevation drive is also equipped with a holding brake, activated in the case the motor power is switched OFF.

During normal operation, the ≈ 65 ton telescope can track a source with a precision of the order of 0.02°. When a GRB alarm arrives, the drive system can reposition the telescope, completing a rotation of 180° in less than 20 s.

Re□ector

The diameter D of the reflector dishes is 17 m as well as its focal distance f, therefore $f/D = 1$. The total surface area is 236 m per telescope. The mirror surfaces have a parabolic shape, so relative arrival times of the photons are conserved on the camera plane. This is important because the conservation of the time spread of the Cherenkov photons allows to reduce the trigger window, which means to reducing the contamination of the night sky background photons. Timing parameters are also useful in the analysis since they give information about impact parameters (distance from the shower axis to the telescope) leading to better image cleaning, angular resolution and energy estimation.

On the other hand, a parabolic reflector makes a relatively large coma aberration, which makes the images extended (blurred) if looking off-axis. In the case of the

MAGIC reflector, the coma aberration effect amounts to 7%, i.e., the virtual distance an image point which should have a distance d is instead $1.07d$.

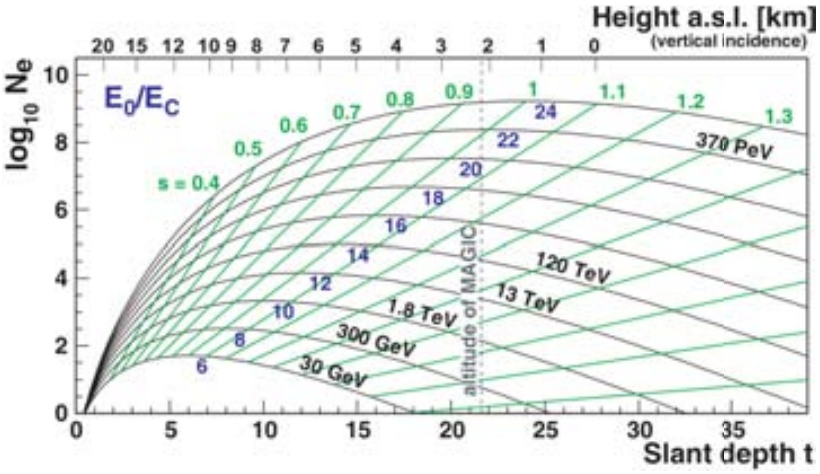

(a) The longitudinal development of an extensive electromagnetic air shower for several different primary gamma ray energies (shown in black, from equation 3.5). The x-axis is the atmospheric slant depth expressed as the number of radiation lengths t (its equivalent in height for vertical incident is shown in the upper axis). The y-axis gives the logarithm of the number of electromagnetic particles in the air shower N_e. Green lines display the shower age s.

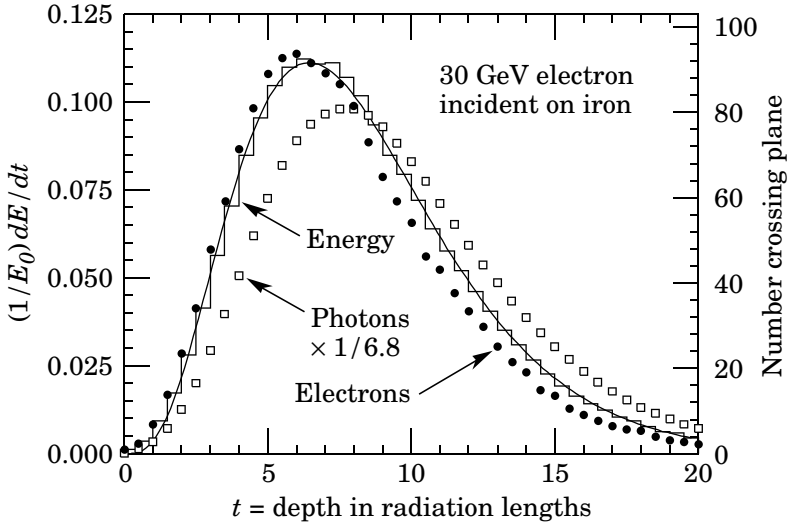

(b) Monte Carlo simulation of a 30 GeV electron-induced cascade in iron, from Nakamura et al. (2010). The histogram shows fractional energy deposition per radiation length t, and the curve is a gamma-function fit to the distribution, as eq. (3.8). Circles and squares indicate the number of electrons and photons with $E > 1.5$ MeV at the corresponding depth. Photon number is scaled by a factor 1/6.8. The value of $t_{\max}$ predicted from eq. (3.9) is 6.7 and 7.7, for electrons and photons, respectively.

Figure 3.5
Development of the multiplicity of an electromagnetic shower in terms of radiation length, in air (3.5a, model) and in iron (3.5b, Monte Carlo simulation).

4. Detection of the Blazar B3 2247+381

The object B3 2247+381 was first detected at the position R.A.: 22.834 72° Dec.: 38.410 28° as a faint flat spectrum radio source with a flux of 0.12 ± 0.02Jy in the third Bologna sky survey at 405 MHz, and reported in the corresponding catalog (Ficarra et al., 1985). Other radio observations at higher frequencies followed (Griffith et al., 1990; Becker et al., 1991; Gregory and Condon, 1991). B3 2247+381 was detected as a bright X-ray source by the ROSAT satellite as early as 1990, it also appears in the ROSAT bright source catalogue with a flux of 0.6 Jy at 1 keV.

The X-ray observations triggered further radio infrared, and optical observations (Neumann et al., 1994; Laurent-Muehleisen et al., 1997; Brinkmann et al., 1997; Falco et al., 1998; Nilsson et al., 2003; Chen et al., 2005; Wu et al., 2007). In 1998 its redshift was measured to be $z = 0.1187 \pm 0.0003$ by observations of optical absorption features, specifically the Ca II H, Ca II K, Hβ, Mg, CaFe, Na lines and in the G bands (Falco et al., 1998).

(Donato et al., 2001) classify it as a high-energy peaked BL Lac object (HBL), while in the sample of BL Lac objects by Nieppola et al. (2006) it is listed as an intermediate-energy peaked BL Lac object (IBL), with the position of the synchrotron peak estimated to be at $_{peak} \approx 4 \times 10^{15}$ Hz. The comprehensive catalogue of quasars and active galaxies of V"ron-Cetty and V"ron (2010) still lists it as a "probable BL Lac object".

A source spatially associated with B3 2247+381 was detected in high-energy γ-rays by the Fermi-LAT telescope after only one year of operations, and is listed both in the first (Abdo et al., 2010) and the second Fermi-LAT catalog of Active Galactic Nuclei (Ackermann et al., 2011). B3 2247+381 was also included in the list of potentially interesting TeV sources released to the Imaging Atmospheric Cherenkov Telescope experiments by the Fermi-LAT collaboration (Thompson, 2009). Its spectrum measured by Fermi-LAT is indeed very hard: its spectral index is reported to be -1.6 ± 0.1 in the first Fermi-LAT source catalog (1FGL, Abdo et al., 2010), and -1.84 ± 0.11 in the second Fermi-LAT source catalog (2FGL, Nolan et al., 2012). Neronov et al. (2011) found a hint at 2.73σ of γ-ray emission above 100 GeV from B3 2247+381 , using Fermi-LAT data between August 2008 and April 2010.

Due to its nature, B3 2247+381 was selected as a promising VHE source for observation by MAGIC in 2006, and it was indeed observed in single-telescope (mono) mode for a total of 16.3 hours (8.3 hours after quality selection) between August and September 2006, resulting in an upper limit on its flux above 140 GeV: $F(> 140\,\mathrm{GeV}) < 1.6 \times 10^{-7}\,\mathrm{m\,s^{-1}}$ (Aleksi et al., 2011a). After this first MAGIC observation, monitoring of this source in the R-band was set up as part of the Tuorla blazar monitoring program using the 35 cm KVA telescope (see Aleksi et al., 2011b, for a description of the telescope). In late September 2010, due to a increased optical flux, MAGIC observed B3 2247+381 again, which resulted in the detection of VHE γ-ray emission on October 7th, 2010 (Mariotti and Collaboration, 2010).

4.1 Motivation for the observation

At the beginning of 2010, 23 High-frequency peaked BL Lac objects (HBLs) had been detected by Cherenkov telescopes in the VHE gamma-ray energy range, making them are the most numerous class of AGNs known. However many more objects in this class had been observed by IACTs in the past, and had not been detected.

Considering the upper limits set from past observations, the data in the GeV energy range coming from the Large Area Telescope on board the Fermi observatory and the new MAGIC stereo sensitivity, B3 2247+381 was proposed for re-observation for the 2010-2011 MAGIC cycle of observations, with the goal of detecting it and possibly determining its spectrum.

B3 2247+381 was one of the two sources shortlisted amongst a list of 56 sources that had been already observed by either MAGIC or VERITAS but not detected. The list was a merge of three distinct publications, here summarized using the names of the corresponding authors:

- The “Mayer” catalog, from Albert et al. (2008b);
- The “HHhne” catalog, from Aleksi et al. (2011a);
- The “Benbow” catalog, from Benbow (2009).

The three catalogs reported observation time, the energy threshold and of course the integral upper limit on the flux above that threshold. The full source list can be found in appendix as table A.4; the catalogs overlapped as shown in Fig. A.2

The selection procedure consisted in two main steps: a check on the existing upper limits from IACTs and an estimation of its maximum flux in VHE gamma-rays extrapolating Fermi-LAT data. Being based on archival data only, it could not take fully into account the variable nature of the sources.

A preliminary skimming of the 56 source candidates removed the ones that had already been detected in the meanwhile, since the goal of the proposal was detecting a new blazar. Also, those not visible from the MAGIC location at a zenith angle

lower than 35 degrees were discarded. The sources not present on the first Fermi-LAT source catalog (Abdo et al., 2010) were also removed, since the high-energy γ-ray spectral information provided by Fermi-LAT was necessary to proceed further into the selection process, and sources not detected by Fermi-LAT after one year of operations were assumed to be too faint for a detection by MAGIC anyway.

The first step in the selection, was eliminating those sources for which the reported upper limit was lower than the projected integral sensitivity for a 25 hours long stereo observation with MAGIC as illustrated in Fig. A.1. In order to perform this selection, a preliminary MAGIC sensitivity curve was used, as the final one was released only in 2011 (Aleksi et al., 2012). The second step of the selection consisted in extrapolating the Fermi-LAT spectrum found in the catalog to VHE energies, taking into account the redshift of the source and the relative attenuation due to the extragalactic background light (EBL), using the Gilmore et al. (2009) absorption model. All sources were (optimistically) assumed to have an intrinsic spectrum power-law index extending into VHE energies. A final check on the "source variability" parameter given in the 1FGL was also performed, to assure the stability of the source at least at GeV energies. Sources whose probability of being variable was greater than 99% (corresponding to a "source variability" index of 23.21) were excluded.

Two sources were shortlisted at the end of this process, both HBLs: 1ES 2321+419 and B3 2247+381 . The time allocated for the observation of both was 20 hours.

1ES 2321+419 was observed in August 2010, but the observation did not result in a detection. About 10 hours of data were taken, however most of them were affected by strong *calima*, an aerosol layer of dust particles from the Sahara desert in the lower atmosphere that strongly affects the performance of the telescope by increasing the threshold and compromising the energy reconstruction (Terrats, 2011). Due to the absence of a signal the observations were stopped. A full analysis of this observation and other non-detections of AGNs will be presented in a forthcoming paper.

Observations of B3 2247+381 were in contrast triggered by an optical high state. The trigger of opportunity was set up because correlation between flares in optical and VHE γ-rays has been observed in several blazars (Reinthal et al., 2012). In late summer 2010, the optical monitoring by the Tuorla group (Berdyugin et al., 2012) showed a 30% increase in the R-band flux of B3 2247+381 , going from its usual steady value of ~ 1.8 mJy (measured from 2006 until 2009) to an average level of 2.4 mJy. In late September 2010 an alert was issued to the MAGIC telescopes, which started observing on September 30th.

4.2 MAGIC observations

B3 2247+381 was observed with the MAGIC telescopes during 13 nights between September 30th and October 13th 2010, for a total of 21.2 hours, partly under moderate moonlight conditions. A preliminary quality selection was performed on the data as can be seen in Fig. 4.1 per telescope and per sub-run, with empirical quality

cuts on four parameters: "cloudiness", event rate, and root mean square (RMS) of the "width" and "length" Hillas parameters, as suggested by Ignasi (2009). The last three parameters were calculated after cleaning and after a cut in the "size" parameter above 100 photoelectrons, taking into account their dependence on the zenith angle θ_{zd}. A further selection cut was $\theta_{zd} < 35$ deg.
As a result of the quality selection, two full days were discarded, and a few other subruns, for a total of 5.3 hours, The observation periods left after this quality selection are listed in table 4.0a.

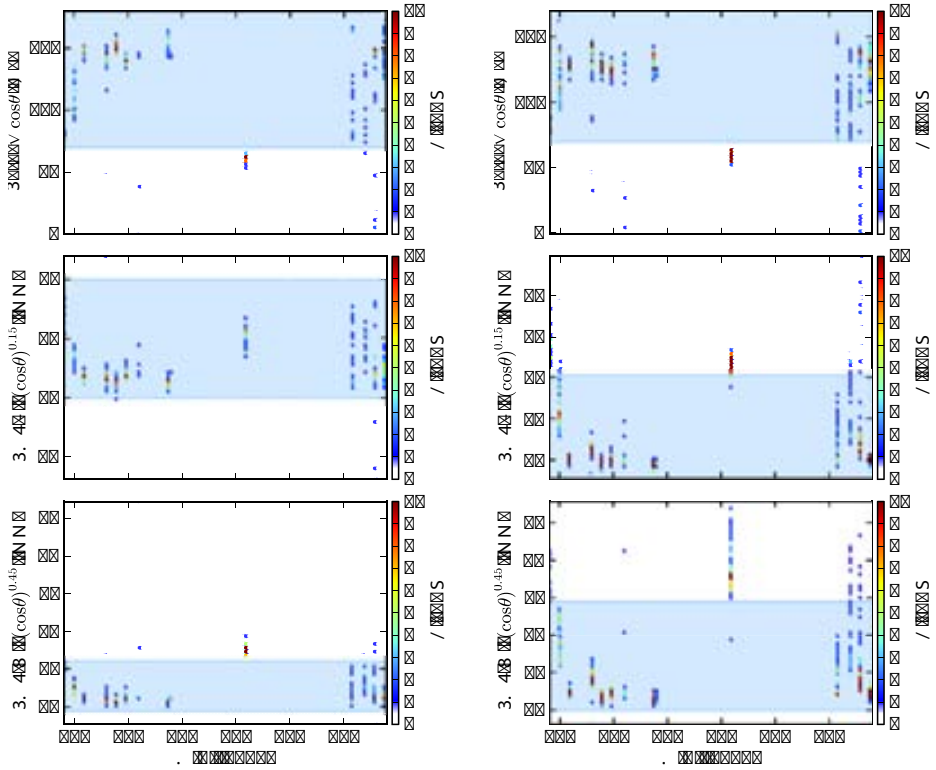

Figure 4.1
Quality cuts for MAGIC B3 2247+381 observations. Cut parameters are the rate and the RMS of "width" and "length" image parameters. The zenith angle dependence is taken into account as a power of $(\cos\theta_{zd})^{\alpha}$, with $0.25 < \alpha < 0.5$, determined empirically

(a) Quality cuts on M1 (b) Quality cuts on M2

The data was taken in false-source tracking mode as explained in chapter 3: the telescope was alternated every 20 minutes between two sky positions at 0.4° offset from the position of B3 2247+381 , one towards the north and the other towards the south.

Only "stereo" events, i.e. events that triggered both telescopes, were recorded. The multiplicity of the level 1 (L1) triggers was set to 3NN, and the average rate of stereo triggers was slightly about 240 Hz. The data was analyzed using the standard MAGIC

Table 4.1: B3 2247+381 observations and quality selection

(a) Summary of the observations

Day	Sub-runs		Eff. time (h)	Runs	N. events
	M1	M2			
2010/09/30	19/19	0/47	0.0	⊠	⊠
2010/10/01	45/46	111/119	1.51	6	443451
2010/10/02	37/38	92/96	1.12	6	330042
2010/10/04	58/59	141/149	1.71	7	497450
2010/10/05	64/69	163/171	1.76	7	487288
2010/10/06	51/53	120/125	1.46	7	421492
2010/10/07	9/11	23/27	0.30	1	87092
2010/10/10	49/54	135/139	1.50	6	434874
2010/10/17	0/62	0/152	0.0	⊠	⊠
2010/10/27	29/31	76/77	1.17	5	326245
2010/10/28	26/27	44/73	0.67	4	204154
2010/10/29	41/50	105/127	1.34	6	408339
2010/10/30	78/79	140/145	1.71	7	491333

(b) Data quality parameters after selection. Rate, RMS of width and length are calculated for events above 100 photoelectrons in both telescopes.

Day	θ_{zd} (deg)	Rate (Hz)		RMS width (mm)		RMS length (mm)	
		M1	M2	M1	M2	M1	M2
2010/10/01	14.8 ⊠ 34.1	49.9	59.0	22.0	27.7	43.9	53.3
2010/10/02	10.5 ⊠ 24.0	49.9	52.5	22.5	23.9	44.3	48.0
2010/10/04	13.2 ⊠ 34.1	46.6	51.9	21.9	24.9	43.8	48.5
2010/10/05	10.9 ⊠ 32.2	42.4	43.2	21.9	23.2	43.8	47.3
2010/10/06	9.8 ⊠ 15.0	46.6	49.9	22.6	24.4	44.8	48.7
2010/10/07	13.0 ⊠ 13.0	50.3	53.1	22.6	23.9	44.9	48.2
2010/10/10	10.5 ⊠ 26.0	46.0	46.9	22.1	23.2	44.2	47.4
2010/10/27	9.8 ⊠ 24.8	51.3	54.5	23.5	25.7	44.9	49.8
2010/10/28	12.9 ⊠ 22.6	52.9	61.4	22.5	28.0	44.3	53.8
2010/10/29	12.5 ⊠ 26.3	52.5	56.1	22.0	24.8	44.0	50.3
2010/10/30	11.9 ⊠ 32.1	48.0	50.3	22.1	23.3	44.3	48.3

analysis framework "MARS" as described in Moralejo et al. (2009), with additional adaptations incorporating the stereoscopic observations. The images were cleaned with the “absolute” method using timing information as described in (see Aliu et al., 2009). Since the observations were taken in average conditions, with no or moderate moonlight, default cleaning levels were chosen. In MAGIC-I the absolute cleaning levels were of 6 photoelectrons (phe), for the so-called “core pixels” and 3 phe for the “boundary pixels”. In MAGIC-II the levels were slightly higher, at 9 phe and 4.5 phe respectively. For the timing parameters the default setting had also been kept at 4.5 ns for the maximum single pixel core time offset, and 1.5 ns for the maximum time difference between boundary pixel and core neighbor.
Image parametrization followed the prescriptions of Hillas (1985), with additional

parameters described in chapter 3.

The reconstruction of the shower arrival direction was accomplished using a random forest regression method for the determination of the "DISP" parameter as in Aleksi□et al. (2010), which was extended using stereoscopic information such as the height of the shower maximum and the impact distance of the shower on the ground. Estimating the "DISP" parameter for each telescope separately gives two possible degenerate solutions along the major axis of the shower image of each telescope (see Fig. 4.2). The combination of two DISP solutions (one per telescope) that have the shortest squared angular distance □θ^2 between them is chosen. If □$\theta^2 > 0.05$ deg^2 the event is discarded, and this improves hadron rejection, since for hadrons □θ^2 is in general larger.
The arrival direction is finally found by averaging the two DISPs, weighted with the number of pixels present in the corresponding shower images.

For the gamma-hadron separation the random forest method is used (Albert et al., 2008a). In the stereoscopic analysis image parameters of both telescopes are used as well as the shower impact point and the shower height maximum.

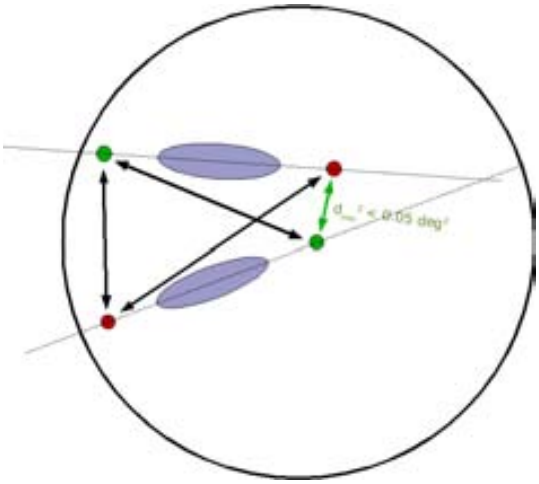

Figure 4.2
Stereo source position reconstruction using DISP for each telescope: the degeneracy is removed by choosing the closest possible combination.

4.3 Multi-wavelength observations

Optical observations and data analysis

B3 2247+381 has been observed in the Landoldt R-band (0.64□m) by the by the Tuorla group (Berdyugin et al., 2012) as previously mentioned. The observations were carried on using a CCD camera attached to the 35 cm KVA telescope, and the brightness of B3 2247+381 was calibrated using known stars in the same CCD frame. The R-band magnitude was converted to flux using: $F = 3080 \times 10^{-m_R/2.5}$ Jy. The host galaxy contribution has been subtracted from the data, following Nilsson et al. (2007). The fluxes were corrected for galactic absorption by $R = 0.398$ mag (a more

recent value given in Schlafly and Finkbeiner, 2011, is $R = 0.323$ mag, but was not available at the time of the analysis.)

X-ray observations and data analysis

X-ray observations of B3 2247+381 were also requested at the same time as the ones by MAGIC, using the Target of Opportunity (ToO) program of the *Swift* satellite. The *Swift* Gamma-Ray Burst observatory (Gehrels et al., 2004) is an X-ray satellite whose principal mission is to detect and follow up GRBs, however due to its fast response capability and its multi-wavelength coverage it turned in a multi-purpose observatory. Its three instruments cover three different wavelength bands: UVOT (Ultra-Violet/Optical Telescope, Roming et al., 2005) covers wavelengths between 1800 and 6000 Å, XRT (X-ray telescope, Burrows et al., 2005) covers the soft X-ray band between 0.3 and 10 keV, and BAT (Burst Alert Telescope Barthelmy et al., 2005) covers the hard X-ray band between 15 and 150 keV.

After the ToO was issued, the XRT instrument aboard *Swift* observed B3 2247+381 between October 5th, to 16th, 2010, for ~ 5 ks every night, in photon counting mode. *Swift* archival data was also analyzed in order to compare the level of X-ray emission previous to the ToO. Relevant X-ray B3 2247+381 data was taken on August 10th, 2009; February 18th, 2010 and April 18th, 2010. During the time interval of the MAGIC observations the X-ray flux measured by *Swift* was found to be ~ 4 times higher than in the previous observations by the satellite.

Swift/XRT data was processed with the standard HEASoft software package v6.10 distributed by HEASARC[1] (NASA, 2012b). Events graded 0–12 were selected from the photon count data (see Burrows et al., 2005) and the standard telescope response matrices[2] were employed. The spectral analysis was performed extracting "on" events from a circle with a radius of 20 pixels (~ 47″) around the source position, and background events from a circular region with a radius of 40 pixels centered on an "off" source. The excesses were binned in energy ensuring a minimum of 30 counts per bin, in order to realiably use the χ^2 statistics. The spectral fitting program XSPEC v.6.12 , was used for performing the Spectral analyses. Both a simple power-law and a log-parabolic model (as in Massaro et al., 2004) were tried, assuming the absorption hydrogen-equivalent column density fixed to the Galactic value in the direction of the source (1.2×10^{-17} m). The results provided by the two models agree in terms of goodness of fit above ~ 0.7 keV. Below this energy the differences are negligible due to low statistics.

Swift/UVOT data was also available , however during the time interval of the MAGIC observations the source was observed with different filters, since the telescope was set to "filter of the day" mode. This did not allow to compare directly UV fluxes among different days, nor to extract a reliable magnitude estimation.

[1] In specific the FTOOLS task XRTPIPELINE 0.12.6 was used

[2] Version v.20100802 of the default *Swift* CALDB database

Fermi observations and data analysis

For most of the time the Fermi-LAT pair conversion telescope (covering the enegy band from 20 MeV to 300 GeV, see Atwood et al., 2009a) operates in survey mode, scanning the time every three hours. This means that B3 2247+381 got observed since the very beginning of the mission, on August 5th, 2008. The data used for this study spans a little over 32 months, until April 7th, 2011.

Data analysis was performed using the Fermi Science Tool software package v9r23p0, available from the Fermi Science Support Center (FSSC, NASA, 2012a) , and "Pass 6" data. Preliminary cuts selected only events in the "diffuse" event class (i.e. those with the highest probability of being photons), coming from a circular region of 12° radius centered on B3 2247+381 , to be used in the analysis. A further cut on the maximum zenith angle ($\theta_{zd} < 100°$) was applied in order to reduce contamination of albedo γ-rays coming from the earth limb, produced by interactions of cosmic rays with the upper atmosphere. The galactic γ-ray background was modelled using the spatial and spectral template , while the extra-galactic and instrumental isotropic backgrounds were modelled with . The two files are available on the FSSC websiteí.

The spectral fitting itself was performed applying an unbinned maximum likelihood technique (Mattox et al., 1996), to events between 300 MeV and 300 GeV. The model, apart from the above-mentioned background components, includes all sources present in the second source catalog 2FGL located within 7° from B3 2247+381 . The normalization parameters of source and background components were allowed to vary freely during the spectral point fitting iterations, while the other parameters were set to those of the 2FGL catalog. The instrument response function (IRF) used was the post-launch one . The systematic uncertainty in the flux is estimated as 10% at 100 MeV, 5% at 560 MeV and 20% at 10 GeV and above[4].

During the time interval of the MAGIC observations (taken as 30 days between September 30th and October 30th 2010), B3 2247+381 could not be significantly resolved in the Fermi-LAT data. Upper limits were calculated for a 2-sigma (95%) confidence level using the Bayesian method (Helene, 1983).

4.4 Excess determination and position reconstruction

The signal is extracted from the distribution of the square of the angle θ between the reconstructed direction of the events and the position of B3 2247+381 . Prior to the signal extraction and excess determination, cuts on both θ^2 and the "Hadronness" parameter were optimized on a trial sample of Crab Nebula data with similar characteristics, assuming the source flux to be 3% that of the Crab Nebula. The result of this optimization was $\theta^2 < 0.013 \text{degrees}^2$ and "hadronness" < 0.26. Other standard cuts were applied on the "size" parameter (above 55 photoelectrons in both

íhttp://fermi.gsfc.nasa.gov/ssc/data/access/lat/BackgroundModels.html

[4]http://fermi.gsfc.nasa.gov/ssc/data/analysis/LAT_caveats.html

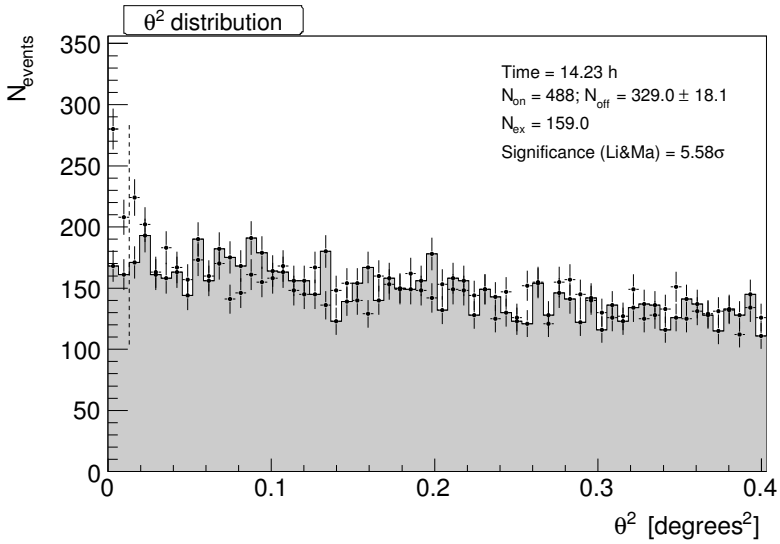

Figure 4.3
Distribution of the squared angular distance θ^2 between reconstructed direction and position of B3 2247+381 (black points with error bars). The gray histogram is the normalized θ^2 distribution for the anti-source.

telescopes) and on the estimated energy (above 150 GeV), enhance the sensitivity at intermediate energies.

The events surviving the above cuts were used as "on" sample. The background ("off") sample comes from the same data and cuts, but with θ calculated as the angle between the reconstructed direction of the event and the "anti-source" position, located 180° from the real source position in the plane of the camera. The estimated energy threshold of this data is 200 GeV, calculated from MC simulated data by finding the peak of the differential rate vs. energy distribution after cuts and spectral reweighting, as described in (Konopelko et al., 1999).

As can be seen in Fig. 4.3, the number of "on" events N_{on} is 488, while that of the "off" $N_{o⊠}$ events is 329, with an excess N_{exc} of 159 ± 28 events, corresponding to a significance of 5.6 σ calculated using equation (17) from Li and Ma (1983).

The source position and extension were determined fitting a 2D Gaussian on the excess sky map produced with the above-mentioned cuts, as can be seen in Fig. 4.4. The position of the γ-ray excess is R.A.: 22.8340 ± 0.0011 degrees, Dec.: 38.4221 ± 0.0171 degrees, within 0.015° from B3 2247+381 . The extension is 0.1 ± 0.01 degrees. The point spread function of MAGIC at these energies is 0.1°, which means that the above values are fully consistent with a point-like source placed at the position of B3 2247+381 .

4.5 Spectrum and Lightcurve

The integral flux of the source was determined to be $(5.0{\pm}0.6_{\mathrm{stat}}{\pm}1.1_{\mathrm{sys}}){\times}10^{8}$ ph m s^{-1} after a cut above 200 GeV. The effective area from MC simulations as can be seen in Fig. 4.5a. Above 200 GeV it was calculated to be $4.68 \pm 0.16 \times 10^4$ m. To extract the differential energy spectrum, the data was binned in 24 logarithmically-spaced

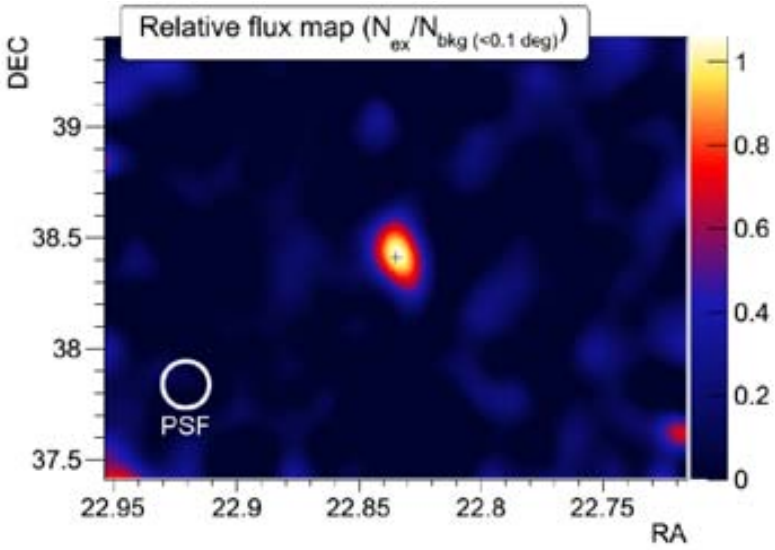

Figure 4.4
Skymap of the point-source equivalent integrated excess N_{ex} relative to the background density $N_{bkg(<0.1°)}$, calculated as number of background events within a circle of radius 0.1°. The black cross shows the position of B3 2247+381 as found in Ficarra et al. (1985). The white circle shows the total PSF after smearing. Smearing radius was chosen to be equal to the point spread function 0.076 ± 0.01 degrees, found using Crab Nebula data.

bins between 5 GeV and 50 TeV in estimated energy, and energy-dependent θ^2 and "hadronness" cuts were obtained from Crab Nebula data as explained before. The efficiency of these cuts varies from 45% at 200 GeV to 65% at 1 TeV, as can be seen in Fig. 4.5b. Excesses were calculated separately for individual bins using θ^2 plots; in all of them the background was normalized to the same value, 0.995 ± 0.0094. In order to correct for the effects introduced in the spectrum determination by the limited energy resolution, different unfolding algorithms were used (Forward, Tikhonov, Schmelling, and Bertero, all described in Albert et al. (2007)). All of the bins with non-null effective area (i.e. those with energies between were used for the unfolding.

Figure 4.5
MAGIC Effective area and efficiency of the cuts as a function of energy, calculated from Monte Carlo simulated data

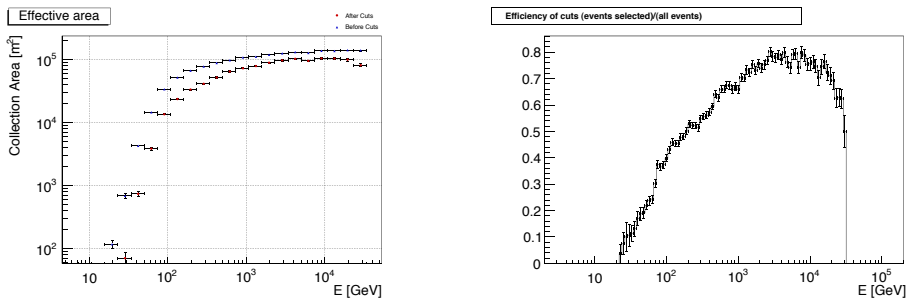

(a) Effective area.

(b) Efficiency of the cuts.

The differential energy spectrum can be seen as black points in Fig. 4.6. It is well described by a simple power-law:

$$\frac{dN}{dE} = f_0 \left(\frac{E}{300\,\text{GeV}} \right)^{\alpha} \tag{4.1}$$

where $\alpha = (-3.2 \pm 0.5_{\text{stat}} \pm 0.5_{\text{sys}})$ is the spectral index and $f_0 = (1.4 \pm 0.3_{\text{stat}} \pm 0.2_{\text{sys}}) \times 10^{-7}$ ph m s^{-1} the flux normalization at 300 GeV .

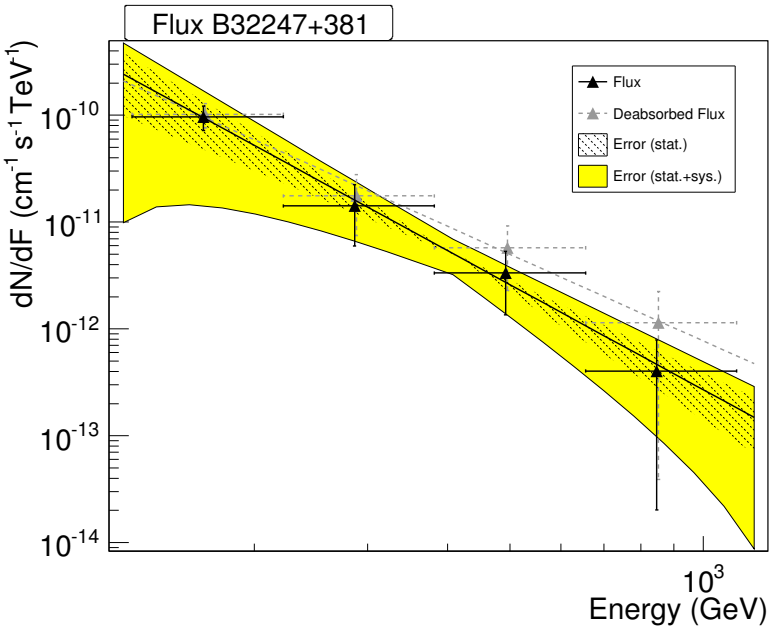

Figure 4.☒
The unfolded differential energy spectrum of B3 2247+381 observed by MAGIC. The black data points refer to the measured spectrum, while the grey dashed points have been corrected for the attenuation of the EBL (see main text). The dashed band corresponds to the statistical error of the fit, while the yellow one is the sum of statistical and systematic errors.

Since the redshift of B3 2247+381 is known, it is possible to obtain the intrinsic source spectrum by correcting the observed one for absorption due to extragalactic background light (EBL) , a procedure known as de-absorption (see §2.2.6 for more details). Two different models for the absorbed spectra were employed: a forward evolution lower limit model by Kneiske and Dole (2010) and a observed evolution model by Dom¯nguez et al. (2011). The latter predicts higher attenuations than the former : at 600 GeV the difference is 10%, and at 1 TeV it is 20%, as can be seen in Fig. 4.7, where the attenuation values derived from these models for the redshift of B3 2247+381 are displayed. . Using the full EBL model by Dom¯nguez et al. (2011), the intrinsic spectrum is found to have spectral index $\alpha = (-2.7 \pm 0.5_{\text{stat}} \pm 0.5_{\text{sys}})$ and flux normalization at 300 GeV $f_0 = (2.0 \pm 0.3_{\text{stat}} \pm 0.3_{\text{sys}}) \times 10^{-7}$ ph m s^{-1}. The results obtained with the other model by Kneiske and Dole (2010) are comparable within statistical uncertainties.

The MAGIC daily light curve of B3 2247+381 above 200 GeV is show in Fig. 4.8a. It is consistent with a non-variable emission, having a reduced ☒^{2} value of 0.6 with 10 degrees of freedom. It is also not possible to conclude that B3 2247+381 was in a higher emission state during the October 2010 MAGIC observations and no long-term variability can be established in VHE γ-rays: the flux values are also compatible with the upper limit coming from the previous MAGIC observations in 2006.

Long-term light curves of B3 2247+381 in HE γ-rays (from Fermi-LAT), X-rays (*Swi*☒/XRT) and optical (KVA telescope, R-band) are shown in Fig. 4.8a, together with the MAGIC one.

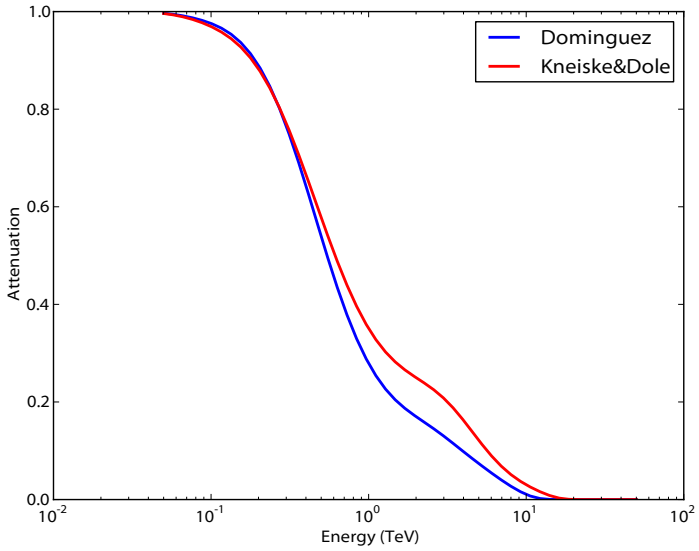

Figure 4.7
EBL attenuation models from Kneiske and Dole (2010) and Dom¯nguez et al. (2011) for redshift $z = 0.1187$, plotted as a function of the γ-ray energy,

The Fermi-LAT bimonthly binned light curve is also consistent with steady emission. A fit on the flux points where the source was detected gives a value of $3.7 \pm 0.5 \times 10^{-5}$ ph m s^{-1}, with a reduced χ^2 value of 0.7 and ten degrees of freedom. The conclusion is that Fermi-LAT is not sensitive enough to detect short term variations at this flux level. On the contrary, emission from B3 2247+381 in X-rays and optical band shows a clear increase of the flux level starting in the fall of 2010. However, when one considers daily timescales during September–October 2012 (see Fig. 4.8b), no strong variability is detected, with the exception of one night when the X-ray flux was significantly higher (almost a factor of 2) than the other data points, but simultaneous optical or MAGIC data was not available.

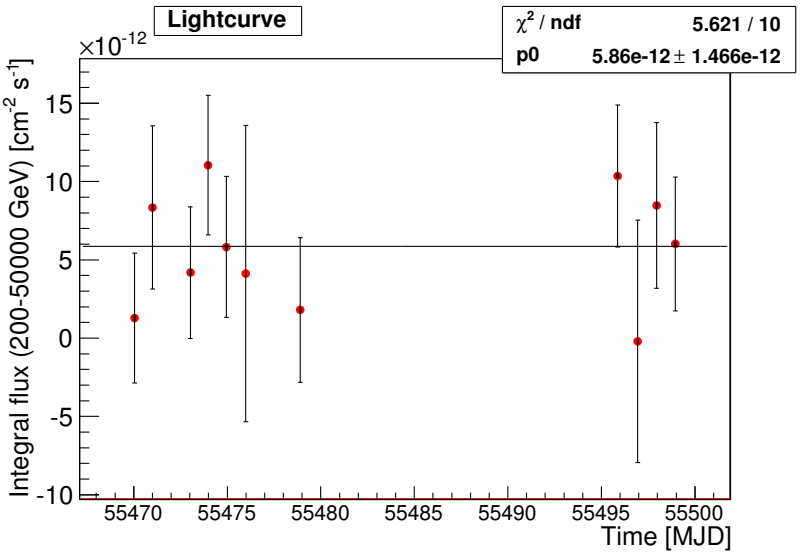

(a) MAGIC VHE γ-ray lightcurve above 200 GeV.

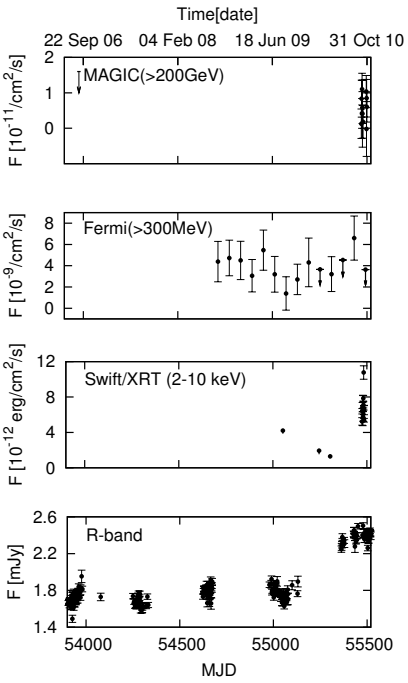

(a) Multi-wavelength long-term lightcurves.

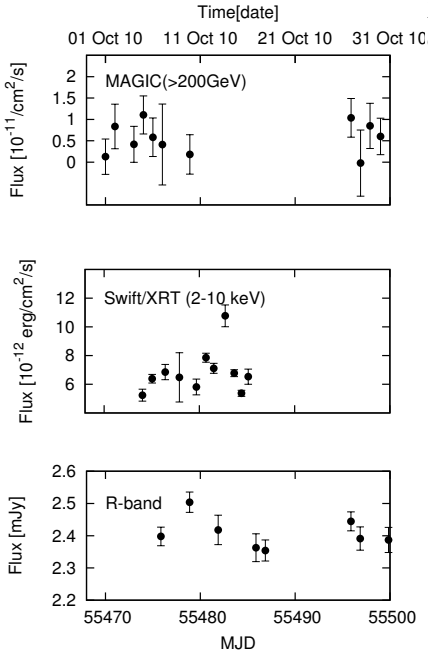

(b) Multi-wavelength lightcurves during the magic observations in October 2010.

Figure 4.8 Multi-wavelength light curves of B3 2247+381 .

4.6 Modelling and Discussion

As stated in the previous section, it is not possible to conclude that B3 2247+381 was in a high VHE γ-ray emission state from the MAGIC observations alone. It is however clear that the source was in a high emission state in X-rays and optical R-band. To model the spectral energy distribution of B3 2247+381 in both its high and low state two instances of a simple one-zone synchrotron-self-Compton (SSC) model from Tavecchio et al. (2001) were produced, varying its parameters. In this model, the emission region is assumed to be spherical with radius R, filled with a tangled magnetic field of intensity B. Relativistic electrons giving rise to SSC emission follow a smoothed a power-law energy distribution specified by the limits $\gamma_{\rm min}$ and $\gamma_{\rm max}$i, the break $\gamma_{\rm b}$ as well as the slopes n_1 and n_2 before and after the break, respectively. Their number density normalization is ρ, and relativistic beaming effects are taken into account by the Doppler factor . The values of these parameters used for the modelling of both high and low state are shown in table 4.2.

Fig. 4.9 shows the spectral energy distributions (SED) obtained from them, together with multi-wavelength data for both states. Differences between the two realizations of the model can be easily seen in this figure: the synchrotron component of the emission is significantly higher in the high state, while the inverse Compton component undergoes only minor changes. The parameters influencing the synchrotron and inverse Compton luminosity ratio are mainly the electron normalization K, the source radius R and the Doppler factor . The steeper spectral index of X-ray emission in the low state requires a larger value of n_2. The values adopted for the parameters, and resumed in table 4.2 are close to the typical ones derived for BL Lac objects (see Tavecchio et al., 2010). The Doppler factor is larger and magnetic field intensity lower than their "standard" values because of the relatively large separation between the synchrotron and the inverse Compton peaks observed in B3 2247+381 .

The high state of B3 2247+381 was additionally modelled using a different, two-zone SSC model, similar to that used in Weidinger et al. (2010), see Fig. 4.10. The parameters of this self-consistent model are basic physical quantities. The ones describing the source and its environment (R and B) are in common with Tavecchio et al. (2001), but the electron (and photon) spectral index s, the break and maximum energies $\gamma_{\rm b}$ and $\gamma_{\rm max}$ are derived from the steady state solution assuming a continuous injection of monochromatic electrons at Lorentz factor γ_0 with a rate K, and an acceleration efficiency $t_{\rm acc}/t_{\rm esc}$. The values for these parameters have been summarized in table 4.3. The common values between the two models agree well.

Table 4.2: Input parameters for the high and low states of the SSC-model of Tavecchio et al. (2001) shown as solid and dashed lines in Fig. 4.9. Explanations are given in the text.

Flux State	$\gamma_{\rm min}$	$\gamma_{\rm b}$	$\gamma_{\rm max}$	n_1	n_2	B G	ρ cm^{-3}	☒	R cm
High	3×10^3	7.1×10^4	6×10^5	2.0	4.35	0.06	2.5×10^3	35	8×10^{15}
Low	3×10^3	6.8×10^4	5×10^5	2.0	5.35	0.08	1.15×10^4	30	4×10^{15}

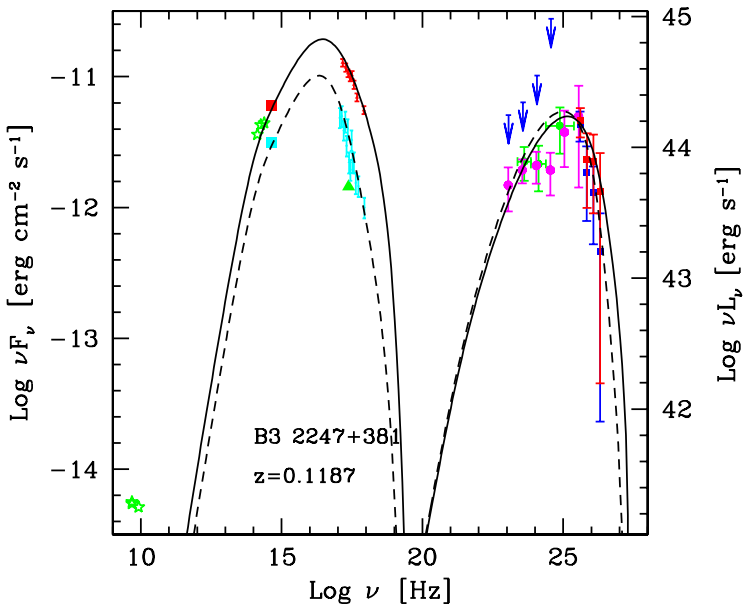

Figure 4.9: Spectral energy distribution of B3 2247+381 (red: EBL corrected MAGIC spectral points). The green crosses are Fermi-LAT 1FGL data points (Abdo et al., 2010). while the magenta points represent the analysis from this work (2.5 years of data). Blue arrows show the 95% confidence upper limits computed from Fermi-LAT data for the time interval of the MAGIC observation. Low (high) state *Swi* data were taken on April 18th 2010 (October 5-16, 2010). Green and light blue points represent non-simultaneous low state data. KVA R-band data is plotted as red and light blue squares, for high and low state respectively. The solid line is our SSC-model fit to the high state observations; the dotted line is a fit to the low state observations.

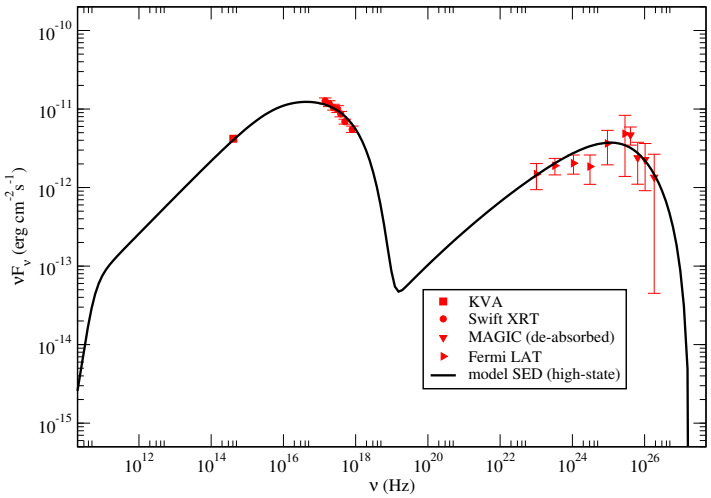

Figure 4.10
Spectral energy distribution of the high state of B3 2247+381 , with the model from Weidinger et al. (2010) (solid black line). The data points are described in the inlay of the figure. The fit parameters can be found in Table 4.3.

Table 4.3: Input parameters for the Weidinger et al. (2010) model of the high state of B3 2247+381 displayed in Fig. 4.10. Explanations are given in the text.

Input parameters					Derived quantities		
γ_0	K	B	t_{acc}/t_{esc}	R	s	γ_b	γ_{max}
	$cm^{-3}\,s^{-1}$	G		cm			
10^4	8.4×10^4	0.07	1.09	1.3×10^{16}	2.09	2.9×10^4	4.8×10^5

5. Observations of the Crab Pulsar with MAGIC

The Crab pulsar (also known as PSR B0531+21) is a young neutron star, remnant of SN 1054, one of the eight historical supernovas, observed by Chinese astronomers in 1054 CE . Its age is therefore 959 years, and its estimated distance is 1.9 kpc. A short summary of other relevant proprieties is given in table 5.1.

The pulsar is surrounded by a filled-center supernova remnant (as defined by Green, 2004), or plerion (as defined by Weiler and Panagia, 1980), commonly known as the Crab nebula (Mitton, 1979). It is the second SNR by surface brightness (4.4×10^{18} W m Hz^{-1} sr^{-1}) surpassed only by Cassiopeia A SNR. Most of the radiation it emits is of non-thermal nature, and there is little doubt that the highly relativistic electrons responsible for it are injected in the nebula by the pulsar, however the details of the injection process are still poorly known.

After the discovery of the pulsar, the Crab system as a whole was established as the prototypical young pulsar - pulsar wind nebula complex, but also one of the most prominent sources of non-thermal radiation across the electromagnetic spectrum. Theoretical models can satisfactorily explain most of the observed features.

The Crab nebula was the very first VHE γ-ray source discovered by an atmospheric imaging Cherenkov telescope (Weekes et al., 1989), and has been subject of detailed studies by all by the following generations of Cherenkov telescopes ever since. Due to its brightness in the VHE band and the steadiness of its emission, the Crab nebula became the de-facto "standard candle" of VHE γ-ray astronomy.

Conversely, the Crab pulsar was detected in HE as early as 1971, but it it eluded detection in the VHE γ-ray band for decades. In addition, theoretical models explaining the HE and VHE emission remain subject of disputes.

The observations of the Crab pulsar with the MAGIC telescopes presented in this thesis provide for a better insight in the physical processes taking place in and around it, and at the time of its publication reserved some surprises to the high-energy astrophysics community.

Table 5.1: Crab pulsar proprieties

Crab pulsar proprieties	
Name :	J0534+2200
Alt. Name :	B0531+21
RA :	05h 34' 32.237"
DEC :	22° 01' 22.56"
Gal. Longitude l :	184.551 365 degree
Gal. Latitude b :	−5.778 631 degree
Epoch T_0 (MJD) :	54681
$\boxtimes_0$:	0.0749585628509521
$\boxtimes_0$:	29.7532408163703 Hz
$\boxtimes_0$:	$-3.721918061502 \times 10^{-10}$ Hz/s
$\boxtimes_0$:	$1.111948785137 \times 10^{-20}$ Hz/s^2
$\dot{E}$:	4.37×10^{38} erg/s
B_S :	3.8×10^{12} G

5.1 Previous observations of the Crab Pulsar

The emission from the Crab pulsar spans the whole electromagnetic spectrum, and it is characterized by a two-peaked light curve (shown in Fig. **??**). The positions of the two peaks in phase remains roughly the same, while their relative height and their widths change at different wavelengths. The highest peak in radio is commonly referred to P1 and its location is at phase ~ 0, while the other peak, P2, is located at phase ~ 0.4.

The Crab pulsar is probably one of the best studied pulsars, and the second one to be discovered, thanks to its giant radio pulses (Staelin and Reifenstein, 1968). Shortly after its discovery in radio, a pulsed signal was detected at optical wavelengths (Cocke et al., 1969), then in X-rays (Fritz et al., 1969; Floyd et al., 1969) and in γrays (Browning et al., 1971; Kniffen et al., 1974).

For what regards the very high energy band, many detection attests were made in the past by ground-based atmospheric imaging Cherenkov telescopes (summarized in table 5.2).

It was only in 2008, prior the Fermi-LAT satellite operation, when finally the MAGIC Collaboration reported the detection of a pulsed signal above 25 GeV (Aliu et al., 2008). This detection was achieved after 22 hours of observation with a special trigger (the "sum trigger", Rissi et al. (2009)) that significantly lowered the energy threshold of the then-standalone Cherenkov telescopes.

The MAGIC detection revealed that, if the energy spectrum was modeled as a power law with an exponential cutoff, then the cutoff energy E_c had to be 17.7 ± 2.8 GeV, a much higher value than what had been previously predicted and tentatively measured (only poorly with EGRET, see Fierro et al. (1998) and Kuiper et al. (2001) and

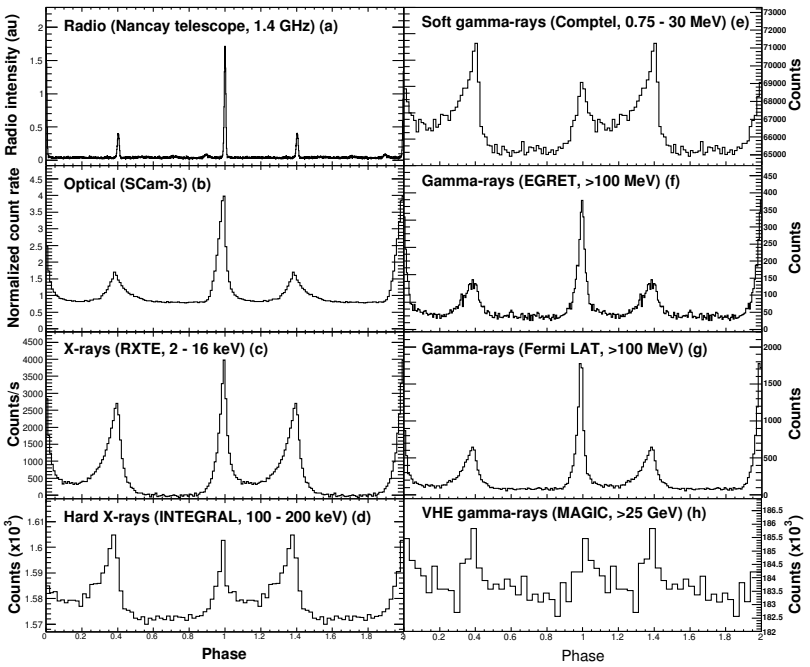

Figure 5.1
Light curves of the Crab Pulsar at different wavelengths (available in 2010). Two cycles are shown. From Abdo et al. (2010) and references therein.

references therein).

The presence of such a mild exponential cutoff, (if one was present at all), suggested that the Crab pulsar has high-altitude emission zones. This implied that the polar cap model was essentially excluded as a possible explanation for the HE γ-ray emission.

Later, Fermi-LAT and AGILE observed the high-energy γ-ray emission (between 100 MeV and few tens of GeV) from the Crab pulsar (Pellizzoni et al., 2009; Abdo et al., 2010) measuring it in detail. In the case of the Fermi-LAT measurements, spectra could be resolved for finer bins in phase than previous works.

The Fermi-LAT observations showed that the energy spectrum of the Crab pulsar could also be best modeled as a power law with an exponential cutoff at around few GeV, as for the other rotation-powered gamma-ray pulsars detected by that instrument (Abdo et al., 2010). Only in few cases the polar cap scenario remained a viable alternative.

The Fermi-LAT team, reported a phase-averaged value for the cutoff energy of E_c = $5.8 \pm 0.5_{\rm stat} \pm 0.6_{\rm sys}$ GeV. Cutoff energies of spectra extracted using finer phase regions (from -0.13 to 0.52) ranged between $1.7 \pm 0.5_{\rm stat} \pm 0.3_{\rm sys}$ and $10.0 \pm 4.8_{\rm stat} \pm 11.6_{\rm sys}$, and pulsed photons could be detected up to ~ 20 GeV.

The value of E_c obtained with Fermi-LAT did not agree with that that obtained with MAGIC one year before. The Fermi-LAT team in (Abdo et al., 2010) attributed this discrepancy to the fact that the value of E_c reported in the MAGIC paper was was obtained using an outdated spectrum in the MeV band: a power-law with spectral index α = 2.022, coming from old EGRET data. Taken that into account, the two

Table 5.2: Crab Pulsar detection attempts in the VHE energy band.

Experiment	Period	Effective Time	Energy Range	Result
WHIPPLE	1994 - 1997	73.4 h	250 GeV - 4 TeV	< 3% Crab UL
HEGRA	1997 - 2002	384.86 h	0.32 - 100 TeV	< 3% Crab UL
MAGIC Mono (L1T)	2005 - 2006	16 h	60 GeV - 10 TeV	< 2% Crab UL
MAGIC Mono (L1T)	2007 - 2009	61 h	60 - 200 GeV	Hints, not fully analyzed yet!
MAGIC Mono (ST)	2007 - 2009	59 h	25 - 100 GeV	First detection above 25 GeV
VERITAS	2007 - 2011	107 h	100 - 400 GeV	Full detection up to 400 GeV
MAGIC Stereo	2009 - 2011	73 h	50 - 400 GeV	Full detection up to 400 GeV

results would be compatible within systematic errors.

Later observations by MAGIC with the same trigger delivered a better measurement between approximately 25 – 100 GeV. The newer MAGIC measurement together with Fermi-LAT data suggested a simple power-law extension of the spectrum up to 100 GeV, with no sign of cutoff (shown in Saito, 2010; Aleksi⊠et al., 2011), in stark disagreement with the published Fermi-LAT results, and more importantly with the presence of a exponential suppression of the spectrum altogether.

The timely measurement of the spectrum of the Crab pulsar by the VERITAS air imaging Cherenkov array (Aliu et al., 2011) added credibility to the power-law extension claimed by MAGIC, and showed that the spectrum continued above 100 GeV, something completely new that strongly excluded the exponential cutoff hypothesis.

Therefore, the Crab pulsar can be considered the only pulsar not showing a spectrum with a cutoff at few GeV, a unique counterexample of an otherwise general property of γ-ray pulsars.

Thus, to develop pulsar emission theories beyond the widely accepted curvature-radiation models, it is essential to examine the detailed phase-resolved spectrum of this young pulsar in the VHE band, a task that could be accomplished during this thesis by observing the pulsar with MAGIC in stereoscopic mode.

5.2 Data sample and quality selection

In the analysis presented here, stereoscopic data from the winter seasons in 2009/2010 and 2010/2011 were used. During that time, the MAGIC telescopes were equipped with two different camera geometries and two different readout technologies, both accounted for in the Monte Carlo simulation (see chapter 3).

About 60% of the observations were carried on in the standard false-source tracking mode, dubbed "wobble" mode, the remaining 40% in on-source mode (see §**??**). The on-source observation mode was chosen for low-zenith observations specifically dedicated to pulsar search: for these observations there was a need of operating the legacy MAGIC-1 sum trigger in parallel to the stereo trigger, and the sum trigger was meant to be used for standalone, on-source observations only.

Normally the on-source observation mode is never used when observing with stereo trigger because it precludes background estimation without independent off-source observations. This is not an issue when dealing with pulsed data since signal and background are extracted from the phase of the events (e.g. in time domain) and not from their arrival direction in the sky with respect to the position of the source (e.g. in space domain). The merging of both wobble and on-source datasets did not represent a problem for pulsar observations, however many of the checks could be carried out for wobble data only, as it will be shown in the following.

For what regards the quality selection, data affected by hardware problems, bad atmospheric conditions, and unusual analysis rates was rejected in order to ensure a stable performance. The cuts adopted are the same as in Zanin (2011):

- "Cloudiness" lower than 50%
- Analysis rate (e.g. absolute event rate after image cleaning and after a size cut at 100 photo-electrons) within 30% of the mean value, 86 Hz.

An additional cut was applied: to ensure a low threshold, only data with zenith angles below 35° was considered.

Furthermore, the data was checked for consistency on a day-to-day basis. A preliminary analysis with standard cuts was performed, extracting the rate of gamma and background events above 250 GeV (i.e. without considering the pulse phase) for each day.

In the case of wobble data, gamma and background event rates could be taken into consideration separately, their mean value for the whole dataset being 4.53 ± 0.97 and 0.28 ± 0.15 events per minute, respectively.

For on-source data, only the cumulative gamma+background rate could be calculated, its mean value for the whole dataset being 4.44 ± 0.81 events per minute.

Days in which the absolute value of any of the above rates differed by more than 30% from the corresponding all-time mean were discarded. Also discarded were days in which the rate was more than 3.5 σ away from the all-time mean, with σ being the error on the daily rate.

After these cuts and checks, the total effective time of these observation summed up to a total of 72.78 hours, as reported in table 5.3.

Table 5.3: Effective time after quality selection

	Cycle V ('09/'10)	Cycle VI ('10/'11)	All data
Wobble	22.62 h	20.42 h	43.04 h
On-source	6.68 h	23.06 h	29.74 h
		Total:	72.78 h

Data Processing

For the data analysis, we used the standard MAGIC analysis package MARS (Moralejo et al. 2009; Aleksi⊠et al. 2012 and §**??**),

The shower images were cleaned applying the so-called sum cleaning (Lombardi (2011) and §**??**) which shows a significant improvement in rejecting the background at low energies, and consequently in the analysis sensitivity in the most important region for pulsar studies. The cleaning levels chosen were the standard ones used in Zanin (2011): for MAGIC-I the "core" level was set to 4 phe, the "boundary" to 3 phe; for MAGIC-II the corresponding values were higher at 7 and 4 phe, respectively. This difference was motivated by the higher noise level of the MAGIC-II readout.

The maximum allowed arrival time differences were set for both telescopes at 0.9, 1.2 and 1.9 ns for 2NN, 3NN and 4NN groups, respectively.

To ensure consistency with the reference analysis of the Crab Nebula described in Zanin (2011), the signal in each pixel was clipped at 750 phe. This setting was shown to have little if no impact in the latter analysis steps.

As usual, the Hillas image parametrization Hillas (1985), with additional parameters described in chapter 3.

For the gamma/hadron separation and gamma direction estimation the random forest (RF) technique was applied (Albert et al. (see, e.g., 2008a) and §**??**).

5.3 Optimized cuts

The analysis of the Crab pulsar presents a rather peculiar case: the background is dominated by gamma rays coming from the Crab nebula instead of hadrons already above ~ 120 GeV.

To boost the sensitivity it is therefore important to include all possible gamma-ray candidates in the analysis. To accomplish this, an ad-hoc optimization of the cuts in Hadronness and θ^2 was carried out.

The optimization criterion was the maximum significance calculated like this:

$$\sigma_\gamma = \mathrm{LiMa}\left(N_{on}\frac{\Gamma_{TP}}{\Gamma_{OP}} + N_{ex}\alpha, N_{on}, \frac{\Gamma_{TP}}{\Gamma_{OP}}\right) \tag{5.1}$$

where:

LiMa(ON, OFF, ALPHA) is the significance calculated following equation 17 from Li and Ma (1983). Usually the ON is the number of "signal" events, OFF the number of background events and alpha is the normalization parameter;

N_{on} is the number of events in the off-peak region (OP), here defined as [0.52⊠0.87] that survive the Hadronness and θ^2 cuts;

N_{ex} is the total number of excesses (i.e. gamma events) from the Crab nebula. This is the number of events passing the cuts minus the background events N_{off};

N_{off} is the number of background events. In the case of wobble mode observations, N_{off} is the number of events that passing the same cuts as the "signal" events, but using θ^2 calculated with respect to the anti-source position. In case of on-source observations, N_{off} is estimated by extrapolating linearly the θ^2 distribution in the 0.1 - 0.35 region;

Γ_{OP} and Γ_{TP} are the relative widths of the off-peak and the union of the peak regions (P1 P2 = TP) bins, respectively;;

α is the ratio between the energy fluxes of the Crab nebula and the Crab pulsar, as found in Zanin (2011) and Saito (2010), respectively.

σ_γ "simulates" the significance that one would observe from the pulsar emitting in the phase integral TP, with a gamma-dominated background coming from the nebula. In fact, the number of background events OFF is taken as the same "signal" events (that would be the ON events in the usual case) while the ON events are the same background plus the nebular excess scaled to the flux ratio, i.e. the excess that one would expect from a source with a spectrum similar to that of the pulsar.

In order to find the optimum cuts, the value of σ_γ was calculated for a three dimensional grid in energy, Hadronness and θ^2. The result of this scan, shown in Fig. . 5.2, is that σ_γ, for the energies at which it could be reliably calculated, has a broad maximum located roughly at Hadronness > 0.3 and $\theta^2 > 0.02$. The cut values listed in table 5.4 were chosen somewhat arbitrarily around the center of this maximum region, whenever it could be found. The absolute maxima σ_γ were neglected since its usage produced a non-smooth cut evolution with energy.

The validity of the cuts was later checked by applying them to the analysis of the Crab nebula signal: the reconstructed spectrum was in good agreement with the fiducial one.

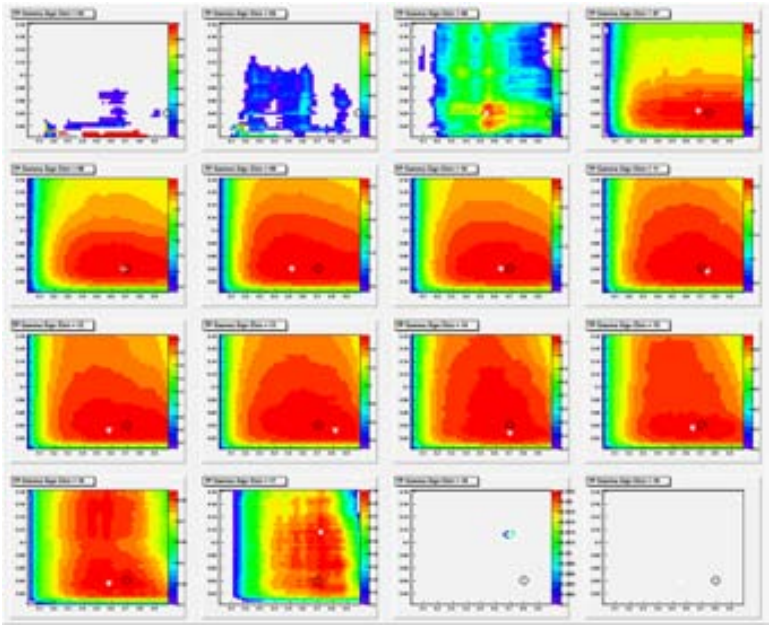

(a) Scans for wobble data

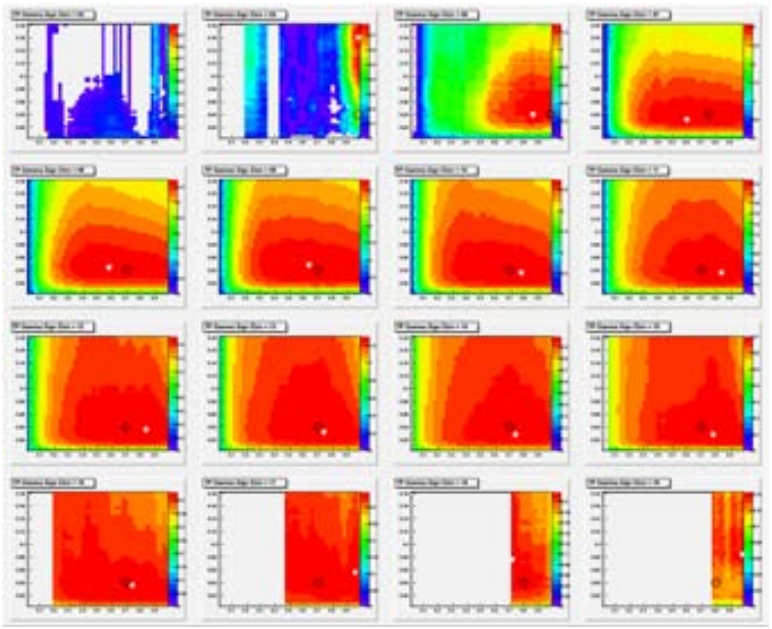

(b) Scans for on data

Figure 5.2
Scan of σ_y in energy (individual plots), Hadronness (x-axis) and θ^2 (y-axis) for wobble and on data. The energy bins indicated in the titles refer to those in table 5.4. The white stars indicate the position of the maximum, while the black crosses the chosen values for the cuts. Some of the plots are empty, where the

Table 5.4: Optimized selection cuts on Hadronness and θ^2.

Energy bins (GeV)			Cut value		Cut efficiency (%)	
Bin N.	E min	E max	Had	Th2	Had	Th2
01	7.2	10.4	0.98	0.040	100	42
02	10.4	15.1	0.98	0.040	100	49
03	15.1	21.8	0.98	0.040	100	69
04	21.8	31.5	0.98	0.040	100	61
05	31.5	45.6	0.98	0.040	100	51
06	45.6	65.9	0.98	0.030	100	54
07	65.9	95.3	0.75	0.030	97	62
08	95.3	137.7	0.70	0.030	98	73
09	137.7	199.0	0.70	0.030	99	83
10	199.1	287.7	0.70	0.030	99	90
11	287.7	415.9	0.70	0.030	99	93
12	415.9	601.1	0.70	0.030	99	96
13	601.1	868.9	0.70	0.030	99	97
14	868.9	1255.9	0.70	0.030	99	97
15	1255.9	1815.4	0.70	0.030	99	98
16	1815.4	2624.0	0.70	0.030	99	99
17	2624.0	3792.9	0.70	0.030	99	99
18	3792.9	5482.4	0.80	0.030	100	99
19	5482.4	7924.5	0.80	0.030	100	100
20	7924.5	11454.3	0.80	0.030	100	100
21	11454.3	16556.6	0.80	0.030	100	100
22	16556.6	23931.5	0.90	0.030	100	99
23	23931.5	34591.5	0.90	0.030	100	99
24	34591.5	50000.0	0.90	0.030	100	100

5.4 Phase calculation

The phase of each event with respect to the main radio pulse was calculated using the TEMPO2 package (Hobbs et al., 2006): for this purpose an ad-hoc plug-in was written in order to feed MAGIC data to TEMPO2.

The calculation of the phases consist of two steps as described in chapter 3: at first the arrival time of the event, given by a high precision GPS clock coupled with a rubidium oscillator, is transformed to the solar system barycenter. Secondly, the pulse phase ☒ is calculated from the ephemeris using a Taylor expansion as in **??**.

TEMPO2 was preferred over self-written phase-calculation code because of its simplicity and robustness, given the fact that it is the de-facto standard tool for radio pulsar timing. Another advantage is that the plugin empowers the MAGIC collaboration to make use of its many advanced features such as timing noise corrections or binary system calculations, which were not exploited in this analysis.

The ephemerides used for the phasing were the monthly ephemerides publicly provided by the Jodrell Bank Observatory (Lyne et al., 1993). They were checked for consistency with the ephemerides provided in the Fermi-LAT Crab Pulsar paper (Abdo et al., 2010), and minor differences were found of less than 0.001 in phase. The Fermi-LAT ephemerides are possibly more accurate since they accounted for timing noise corrections, however they are only valid for a part of the time span of the MAGIC observations, and were not used further on.

The validity of the whole timing chain was checked - when possible - by measuring the optical pulsation from the Crab pulsar with the central pixel in MAGIC-I. This method could only be applied to on-observations, and not for all of them, since the central pixel hardware suffered some failures between 2009 and 2012. Nevertheless, whenever the system was operating nominally, a strong pulsation was detected, with a sharp main peak aligned to the phase 0, as can be seen in Fig. 5.3.

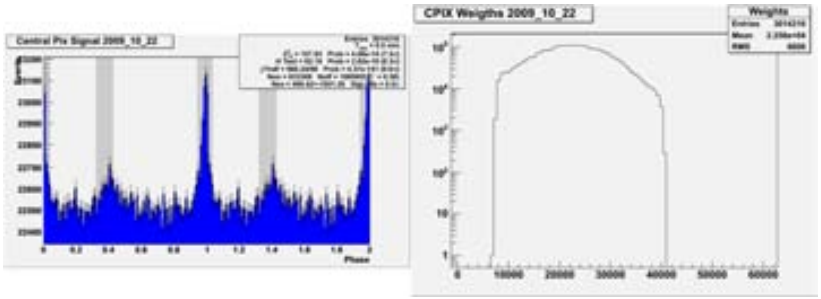

Figure 5.3
Example of optical signal from the Crab pulsar detected with the central pixel. The folded light curve shows that peak positions and relative heights correspond to the expected ones.

5.5 Folded light curves and detection of the pulsation

For the determination of the folded light curve (also called phase histogram, or phasogram), only correctly reconstructed stereoscopic events passing the above-

mentioned Hadronness and θ^2 cuts were considered. The energy range selected was from 46 to 416 GeV in estimated energy, corresponding to a median true energy of 100 GeV, estimated from simulations. The lower limit roughly[1] corresponds to the lowest energies that could be reconstructed in the Crab Nebula spectral analysis of Zanin (2011) (about 50 GeV), while the upper limit was chosen to match the upper extension of VERITAS measurement (about 400 GeV, see Aliu et al., 2011).

This energy range was further divided into two sub-ranges, spaced logarithmically: a "low-energy" one between 46 and 138 GeV and a "high-energy" one from 138 to 416 GeV. The median true energy for these two subranges was estimated from simulations to be 80 GeV and 180 GeV, respectively.

With the above selections, three folded light curves were obtained, shown in Fig. 5.4. The significance of the pulsation was tested against the null hypothesis of a uniform distribution using the Z^2_{10}-test, the H-test (de Jager et al., 1989) and a simple ☒^{2}-test. None of these tests makes an a priori assumption concerning the position and the shape of the pulsed emission. The significances that these tests yielded for the different energy ranges considered are displayed in table 5.5.

Table 5.5: Energy ranges and corresponding a priori pulsation significances, calculated with different uniformity tests. The pulsation is detected in all cases.

	Energy (GeV)			Significance (σ)		
Range	E_{min}	E_{max}	$\overline{E_{\mathrm{true}}}$	Z^2_{10}-test	H-test	☒^{2}-test
Low	46	138	80	6.2	5.7	5.1
High	138	416	180	4.5	4.0	3.4
All	46	416	100	8.6	6.4	7.7

Fits to the light curves

The all-energy folded light curve was very finely binned and a function with two peaks and a constant background was fitted to it by maximizing the likelihood (for the Poisson case, since the average number of entries per bin was very low) by means of the MINUIT (James and Roos, 1975) package inside ROOT (James and Roos, 1975). For the functional form of the peaks Gaussian and Lorentzian functions were tried. The resulting peak positions and widths at half the maximum (FWHM) are displayed in table 5.6.

The signal in P2 is strong enough to also be fitted with an asymmetric Lorentzian, which involves more parameters. This was not possible for P1 because the fit parameters did not converge to a stable solution. The results are displayed in Fig. 5.5.

All fits to the data yield very similar results and likelihood values, so it was not possible to support or rule out the presence of thicker tails implied by a Lorentzian

[1]The exact values are somewhat arbitrary: for consistency with the spectral analysis they were chosen as the bin edges closest to 50 GeV and 400 GeV of a logarithmically-spaced energy binning spanning from 5 GeV to 50 TeV

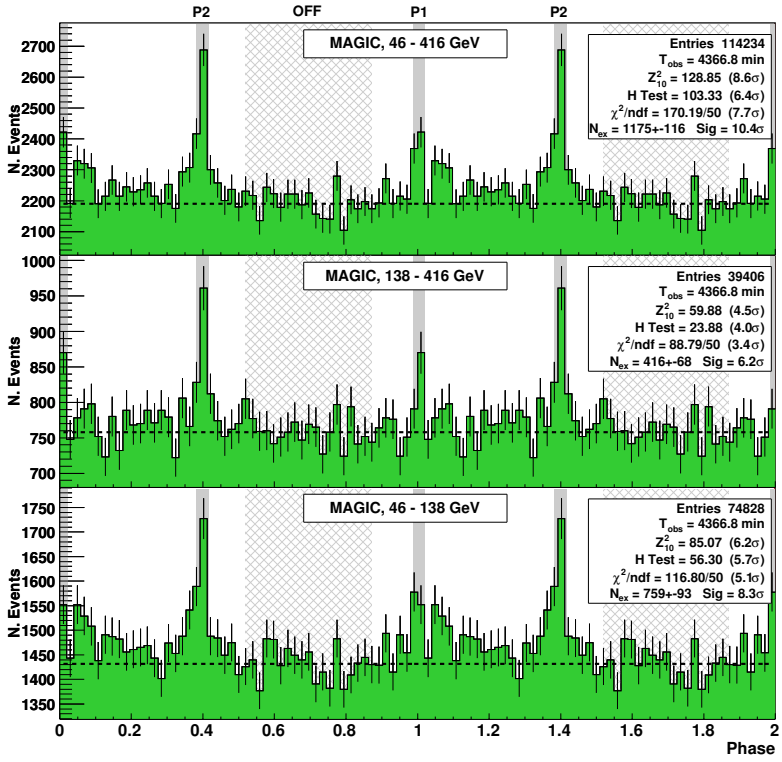

Figure 5.4
MAGIC folded light curves of the Crab pulsar for the total range in estimated energy and for two separate subranges. The shaded areas are the on-phase regions $P1_M$ and $P2_M$ chosen after fitting (see §??), the light shaded area is the off-region [0.52–0.87], from Abdo et al. (2010). The dashed line is the constant background level calculated from that off-region.

Table 5.–: Results of the fits on the Crab pulsar folded light curve, in terms of peak positions and widths

	P1		P2	
Peak Type	Position	FWHM	Position	FWHM
Gaussian	0.005 ± 0.003	0.025 ± 0.007	0.3996 ± 0.0014	0.026 ± 0.004
Lorentzian	0.005 ± 0.002	0.025 ± 0.008	0.3993 ± 0.0015	0.023 ± 0.004

function. Furthermore, the asymmetric fit does not yield a significant difference in the leading and trailing wings of P2. Hence, the Gaussian parametrization was deemed sufficient to describe the peaks.

A positive excess throughout the region between the two peaks can be observed. Its most prominent trait is the trailing wing of P1, defined as [0.04–0.14] in Fierro et al. (1998), whose significance corresponds to 3.4σ using equation 17 of Li and Ma (1983), henceforth Li & Ma significance. This hint can be confirmed only once more data is collected.

A bridge emission between the two peaks in the lowest energy range is expected, since in the Fermi-LAT data (Abdo et al., 2010) the bridge emission is evident up to at least 10 GeV, and it is spectrally harder than the peak emission. However no significant signal was found in the MAGIC data: the emission, if there, is too low for spectral analysis and will not be further considered.

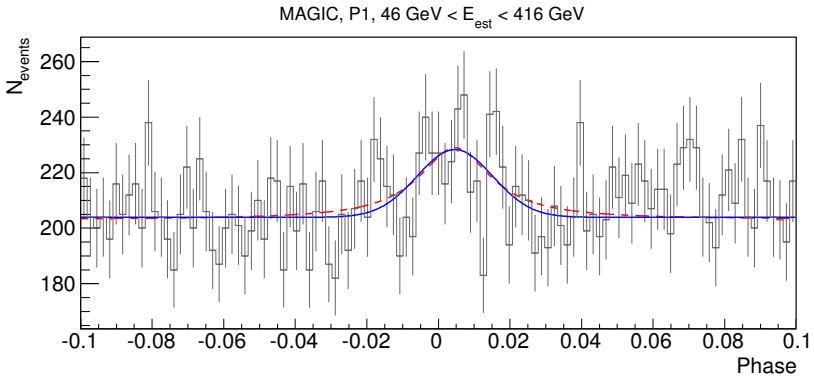

(a) Fit to P1

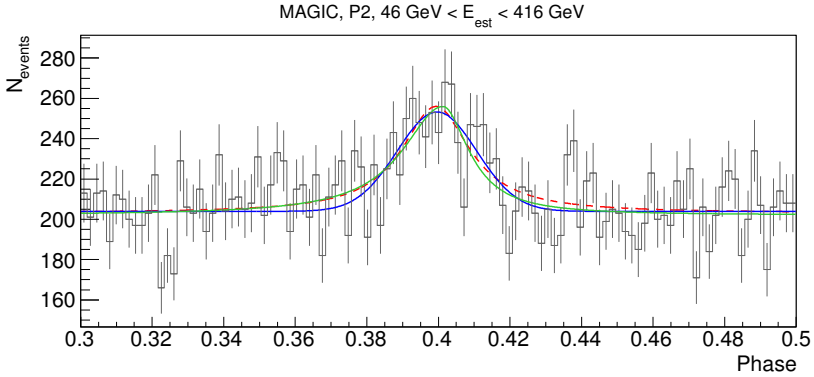

(b) Fit to P2

Figure 5.5
Close-up display of the two peaks P1 and P2 using a finer binning than in Fig. 5.4. The blue curve represent the Gaussian functions used to defined the a posteriori phase intervals. Also displayed as red dashed lines are the Lorentzian functions, while the asymmetric Lorentzian function fitted to P2 only is displayed as a green dashed line. Note that the binning used for the fits is much finer than the one displayed.

Definition of the peaks

The peak shapes found in the fits described above are significantly narrower than those found in the GeV regime: considering Fermi-LAT, MAGIC mono and VERITAS data together with these results, a consistent narrowing trend from GeV to beyond 100 GeV could be established, as shown in Fig. 5.6.

The consequence is that the excess in the present data is much more concentrated in phase than the wide peak ranges defined in Fierro et al. (1998) ($P1_E$ = [0.94⊠0.04] and $P2_E$ = [0.32⊠0.43], where the subscript "E" stands for EGRET-defined, in contrast to the MAGIC and VERITAS definitions below).

Also, the broader EGRET phase definitions leads to the integration of an unnecessarily large number of noise events, which penalizes the accuracy of the spectral reconstruction.

Therefore, the spectrum was investigated considering both phase interval definitions: the EGRET, a priori ones, and narrower ones defined a posteriori, labelled "M" for MAGIC from now on. The latter were defined as in Aliu et al. (2011): centered on the Gaussian peak positions and 2σ wide, resulting in $P1_M$ = [0.983⊠0.026]

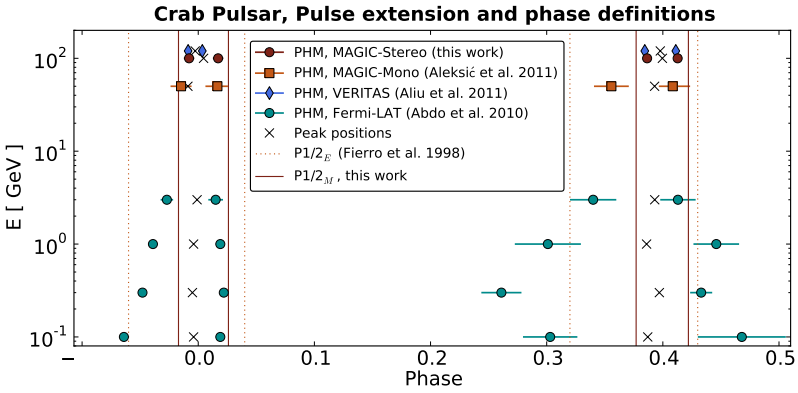

Figure 5. Compilation of the positions (crosses) and widths (solid points representing the phases of the half-maxima) of the two peaks P1 and P2 across 3 decades in energy. Vertical hashed lines indicate the phase range definitions later used for the spectra. The values are from Fermi-LAT (Abdo et al., 2010, light circles), MAGIC-Mono (Aleksi et al., 2011, squares), VERITAS (Aliu et al., 2011, diamonds) and MAGIC stereo (this work, dark circles).

and $P2_E$ = [0.377–0.422].

Given these definitions, the significance of the signal in these intervals could be calculated with equation 17 from Li and Ma (1983), with "off" events coming from the off-phase interval [0.52–0.87] from Abdo et al. (2010).

An overview of the different phase interval definitions is given in table 5.7, while the Li & Ma significances for the EGRET and MAGIC phase intervals are given in table 5.8.

Table 5.7: Phase interval definitions for main radio peak (P1), secondary peak (P2) and off-phase region (OP)

	EGRET	MAGIC	VERITAS
P1	[-0.06–0.04]	[-0.017–0.026]	[-0.013–0.009]
P2	[0.32–0.43]	[0.377–0.422]	[0.375–0.420]
OP	[0.52–0.88]	[0.52–0.87]	[0.43–0.94]
(P1+P2)%	21.0%	8.8%	6.7%

Table 5.8: Li&Ma significances for EGRET and MAGIC phase interval definitions used later in the reconstruction of the energy spectrum.

Definition	P1+P2	P1	P2	P1/P2 ratio
EGRET	7.5σ	4.3σ	7.4σ	0.46 ± 0.13
MAGIC	10.4σ	5.5σ	9.9σ	0.54 ± 0.12

The phase interval definitions are equally valid: on one hand, the EGRET phase definitions are free from the selection bias, but lead to higher noise contribution; on the other hand the narrower MAGIC intervals have lower noise, but are affected by a (minor) selection bias. The VERITAS intervals are similar to the MAGIC ones, if not a bit narrower still, and will not be used in the following analysis.

The emission ratio between the two peaks P1/P2 was found to be around 0.5, with the values calculated for the two phase definitions (shown in table 5.8) well agreeing with each other.

The differences in the pulse shape parameters between the two energy sub-ranges were found to be not relevant: the width, position and relative intensity of the two peaks did not change by much. The invariance of the width is probably related to the fact that the median energies of the two energy sub-ranges considered are comparably close to each other (80 and 180 GeV), making the width difference small compared to the energy dependent trend.

5.6 Energy spectra

The energy spectra for (P1+P2), P1 and P2 were calculated extracting the excess events from the corresponding phase regions after the above-mentioned cuts, and binning them with respect to their estimated energy in 25 logarithmically-spaced bins between 5 GeV and 50 TeV. The background came from the off-peak region and was normalized accordingly to its relative width. The effective area was calculated separately for on-source and wobble observations using the corresponding Monte Carlo simulations. The effective time was calculated assuming a readout dead time of 5 ms.

The spectral parameters and the χ^2 values were determined after unfolding, i.e., correcting the spectrum for the migrations and the energy biases expected in the threshold regime. During unfolding iterations, the simulated events are re-weighted each time with the appropriate spectrum derived in the previous iteration. The forward unfolding algorithm (Albert et al., 2007) was used, which is the most robust method to pa-ra-me-tri-ze the data. On-source and wobble data were joined together in this analysis step.

The spectra were calculated for both the MAGIC phase intervals (shown as red squares in Fig. 5.7) and for the unbiased EGRET ones (yellow circles). They could be described by power laws with the values displayed in table 5.9. Notably, the χ^2 values found are not optimal, especially for the spectrum of $P1_M$. Considering the systematic uncertainties the significance of this inconsistency is too low to claim any spectral feature, at least with the present dataset.

The ratio of the normalization constants between P1 and P2 at 100 GeV is 0.4 ± 0.2, fully compatible with the value of 0.5 ± 0.1 derived from the analysis of the folded light curve in the previous section.

Consistency checks

Due to differences in the selection of the peak phases, a small discrepancy in the flux measurement between the EGRET phase intervals and the MAGIC ones is expected. In fact, the spectra resulting from the EGRET and MAGIC phase definitions display

Table 5.9: Results of the spectral fits on the spectra obtained for the MAGIC and EGRET intervals. The fitting functions are power laws of the form $dN/dE = f_0(E/100GeV)^{-\gamma}$; the units of f_0 are 10^{-11} cm s^{-1} TeV^{-1}.

Phase	f_0	γ	χ^2/n.d.f	Prob
$(P1+P2)_M$	13.0 ± 1.6	3.57 ± 0.27	10.3/4	0.04
$P1_M$	3.9 ± 1.7	4.0 ± 0.8	9.3/2	0.01
$P2_M$	8.8 ± 1.0	3.42 ± 0.26	6.1/5	0.30
$(P1+P2)_E$	15.5 ± 2.9	3.9 ± 0.4	9.5/4	0.05
$P1_E$	6.5 ± 2.0	3.3 ± 1.0	3.8/2	0.15
$P2_E$	11.2 ± 1.9	3.7 ± 0.4	7.2/5	0.21

a minor systematical difference: the spectral points of the latter are all somewhat below the former.

This is self-consistent, since the EGRET intervals enclose the MAGIC intervals, causing more background events to enter the calculation but also covering the totality of the pulse: the MAGIC intervals instead could leave some of the excess out (as can be seen in table 5.7, the EGRET phase intervals cover 21% of the whole phase, are more than two times wider than MAGIC intervals, which cover only 8.8%).

The smallness of the effect shows that the selection bias affecting the MAGIC phase intervals is not a significant one.

The spectra obtained for $(P1+P2)_M$ were cross-checked for consistency by comparing 2009/10 and 2010/11 data, on-source and wobble data, two different zenith angle ranges, two quality cut levels and two unfolding algorithms. No discrepancy was found in any of these checks, the spectrum was always stable within the errors.

Furthermore, the spectrum of the Crab nebula was determined from the same data (using only the wobble mode dataset), with the same cuts, energy range and binning. This check ensure the understanding of all possible systematic errors, since the nebula spectrum was found to be in agreement with the most recent Crab nebula analysis (that of Zanin, 2011), as well as with the Fermi-LAT results (in Abdo et al., 2010). This confirms the performance of our spectral analysis down to 46 GeV, since also the Crab nebula flux could be reconstructed down to about those energies (55 GeV), agreeing within errors with the function derived by the combined Fermi-LAT/MAGIC fit in Zanin (2011), which is not sensitive to the lowest MAGIC point since it is determined by much more precise points a higher and lower energies.

These checks indicate that the systematic flux uncertainties are not different than the standard one for low-energy observations given in Aleksi☒ et al. (2012). These systematic uncertainties are 17% on the energy scale and 19% on the flux normalization (shown as a grey arrow in Fig. 5.7). If one assumes a photon index of 3.6, the total flux uncertainty including the energy bias is ∼ 44% at low energies. The systematic uncertainty on the spectral index for such a soft spectrum is approximately 0.2

Since all MAGIC spectra shown in Fig. 5.7 are unfolded, the statistical errors are correlated by a factor 20–60%. This reflects the energy resolution and bias, which vary between 15% and 40% (see Aleksi et al. (2012) and chapter 3).

Comparison with other data

The EGRET spectra presented in this work can be compared directly with previous studies, especially the MAGIC monoscopic observations reported in Saito (2010) and Aleksi et al. (2011). The stereo results are compatible with the monoscopic ones, since the statistical deviations are of at most 2σ, and many of the systematic errors are independent. These new measurements, however, support the possibility of an over-estimation of the gamma-ray energy scale in the mono data, already taken in consideration in Saito (2010).

Figure 5.7 also shows the Fermi-LAT spectra in the EGRET intervals determined in Aleksi et al. (2011): they extrapolate consistently to the monoscopic and stereoscopic spectra within the uncertainties. The black dashed curve in the same figure display an estimation of the Fermi-LAT spectrum in the MAGIC phase range, obtained from a linear combination of the fit functions $f_i(E)$ describing the phase-resolved spectra provided in Abdo et al. (2010), an extrapolation possible because said functions have flux constants that are differential in phase:

$$f_{\mathrm{M}}(E) = \sum_i a_i f_i(E). \tag{5.2}$$

The coefficients a_i of this linear combination were proportional to the relative width of the intersection between the corresponding phase interval P_i and the MAGIC one:

$$a_i = \frac{\mathrm{P}_i \quad \mathrm{P}_{\mathrm{M}}}{\mathrm{P}_i}. \tag{5.3}$$

If P_i is full contained by the MAGIC interval, then $a_i = 1$; if it is only partly contained $0 < a_i < 1$, and if it's out $a_i = 0$.
As expected, the resulting GeV spectrum for the narrower MAGIC phase intervals is substantially lower than the one calculated from the EGRET intervals.

Finally, for a correct comparison of the energy spectra found in this work with those extracted from Fermi-LAT, VERITAS or previous MAGIC monoscopic data, it is relevant to mention that the different energy-dependent systematic uncertainties of these experiments, which altogether add up to 10% to 30% in energy, can be the source of possible discrepancies, in addition to the differences in phase interval definitions.

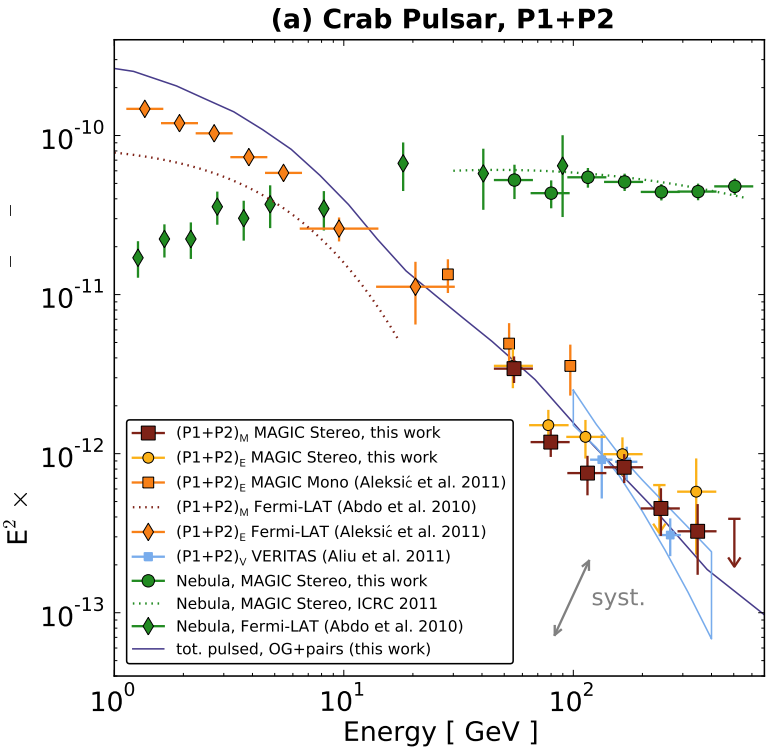

(a) SED for P1+P2

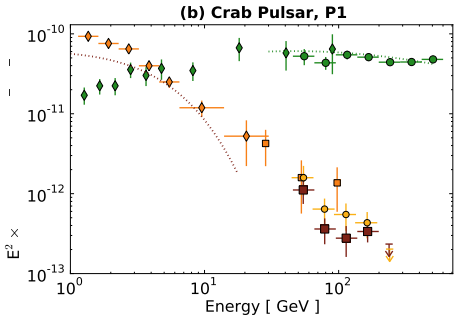

(b) SED for P1

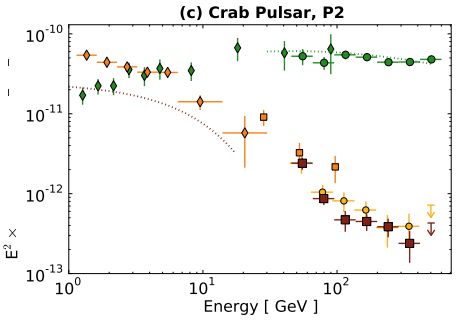

(c) SED of P2

Figure 5.7
Compilation of spectral measurements of the Crab pulsar by MAGIC mono (Aleksi⊠ et al., 2011, yellow squares,), MAGIC stereo, (this work, red squares), VERTAS (blue squares, from Aliu et al., 2011) and Fermi-LAT (yellow diamonds, from Aleksi⊠ et al., 2011). The spectrum of the two peaks together is shown in a); in b), c) each peak separately. Additionally, the yellow circles are the spectra calculated with respect to the EGRET bins, while the green diamonds and circles are the spectrum Crab nebula from Fermi-LAT data (from Aleksi⊠ et al., 2011) and MAGIC wobble data, respectively. The meaning of the dashed and solid curves is explained in §?? and ??, respectively.

5.7 Discussion

The pulsed VHE γ-ray signal from the Crab pulsar reported in this thesis has been detected with a very high confidence, and the spectra presented in the previous section have an unprecedented energy range and phase resolution.

The breadth of the checks performed on the data, which included using different phase intervals and checking the reconstruction of the spectrum with the Crab nebula, leave absolutely no doubt about the solidity of the measurement of both light curves and spectra. At high energies, the P1+P2 spectrum and the lightcurve (including position and width of the peaks) agree well with the published results of VERITAS.

The spectrum presented here spans about an order of magnitude in energy, and together with the MAGIC monoscopic (Aleksi⊠et al., 2011) and the Fermi-LAT data (Abdo et al., 2010), it provides the first phase-resolved spectrum of a pulsar in γ-rays between 100 MeV and 400 GeV, an unprecedented achievement.

The results above show that the VHE spectrum of the Crab pulsar does not show any exponential cutoff; it rather resembles a power law up to at least 400 GeV.

This is inconsistent with the widely accepted predictions of both the "classical" models of high-energy γray emission from pulsars (illustrated in more detail in §**??**): in the polar cap scenario, where particle acceleration happens close to the poles, the cutoff is should be super-exponential and it is due to γ-ray attenuation due to pair production in the strong magnetic field close to the pulsar poles.

In the simplest versions of the outer magnetospheric models, particles are accelerated very close to the light cylinder (outer gap) or all along the last open field lines (slot gap), and γ-rays are produced as the result of the curvature radiation by $e^{\pm}$ migrating along curved paths following the lines of the pulsar magnetic field lines. In this scenario, the cutoff is milder, and its energy roughly corresponds to the highest characteristic curvature-radiation energy of the particles accelerated in the pulsar magnetosphere (see §2.1).

A theoretical interpretation of this deviation from the exponential cutoff was formulated with the help of K. Hirotani: its results are shown as a violet solid line in Fig. 5.7, and its derivation is briefly discussed in the following. For more detailed information on this model, see Hirotani (2006).

A possible model in the framework of OG

In general a pulsar magnetosphere cannot accelerate electrons and positrons ($e^{\pm}$) unless the magnetic-field-aligned electric field, $\mathbf{E}_{\parallel}$ is non-zero, i.e., the charge density ρ differs from the Goldreich-Julian ρ_{GJ} density (see equation 2.19)

To derive $\mathbf{E}_{\parallel}$, the inhomogeneous part of the Maxwell equations must be solved (Fawley et al. 1977; Scharlemann et al. 1978; Arons & Scharlemann 1979):

$$\cdot \mathbf{E}_{\parallel} = 4\pi(\rho - \rho_{\mathrm{GJ}}), \tag{5.4}$$

The standard picture of the Outer Gap and Slot Gap models is that if $\rho \quad \rho_{\mathrm{GJ}}$, particle acceleration takes place, a gap forms, and high-energy photons are emitted by the electrons and positrons curving along the magnetic field lines of the pulsar.

In order to derived a detailed, self-contained solution for this model constraining ρ, $E_{\parallel} = |\mathbf{E}_{\parallel}|$ and the gap geometry, it is necessary to solve the Poisson equation (), together with the Boltzmann equation for $e^{\pm}$ and the radiative transfer equation, taking into account general relativistic effects due to the extremely intense gravitational field inside the pulsar magnetosphere. This approach is similar to what described in (Beskin et al. 1992; Hirotani & Okamoto 1998; Hirotani & Shibata 1999a, 1999b; Hirotani et al. 1999; Takata et al. 2006).

The angle between the rotational and the magnetic axes for the following calculations was set to $\alpha = 65°$, and the observer's viewing angle to = 106°.

Of capital importance in this framework is the electron-positron pair creation at each point of the gap: in fact, in contrast with previous quantitative OG models, this model proposes non-vacuum ($\rho \quad 0$) , in which several generations of pairs and γ-ray are produced in a self-seeding cascade mechanism.

The first generation of $e^{\pm}$ pairs are created from $\gamma + \gamma$ interactions in the gap, and are accelerated by $E_{\parallel}$ to attain high Lorentz factors, up to $\gamma \sim 10^{7.5}$.

The particles accelerated inwards (assumed they are $e^{\text{Ú}}$) emit via curvature radiation and inverse Compton scattering γrays, which in turn undergo pair production with the thermal X-ray photons from the pulsar surface. The part of these pairs created inside the gap replenish the first generation $e^{\pm}$ (self-seeding); the other pairs are considered second generation.

The particles that are accelerated outwards (in this case e^{+}) instead undergo the same process, but the γrays only give rise to second generation pairs, which will also be accelerated, to only $10^{3.5} \quad \gamma \quad 10^{7}$.

The secondary pairs repeat the same process, but at a higher altitude in the pulsar magnetosphere, creating tertiary pairs with $10^{4} \quad \gamma \quad 10^{6}$. A more in-depth description of the cascade can be found in Aleksi et al. (2011) and in Hirotani (2006). A variant of this model with an analytical considerations about the multiplicities of higher-generation pairs can be found in Lyutikov et al. (2012).

In this model, the origin of the HE and VHE γ-ray emission from the pulsar lies in the outflowing secondary and tertiary $e^{\pm}$ pairs: via inverse Compton they can upscatter magnetospheric infrared to ultraviolet photons up to energies of ~ 1 TeV. If this happens out enough in the magnetosphere, these secondary and tertiary VHE γphotons can escape pair absorption and result in a measurable pulsed VHE γ-ray emission.

In (Aleksi⊠et al., 2011), the calculations of both $E_{\parallel}$ and the resultant γ-ray emission (via curvature radiation and IC scattering of all generations of $e^{\pm}$) were carried out up to $0.7R_{\rm LC}$, where $R_{\rm LC}$ is the radius of the light cylinder, about 1×10^4 km in the case of the Crab pulsar.

An extension of the calculation was performed up to $0.9R_{\rm LC}$ for $E_{\parallel}$ and up to $1.5R_{\rm LC}$ for the γ-ray emission, justified by the fact that primary IC emission is important near the light cylinder, had the consequence of increasing the inward flux of primary gamma rays originating from the upper side of the gap, which leads to a higher abundance of pair-produced $e^{\pm}$ at lower altitudes ($< 0.6R_{\rm LC}$). This is remarkable in the sense that it increased the screening of $E_{\parallel}$ in the inner magnetospheric regions, reducing the curvature radiation component from the primary pairs and making the predicted spectra more compatible with the Fermi-LAT data at GeV energies. At the same time, this extension of the calculation up to almost the light cylinder did not influence the secondary and tertiary components at energies beyond few GeV.

Conclusion

The revised model just presented here could reproduce reasonably well the total pulsed emission between 1 and 400 GeV, however one of the shortcomings of the model is that it includes a bridge emission, not contained in the P1+P2 spectrum. Therefore it slightly overestimates the Fermi-LAT flux points in figure 5.7. A phase-resolved modeling is challenging and the spectral shape above 100 GeV is difficult to compute with high precision. This is because the $\gamma - \gamma$ cross section, which affects both pair production and γ-ray absorption, depends on the square of the collision angle. Small variations in the geometry of the magnetosphere and of the emitting region can have a large impact on the flux that escapes the pulsar.

Therefore, this model should not be interpreted as a hard quantitative prediction; instead, it is meant to show that the hard component we see in the experiment can quantitatively be met within the present understanding of the OG model. Similarly, the slight modulations of the power law component are not to be interpreted as a significantly predicted feature.

Other possible hypotheses that have been put forward to explain the VHE emission from the Crab pulsar include the production of inverse Compton radiation in the unshocked pulsar wind outside the light cylinder by pulsed X-ray photons (Aharonian et al., 2012; Aharonian and Bogovalov, 2003); a striped pulsar wind (P"tri, 2011), the annular gap model of Du et al. (2012) or curvature radiation at the light cylinder gap (Bednarek, 2012).

Some of these models predict some spectral features: (Aharonian et al., 2012) foresees the onset of a hard component at energies greater than $\sim$ 30 GeV and a corresponding spectral upward-kink in this transition region, others models (Aharonian et al., 2012; Bednarek, 2012) have a cutoff at few hundred GeV.

These spectral features are crucial to establish to test these models. They are in energy ranges within the reach of present generation of Air Imaging Cherenkov Telescopes, and especially MAGIC is in the position to probe them with further dedicated in-depth observations.

Another topic that it will be possible to address with a 2⊠3 times larger dataset is the energy dependence of the pulse shape parameters. The narrowness of the pulses and its evolution with energy are a stringent requirement that the theoretical modeling must fulfill because the folded light curve is almost stable against systematic uncertainties.

Moreover, the indication of pulsed emission in the trailing wing of P1 may indicate that a VHE signal between the two peaks might be within reach.

The MAGIC Telescopes, after the 2011/2012 upgrade, have just started a pulsar observation campaign which will address these issues.

5.8 Outlook

Our knowledge of the emission of neutron stars at very high energies is very much based on a single source, the Crab pulsar. It is still unknown if the Crab is unique or such a pulsed VHE tail is a common feature present also in other pulsars. The next big step in the VHE study of pulsars is to go from one to many.

It is therefore very important to try to discover new pulsars through observations of other candidate sources. On the other hand, a deeper insight on the Crab itself and higher precision measurements can help understand its physics, and make educated guesses about the feasibility of detecting other VHE pulsars. The questions that are left to answer, for this and the next generation of IACTs are:

- Is there another γ-ray pulsar at VHE? If so, is its spectrum similar to the one of the Crab? The three best candidates for Cherenkov telescopes taking into account their fluxes above 10 GeV: the Crab, the Vela and the Geminga pulsars. Future observations should concentrate on these candidates, unless Bednarek's model is proven right and some attention should be diverted from Geminga towards millisecond pulsars.
- Up to which energies does the Crab pulsar spectrum extend? A spectral point at ~ 500 GeV would allow to discriminate between Aharonian's and Hirotani's models, unveiling where the electron acceleration region is located.
- Is the Crab pulsar spectrum showing a spectral hardening at ~ 30 GeV? Such a feature would favor Ahoronian's model over all others.
- Is the pulsed flux from the Crab pulsar showing some enhanchments at VHEs correlated to possible flares in high-energy γ-rays? This detection would imply the observation of the tail of the synchrotron emission at GeV energies.

A. Appendix

A.1 Units and definitions

Table A.1: SI Metric prefixes

Prefix	Symbol	10^n	Decimal
yotta	Y	10^{24}	1000000000000000000000000
zetta	Z	10^{21}	1000000000000000000000
exa	E	10^{18}	1000000000000000000
peta	P	10^{15}	1000000000000000
tera	T	10^{12}	1000000000000
giga	G	10^{9}	1000000000
mega	M	10^{6}	1000000
kilo	k	10^{3}	1000
hecto	h	10^{2}	100
deca	da	10^{1}	10
		10^{0}	1
deci	d	10^{-1}	0.1
centi	c	10^{-2}	0.01
milli	m	10^{-3}	0.001
micro	⊠	10^{-6}	0.000001
nano	n	10^{-9}	0.000000001
pico	p	10^{-12}	0.000000000001
femto	f	10^{-15}	0.000000000000001
atto	a	10^{-18}	0.000000000000000001
zepto	z	10^{-21}	0.000000000000000000001
yocto	y	10^{-24}	0.000000000000000000000001

Useful definitions

Luminosity: the quantity of energy irradiated per unit time: the irradiated power. If it is defined per unit frequency it is called the *monochromatic* luminosity,

$L(\boxtimes)$. The *bolometric* luminosity is integrated over all frequencies:

$$L = \int_0 \quad L(\boxtimes)\mathrm{d}\boxtimes. \tag{A.1}$$

Flux: the irradiated energy passing a unit surface in a unit time, at a certain distance. For a source with luminosity L at a distance r, the flux is:

$$F = \frac{L}{4\pi r^2}; \quad F(\boxtimes) = \frac{L(\boxtimes)}{4\pi r^2}. \tag{A.2}$$

$F(\boxtimes)$ is called the *monochromatic* flux or *spectral* flux density; it is often measured using a non-SI unit, the Jansky: $1\mathrm{Jy} = 10^{26}\ \mathrm{W\,m\,Hz^{-1}}$

Intensity: the power emitted per unit surface perpendicular to the photon direction, per unit solid angle:

$$I = \frac{\mathrm{d}E}{\mathrm{d}t\,\mathrm{d}\Omega\mathrm{d}A\cos\theta}, \tag{A.3}$$

where θ is the angle between the surface normal and the photon direction. It is a measure of the irradiated energy along a light ray, and does not depend upon the distance. The monochoromatic intensity $I(\boxtimes)$ is the intensity per unit frequency. $I(\boxtimes)/\boxtimes^3$ is a Lorentz invariant quantity.

Emissivity: the power emitted by a unit volume in a unit solid angle:

$$J = \frac{\mathrm{d}E}{\mathrm{d}V\mathrm{d}t\mathrm{d}\Omega}, \tag{A.4}$$

for transparent sources with characteristic dimension R,

$$I = JR \quad \text{(optically thin source)}. \tag{A.5}$$

The spectral emissivity $J(\boxtimes)$ is the emissivity per unit frequency. When calculating quantities per particles, the spectral emissivity of one particle is indicated with $j(\boxtimes)$, and is:

$$j(\boxtimes) = \frac{\mathrm{d}E}{\mathrm{d}t\mathrm{d}\Omega\mathrm{d}\boxtimes} \tag{A.6}$$

Radiative energy density: the energy per unit volume per unit solid angle produced by a source. It can be seen as the energy $\mathrm{d}E$ stored in a volume element of area $\mathrm{d}A$ (perpendicular to the photon direction, $\cos\theta = 1$) and depth $c\mathrm{d}t$, irradiated under a solid angle $\mathrm{d}\Omega$:

$$u(\Omega) = \frac{\mathrm{d}E}{c\mathrm{d}t\mathrm{d}\Omega\mathrm{d}A} = \frac{I}{c} \tag{A.7}$$

Table A.2: SI units

Base units				
Unit name	**Unit symbol**	**Quantity name**	**Quantity symbol**	**Dimension**
metre	m	length	l, x, r	L
kilogram	kg	mass	m	M
second	s	time	t	T
ampere	A	electric current	I	I
kelvin	K	thermodynamic temperature	T	Θ
candela	cd	luminous intensity	I_{v}	J
mole	mol	amount of substance	n	N
Derived units				
radian	rad	angle	θ	-
steradian	sr	solid angle	Ω	-
hertz	Hz	frequency	☒	T^{-1}
joule	J	energy, work, heat	E	$\mathrm{M} \cdot \mathrm{L}^2\,\mathrm{T}^{-2}$
newton	N	force	**F**	$\mathrm{M} \cdot \mathrm{L} \cdot \mathrm{T}^{-2}$
pascal	Pa	pressure, stress	P	$\mathrm{M} \cdot \mathrm{L}^{-1} \cdot \mathrm{T}^{-2}$
watt	W	power, radiant flux	$P, F, ☒_{\mathrm{e}}$	$\mathrm{M} \cdot \mathrm{L}^2 \cdot \mathrm{T}^{-3}$
coulomb	C	electric charge	Q	$\mathrm{T} \cdot \mathrm{I}$
volt	V	voltage, electrical potential difference	$V, ☒_{\mathrm{E}}$	$\mathrm{M} \cdot \mathrm{L}^2 \cdot \mathrm{T}^{-3} \cdot \mathrm{I}^{-1}$
ohm	Ω	electric resistance	R	$\mathrm{M} \cdot \mathrm{L}^2 \cdot \mathrm{T}^{-3} \cdot \mathrm{I}^{-2}$
farad	F	electric capacitance	C	$\mathrm{M}^{-1} \cdot \mathrm{L}^{-2} \cdot \mathrm{T}^4 \cdot \mathrm{I}^2$
siemens	S	electrical conductance	G	$\mathrm{M}^{-1} \cdot \mathrm{L}^{-2} \cdot \mathrm{T}^3 \cdot \mathrm{I}^2$
henry	H	inductance	L	$\mathrm{M} \cdot \mathrm{L}^2 \cdot \mathrm{T}^{-2} \cdot \mathrm{I}^{-2}$
tesla	T	magnetic field strength, magnetic flux density	**B**, **H**	$\mathrm{M} \cdot \mathrm{T}^{-2} \cdot \mathrm{I}^{-1}$
weber	Wb	magnetic flux	$☒_{\mathrm{B}}$	$\mathrm{M} \cdot \mathrm{L}^2 \cdot \mathrm{T}^{-2} \cdot \mathrm{I}^{-1}$
lumen	lm	luminous flux	$☒_{\mathrm{v}}$	J
lux	lx	illuminance	E_{v}	$\mathrm{L}^{-2} \cdot \mathrm{J}$
degree Celsius	°C	temperature	T	Θ
becquerel	Bq	activity	A	T^{-1}
gray	Gy	absorbed dose	D_{T}	$\mathrm{L}^2 \cdot \mathrm{T}^{-2}$
sievert	Sv	equivalent dose	H_{T}	$\mathrm{L}^2 \cdot \mathrm{T}^{-2}$

A.2 Selection of Blazar detection candidates

This section contains ancillary information regarding the source selection selection process explained in §4.1.

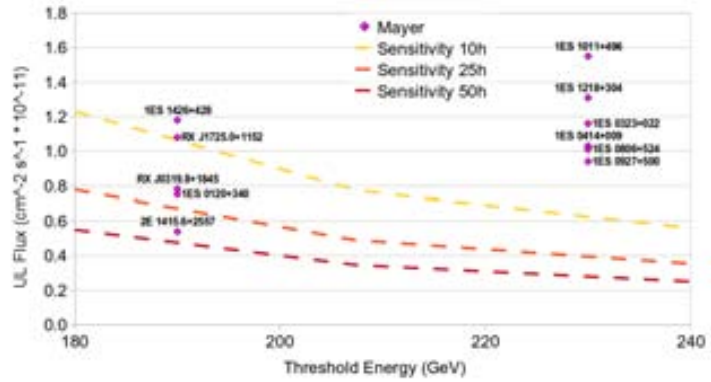

(a) The "Mayer" catalog sources, from Albert et al. (2008b)

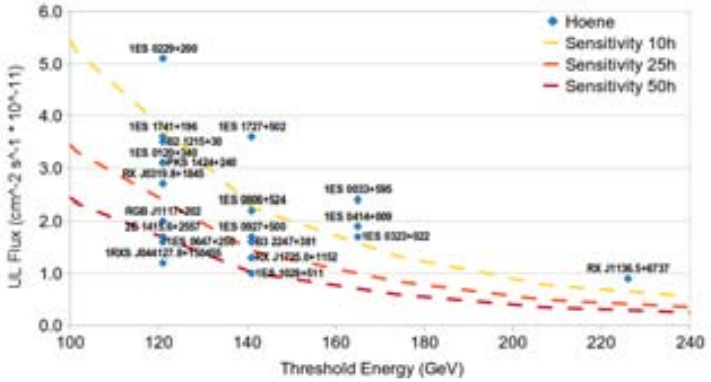

(b) The "HHnne" catalog sources, from Aleksi et al. (2011a)

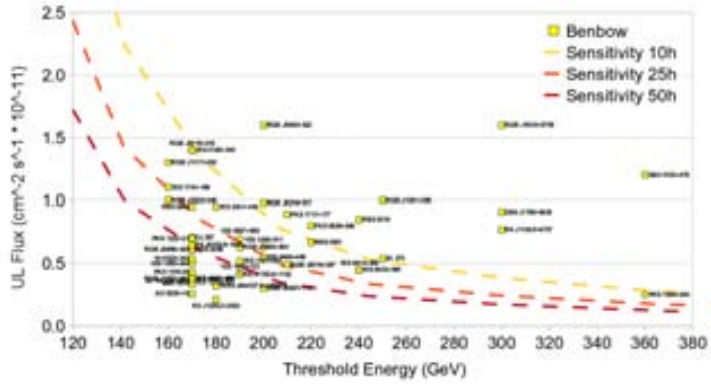

(c) The "Benbow" catalog sources, from Benbow (2009)

Figure A.1
VHE Upper limits for sources from the three catalogs, compared to the preliminary MAGIC stereo sensitivity for 10, 25 and 50 hours of observation time.

Defined as the minimum flux above a given threshold energy necessary to have $N_{\mathrm{exc}}/\sqrt{N_{\mathrm{bkg}}} > 5$ in a given observation time, for a point-like source (N_{exc} is the number of excess events, N_{bkg} that of background events).

Table A.4: List of sources selected for the VHE detection of a Blazar, see §4.1 Fluxes for the Fermi-LAT 1FLG Ca
100 MeV and are given in units of 10^{-5} ph m s^{-1}. Thresholds (Thr.) for the VHE catalogs are given in GeV; upper lim
for the "HHhne" (Aleksi et al., 2011a) and the "Mayer" catalogs, and of 10^{-8} ph m s^{-1} for the "Benbow" catalog (B
detected, references to are given as footnotes.

Source Name	Position		Redshift	Fermi 1FGL		HHhne	
	Right Ascension	Declination		Idx	Flux	Thr.	
RBS 0042	00h18m27.7s	+29d47m30s	0.100	1.4845	0.16	-	
1ES 0033+595	00h35m52.644s	+59d50m04.59s	0.086	1.9475	2.74	165	2
RGB J0110+418	01h10m04.789s	+41d49m50.89s	0.096	-	-	-	
1ES 0120+340	01h23m08.637s	+34d20m48.66s	0.272	-	-	121	3
QSO 0133+476	01h36m58.6s	+47d51m29s	0.859	2.3437	20.89	-	
RGB J0214+517	02h14m17.9342s	+51d44m51.945s	0.049	-	-	-	
RBS 0298	02h16m32.1s	+23d14m47s	0.289	-	-	-	
RBS 0319	02h27m16.6s	+02d02m00s	0.457	-	-	-	
1ES 0229+200	02h32m48.616s	+20d17m17.45s	0.140	-	-	121	5
AO 0235+16	02h38m38.9301s	+16d36m59.275s	0.940	2.1433	42.69	-	
RGB J0314+247	03h14m02.74s	+24d44m33.1s	0.054	-	-	-	
RX J0319.8+1845	03h19m51.800s	+18d45m34.40s	0.190	1.4653	0.33	121	2
1H 0323+342	03h24m41.1613s	+34d10m45.856s	0.061	2.6959	5.11	-	
1ES 0323+022	03h26m13.946s	+02d25m14.77s	0.147	2.1363	1.59	165	1
1ES 0414+009	04h16m52.490s	+01d05m23.90s	0.287	1.9425	0.66	165	1
1RXS J044127.8+150455	04h41m27.4s	+15d04m55s	0.109	-	-	121	1
1ES 0446+449	04h50m07.2s	+45d03m12s	0.203	-	-	-	
RGB J0643+422	06h43m26.750s	+42d14m18.70s	0.080	-	-	-	
1ES 0647+250	06h50m46.490s	+25d02m59.60s	0.203	2.0362	2.02	121	1
RGB J0656+426	06h56m10.6629s	+42d37m02.751s	0.059	-	-	-	
1ES 0806+524	08h09m49.1870s	+52d18m58.252s	0.138	2.0954	2.44	141	2
PKS 0829+046	08h31m48.8769s	+04d29m39.086s	0.174	2.4967	7.28	-	
Mkn 1218	08h38m10.9s	+24d53m43s	0.028	-	-	-	
RGB J0847+115	08h47m12.931s	+11d33m50.25s	0.199	1.3959	0.21	-	
OJ 287	08h54m48.9s	+20d06m31s	0.306	2.3833	6.97	-	
1ES 0927+500	09h30m37.590s	+49d50m25.55s	0.188	-	-	141	1
1ES 1011+496	10h15m04.1398s	+49d26m00.704s	0.212	1.9336	6.74	-	
1ES 1028+511	10h31m18.518s	+50d53m35.82s	0.361	1.7782	0.60	141	1
RGB J1053+494	10h53m44.130s	+49d29m55.99s	0.140	1.6278	0.51	-	
RBS 0921	10h56m06.606s	+02d52m13.50s	0.236	-	-	-	
RGB J1117+202	11h17m06.260s	+20d14m07.40s	0.139	1.7065	1.12	121	2
RX J1136.5+6737	11h36m30.079s	+67d37m04.39s	0.134	1.7977	0.36	226	0
1ES 1215+303	12h17m52.0819s	+30d07m00.636s	0.130	1.9782	5.82	-	
B2 1215+30	12h17m52.0819s	+30d07m00.636s	0.130	1.9782	5.82	121	3
1ES 1218+304	12h21m21.941s	+30d10m37.11s	0.184	1.6996	1.68	-	
PKS 1222+21	12h24m54.4583s	+21d22m46.388s	0.432	2.5472	7.89	-	
3C 273	12h29m06.6997s	+02d03m08.598s	0.158	2.7477	54.73	-	
1ES 1255+244	12h57m31.939s	+24d12m40.23s	0.141	-	-	-	
RX J1326.2+2933	13h26m14.95s	+29d33m31.6s	0.431	-	-	-	
RGB J1341+399	13h41m04.920s	+39d59m35.16s	0.163	2.4483	1.36	-	
7C 1415+2556	14h17m56.7s	+25d43m26s	0.237	2.1230	1.04	121	1
PKS 1424+240	14h27m00.3917s	+23d48m00.037s	0.160	1.8298	7.23	121	3
1ES 1426+428	14h28m32.660s	+42d40m20.60s	0.129	1.4922	0.33	-	
1ES 1440+122	14h42m48.280s	+12d00m40.30s	0.162	1.7691	0.49	-	
PKS 1510-089	15h12m50.5329s	-09d05m59.828s	0.360	2.4076	131.90	-	
RGB J1532+302	15h32m02.241s	+30d16m28.96s	0.064	1.7771	0.24	-	

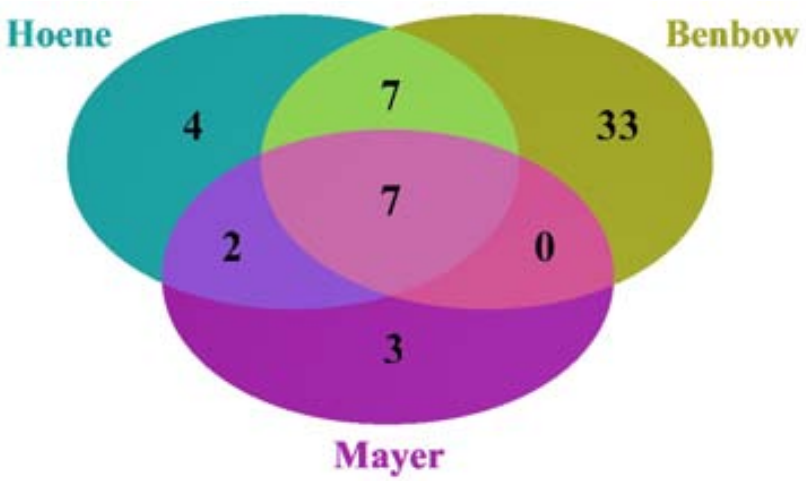

Figure A.2
Venn diagram illustrating the overlap between the three candidate source catalogues listed in table A.4.

List of Abbreviations

1FGL	First Fermi Gamma-ray LAT source catalog Abdo et al. (2010)
2FGL	Second Fermi Gamma-ray LAT source catalog Nolan et al. (2012)
a.s.l.	above sea level
AGILE	Astro-rivelatore Gamma a Immagini LEggero, a gamma-ray satellite
BAT	Burst Alert Telescope on-board *Swi* (Barthelmy et al., 2005)
BH	Black Hole
BLR	Broad Line Region
CBR	Cosmic Background Radiation
CGB	Cosmic Gamma-ray Background radiation: emitted by unresolved extragalactic sources and result from the interactions between cosmic rays and the interstellar medium
CIB	Cosmic Infrared Background radiation: thermal re-emission of starlight by dust.
CMB	Cosmic Microwave Background radiation: redshifted relic radiation from the surface of last scattering, at the decoupling epoch of $z = 1090.88 \pm 0.72$ (**?**).
COB	Cosmic Optical Background radiation: emitted by stars located nearby (Zodiacal light) and at cosmological distances
COBE	COsmic Background Explorer, a satellite for infrared background measurements
CORSIKA	COsmic Ray SImulations for KASCADE
CRB	Cosmic Radio Background radiation

CXB	Cosmic X-ray Background radiation: emitted by nearby hot gas and unresolved galactic and extragalactic sources
Dec.	Declination, a sky coordinate
DIRBE	Diffuse Infrared Background Experiment, an instrument onboard the COBE satellite
EBL	Extragalactic Background Light, the ultraviolet to infrared part of the CBR relevant for VHE γ-ray absorption
EBL	Extragalactic Background Light
EIC	External Inverse Compton models of γ-ray emission from blazars
EM	ElectroMagnetic
Fermi-LAT	Large Area Telescope onboard the Fermi Gamma-Ray Space Telescope
FGST	Fermi Gamma-Ray Space Telescope
Fig.	Figure
FIRAS	The Far Infrared Absolute Spectrophotometer, an instrument onboard the COBE satellite
FSRQ	Flat Spectrum Radio Quasar
FSSC	Fermi Science Support Center
FWHM	Full Width Half Maximum
GBM	Gamma-ray Burst Monitor, an instrument onboard the Fermi Gamma-Ray Space Telescope
GRB	Gamma Ray Burst
GRID	Gamma Ray Imaging Detector, an instrument aboard the satellite AGILE
HBL	High-energy peaked BL Lac object
HE	High Energy, $E > 10$ MeV
HEASARC	High Energy Astrophysics Science Archive Research Center hosts NASA's and other space agencies high-energy mission data and tools
HEASoft	High Energy Astrophysics Software package distributed by HEASARC (NASA, 2012b)

IACT	Imaging Atmospheric Cherenkov Technique, or Telescope
IBL	Intermediate-energy peaked BL Lac object
IBL	Intermediate-peaked BL-Lac object
INTEGRAL	INTernational Gamma-Ray Astrophysics Laboratory
IRF	Instrument Response Function
IRTS	InfraRed Telescope Satellite
KASCADE	KArlsruhe Shower Core and Array DEtector (Antoni et al., 2003)
LAT	Large Area Telescope, see Fermi-LAT
LBL	Low-peaked BL-Lac object
NASA	National Air and Space Administration of the United States of America
NIRS	Near Infrared Spectrometer on board IRTS
NKG	Nishimura-Kamata-Greisen formula for lateral distribution of electrons in an electromagnetic shower
NLR	Narrow Line Region
OP	Off-Peak region in the Crab Pulsar light curve
P1	The highest peak in the radio folded light curve of the Crab pulsar
P1	The secondary peak in the radio folded light curve of the Crab pulsar
phe	photo-electrons
PWN	Pulsar Wind Nebula
R.A.	Right Angle, a sky coordinate
RF	Random Forest
RMS	Root Mean Square
ROSAT	ROentgen SATellite, an X-ray satellite operative between 1990 and 1999.
SED	Spectral Energy Distribution
SED	Spectral Energy Distribution

SMBH	Super Massive Black Hole
SN	SuperNova
SNR	SuperNova Remnant
Soft γ-rays	Gamma rays with energies up to ~ 10 MeV
SSC	Self Synchrotron Compton models of γ-ray emission from blazars
SSC	Synchrotron-Self-Compton
SSRQ	Steep Spectrum Radio Quasars
ToO	Target of Opportunity
TP	Union of the peak regions of the Crab pulsar light curve: P1 P2 = TP
UHE	Ultra High Energies, with energies $E > 10^{18}$
UVOT	Ultra-Violet/Optical Telescope on-board *Swi* (Roming et al., 2005)
VHE	Very High Energy, $E > 100GeV$
XRT	X-Ray Telescope on-board *Swi* (Burrows et al., 2005)
XSPEC	X-ray SPECtral fitting program, part of HEASoft.

List of Tables

List of Figures

References

Abbasi, R. et al. (2010a). Measurement of the anisotropy of cosmic-ray arrival directions with IceCube. *e Astrophysical Journal*, 718(2):L194–L198.

Abbasi, R. U. et al. (2005). A study of the composition of Ultra-High-Energy cosmic rays using the High-Resolution fly's eye. *e Astrophysical Journal*, 622(2):910–926.

Abbasi, R. U. et al. (2010b). Indications of Proton-Dominated Cosmic-Ray composition above 1.6 EeV. *Physical Review Letters*, 104(16):161101.

Abdo, A. A. et al. (2009a). Measurement of the cosmic ray $e^+ + e^-$ spectrum from 20 GeV to 1 TeV with the Fermi Large Area Telescope. *Physical Review Letters*, 102(18):181101.

Abdo, A. A. et al. (2009b). The large-scale cosmic-ray anisotropy as observed with MILAGRO. *e Astrophysical Journal*, 698(2):2121–2130.

Abdo, A. A. et al. (2010). FERMI LARGE AREA TELESCOPE FIRST SOURCE CATALOG. *e Astrophysical Journal Supplement Series*, 188(2):405–436.

Abdo, A. A. et al. (2010). Fermi Large Area Telescope Observations of the Crab Pulsar And Nebula. *e Astrophysical Journal*, 708:1254–1267.

Abdo, A. A. et al. (2010). The first catalog of active galactic nuclei detected by the fermi large area telescope. *e Astrophysical Journal*, 715:429–457.

Abdo, A. A. et al. (2010). The First Fermi Large Area Telescope Catalog of Gamma-ray Pulsars. *e Astrophysical Journal Supplement Series*, 187:460–494.

Abdo, A. A. et al. (2011). Fermi large area telescope observations of markarian 421: The missing piece of its spectral energy distribution. *e Astrophysical Journal*, 736:131.

Abraham, J. et al. (2004). Properties and performance of the prototype instrument for the pierre auger observatory. *Nuclear Instruments and Methods in Physics A*, 523(1):50–95.

Abreu, P. et al. (2011). The pierre auger observatory i: The cosmic ray energy spectrum and related measurements. *arXiv*:□□□□□□□□.

Ackermann, M. et al. (2011). THE SECOND CATALOG OF ACTIVE GALACTIC NUCLEI DETECTED BY THE FERMI LARGE AREA TELESCOPE. □ *e Astrophysical Journal*, 743(2):171.

Adriani, O. et al. (2009a). An anomalous positron abundance in cosmic rays with energies 1.5-100 GeV. *Nature*, 458(7238):607□609.

Adriani, O. et al. (2009b). New measurement of the antiproton-to-proton flux ratio up to 100 GeV in the cosmic radiation. *Physical Review Letters*, 102(5):051101.

Aharonian, F. et al. (2008). Energy spectrum of cosmic-ray electrons at TeV energies. *Physical Review Letters*, 101(26):261104.

Aharonian, F. et al. (2009). Simultaneous observations of PKS 2155-304 with HESS, fermi, RXTE, and atom: Spectral energy distributions and variability in a low state. □ *e Astrophysical Journal Letters*, 696:L150□L155.

Aharonian, F. A. and Bogovalov, S. V. (2003). Exploring physics of rotation powered pulsars with sub-10 GeV imaging atmospheric Cherenkov telescopes. *New Astronomy*, 8:85□103.

Aharonian, F. A., Bogovalov, S. V., and Khangulyan, D. (2012). Abrupt acceleration of a □old' ultrarelativistic wind from the Crab pulsar. *Nature*, 482:507□509.

Albert, J. et al. (2007). Unfolding of differential energy spectra in the MAGIC experiment. *Nuclear Instruments and Methods in Physics Research A*, 583:494□506.

Albert, J. et al. (2008a). Implementation of the random forest method for the imaging atmospheric cherenkov telescope MAGIC. *Nuclear Instruments and Methods in Physics Research A*, 588:424□432.

Albert, J. et al. (2008b). Systematic search for VHE Gamma-Ray emission from X-Ray□bright High-Frequency BL lac objects. □ *e Astrophysical Journal*, 681(2):944□ 953.

Aleksi□, J. et al. (2011). Observations of the Crab Pulsar between 25 and 100 GeV with the MAGIC I Telescope. □ *e Astrophysical Journal*, 742:43.

Aleksi□, J. et al. (2010). MAGIC TeV gamma-ray observations of markarian 421 during multiwavelength campaigns in 2006. *Astronomy and Astrophysics*, 519:A32.

Aleksi□, J. et al. (2011a). Gamma-ray excess from a stacked sample of high- and intermediate-frequency peaked blazars observed with the MAGIC telescope. □ *e Astrophysical Journal*, 729:115.

Aleksi, J. et al. (2011b). MAGIC observations and multiwavelength properties of the quasar 3C 279 in 2007 and 2009. *Astronomy and Astrophysics*, 530:4.

Aleksi, J. et al. (2012). Performance of the MAGIC stereo system obtained with crab nebula data. *Astroparticle Physics*, 35(7):435448.

Alexeyev, E., Alexeyeva, L., Krivosheina, I., and Volchenko, V. (1988). Detection of the neutrino signal from SN 1987A in the LMC using the INR baksan underground scintillation telescope. *Physics Letters B*, 205(23):209214.

Aliu, E. et al. (2008). Observation of Pulsed Gamma-rays Above 25 GeV from the Crab Pulsar with MAGIC. *Science*, 322:1221.

Aliu, E. et al. (2009). Improving the performance of the single-dish cherenkov telescope MAGIC through the use of signal timing. *Astroparticle Physics*, 30(6):293 305.

Aliu, E. et al. (2011). Detection of Pulsed Gamma Rays Above 100 GeV from the Crab Pulsar. *Science*, 334:69.

Alloin, D., Johnson, R., and Lira, P., editors (2006). *Physics of Active Galactic Nuclei at all Scales*. Springer, 1 edition.

Amenomori, M. et al. (2011). Cosmic-ray energy spectrum around the knee obtained by the tibet experiment and future prospects. *Advances in Space Research*, 47(4):629639.

Anderson, C. D. (1933). The positive electron. *Phys. Rev.*, 43:491494.

Anderson, C. D. and Neddermeyer, S. H. (1936). Cloud chamber observations of cosmic rays at 4300 meters elevation and near sea-level. *Physical Review*, 50(4):263 271.

Antoni, T. et al. (2003). The cosmic-ray experiment KASCADE. *Nuclear Instruments and Methods in Physics Research Section A: Accelerators, Spectrometers, Detectors and Associated Equipment*, 513(3):490510.

Antoni, T. et al. (2005). KASCADE measurements of energy spectra for elemental groups of cosmic rays: Results and open problems. *Astroparticle Physics*, 24(12):125.

Antonucci, R. (1993). Unified models for active galactic nucle and quasars. *Annual Review of Astronomy and Astrophysics*, 31(1):473521.

Ant n, S. and Browne, I. W. A. (2005). The recognition of blazars and the blazar spectral sequence. *Monthly Notices of the Royal Astronomical Society*, 356(1):225231.

Apel, W. D. et al. (2009). Energy spectra of elemental groups of cosmic rays: Update on the KASCADE unfolding analysis. *Astroparticle Physics*, 31(2):8691.

Arnett, D. (1996). *Supernovae and Nucleosynthesis*. Princeton University Press.

Arons, J. and Scharlemann, E. (1979). Pair formation above pulsar polar caps- Structure of the low altitude acceleration zone. *Astrophysical Journal*, 231(Part 1).

Atwood, W. B. et al. (2009a). The large area telescope on the fermi gamma-ray space telescope mission. *The Astrophysical Journal*, 697:1071–1102.

Atwood, W. B. et al. (2009b). The Large Area Telescope on the Fermi Gamma-ray Space Telescope Mission. astro-ph/0902.1089.

Auger, P., Maze, R., and Grivet-Meyer, T. (1938). Grandes gerbes cosmiques atmosph"riques contenant des corpuscules ultra-p"n"trantes. *CR Acad. Sci*, 206:1721–1722.

Axford, W. I., Leer, E., and Skadron, G. (1977). The acceleration of cosmic rays by shock waves. In *Proceedings of the International Conference th Cosmic Ray Conference*, volume 11, pages 132–137, Plovdiv, Bulgaria. B'lgarska Akademiia na Naukite.

Baade, W. and Zwicky, F. (1934a). On super-novae. *Proceedings of the National Academy of Sciences of the United States of America*, 20(5):254–259. PMID: 16587881 PMCID: PMC1076395.

Baade, W. and Zwicky, F. (1934b). Remarks on super-novae and cosmic rays. *Physical Review*, 46(1):76–77.

Ballard, K. R. and Heavens, A. F. (1992). Shock acceleration and steep-spectrum synchrotron sources. *Monthly Notices of the Royal Astronomical Society*, 259:89–94.

Barnes, J. E. and Hernquist, L. E. (1991). Fueling starburst galaxies with gas-rich mergers. *The Astrophysical Journal Letters*, 370:L65–L68.

Barthelmy, S. D., Barbier, L. M., Cummings, J. R., Fenimore, E. E., Gehrels, N., Hullinger, D., Krimm, H. A., Markwardt, C. B., Palmer, D. M., Parsons, A., et al. (2005). The burst alert telescope (BAT) on the SWIFT midex mission. *Space Science Reviews*, 120(3):143–164.

Bauleo, P. M. and Martino, J. R. (2009). The dawn of the particle astronomy era in ultra-high-energy cosmic rays. *Nature*, 458(7240):847–851.

Becker, R. H., White, R. L., and Edwards, A. L. (1991). A new catalog of 53,522 4.85 GHz sources. *The Astrophysical Journal Supplement Series*, 75:1–229.

Bednarek, W. (2012). On the origin of sub-TeV gamma-ray pulsed emission from rotating neutron stars. *Monthly Notices of the Royal Astronomical Society*, 424(3):2079–2085.

Bednarek, W. and Protheroe, R. J. (1999). Gamma-ray and neutrino flares produced by protons accelerated on an accretion disc surface in active galactic nuclei. *Monthly Notices of the Royal Astronomical Society*, 302(2):373–380.

Bell, A. R. (1978). The acceleration of cosmic rays in shock fronts. i. *Monthly Notices of the Royal Astronomical Society*, 182:147–156.

Benbow, W. (2009). The VERITAS blazar key science project. *arXiv:????.????*. for the VERITAS collaboration.

Benford, G. and Buschauer, R. (1977). Coherent pulsar radio radiation by antenna mechanisms - general theory. *Monthly Notices of the Royal Astronomical Society*, 179:189–207.

Berdyugin, A., Ciprini, S., Halkola, A., Hovatta, T., Kadenius, V., Lindfors, E., Nilsson, K., Nurmi, P., Ostorero, L., Pasanen, M., Reinthal, R., Saarinen, J., Sainio, J., Takalo, L. O., Tuominen, C., Villforth, C., and Vornanen, T. (2012). Optical r-band lightcurves of selected blazars. http://users.utu.fi/kani/1m/B3_2247+381.html.

Berezhko, E. (1996). Maximum energy of cosmic rays accelerated by supernova shocks. *Astroparticle Physics*, 5(3–4):367–378.

Beringer, J. et al. (2012). The review of particle physics. *Physical Review*, 010001(D86).

Bethe, H. and Heitler, W. (1934). On the stopping of fast particles and on the creation of positive electrons. *Proceedings of the Royal Society of London. Series A, Containing Papers of a Mathematical and Physical Character*, 146(856):83–112.

Bethe, H. A. (1953). Molière's theory of multiple scattering. *Physical Review*, 89(6):1256–1266.

Biermann, P. L., Chirvasa, M., Falcke, H., Markof, S., and Zier, C. (2002). Single and binary black holes and their active environment. *arXiv:astro-ph/??????*.

Bionta, R. M. et al. (1987). Observation of a neutrino burst in coincidence with supernova 1987A in the large magellanic cloud. *Physical Review Letters*, 58(14):1494–1496.

Blackett, P. M. S. and Occhialini, G. P. S. (1933). Some photographs of the tracks of penetrating radiation. *Proceedings of the Royal Society of London. Series A*, 139(839):699–726.

Blandford, R. D. and KHnigl, A. (1979). Relativistic jets as compact radio sources. *e Astrophysical Journal*, 232:34–48.

Blandford, R. D. and Ostriker, J. P. (1978). Particle acceleration by astrophysical shocks. *e Astrophysical Journal Letters*, 221:L29–L32.

Blandford, R. D. and Payne, D. G. (1982). Hydromagnetic flows from accretion discs and the production of radio jets. *Monthly Notices of the Royal Astronomical Society*, 199:883–903.

Blandford, R. D. and Rees, M. J. (1974). A 'twin-exhaust' model for double radio sources. *Monthly Notices of the Royal Astronomical Society*, 169:395–415.

Blandford, R. D. and Znajek, R. L. (1977). Electromagnetic extraction of energy from kerr black holes. *Monthly Notices of the Royal Astronomical Society*, 179:433–456.

Blumenthal, G. R. and Gould, R. J. (1970). Bremsstrahlung, Synchrotron Radiation, and Compton Scattering of High-Energy Electrons Traversing Dilute Gases. *Reviews of Modern Physics*, 42(2):237–270.

BlXmer, J., Engel, R., and HHrandel, J. R. (2009). Cosmic rays from the knee to the highest energies. *Progress in Particle and Nuclear Physics*, 63(2):293–338.

Boettcher, M., Harris, D. E., and Krawczynski, H. (2011). *Relativistic Jets from Active Galactic Nuclei*. John Wiley & Sons.

Boggess, N. W. et al. (1992). The COBE mission - its design and performance two years after launch. *e Astrophysical Journal*, 397:420–429.

Borla Tridon, D. (2011). *A Study of Cosmic Electrons between GeV and TeV with the MAGIC Telescopes*. PhD thesis, Technische Universit" t MXnchen, MXnchen.

Bothe, W. and KolhHrster, W. (1929). Das wesen der hHhenstrahlung. *Zeitschri fXr Physik A Hadrons and Nuclei*, 56(11):751–777.

Brinkmann, W., Siebert, J., Feigelson, E. D., Kollgaard, R. I., Laurent-Muehleisen, S. A., Reich, W., Fuerst, E., Reich, P., Voges, W., Truemper, J., and McMahon, R. (1997). Radio-loud active galaxies in the northern ROSAT all-sky survey. II. multi-frequency properties of unidentified sources. *Astronomy and Astrophysics*, 323:739–748.

Browning, R., Ramsden, D., and Wright, P. (1971). Detection of pulsed gamma radiation from the Crab Nebula(Pulsed gamma radiation detection from Crab Nebula by balloon-borne telescope). *Nature Physical Science*, 232:99–101.

Burrows, D. et al. (2005). The *Swi* x-ray telescope. *Space Science Reviews*, 120(3):165–195.

Busca, N., Hooper, D., and Kolb, E. W. (2006). Pierre auger data, photons, and top-down cosmic ray models. *Physical Review D*, 73(12):123001.

BHttcher, M., Reimer, A., and Marscher, A. P. (2009). IMPLICATIONS OF THE VERY HIGH ENERGY GAMMA-RAY DETECTION OF THE QUASAR 3C279. *e Astrophysical Journal*, 703(1):1168–1175.

Caccianiga, A. and March•, M. J. M. (2004). The CLASS blazar survey: testing the blazar sequence. *Monthly Notices of the Royal Astronomical Society*, 348(3):937–954.

Carlson, J. F. and Oppenheimer, J. R. (1937). On multiplicative showers. *Physical Review*, 51(4):220–231.

Carruthers, P. and Duong-Van, M. (1972). New scaling law based on the hydrodynamical model of particle production. *Physics Letters B*, 41(5):597–601.

Castellina, A. and Donato, F. (2011). Astrophysics of Galactic charged cosmic rays. *ArXiv e-prints*.

Celotti, A., Ghisellini, G., and Chiaberge, M. (2001). Large-scale jets in active galactic nuclei: multiwavelength mapping. *Monthly Notices of the Royal Astronomical Society*, 321(1):L1–L5.

Chandrasekhar, S. (1931a). The highly collapsed configurations of a stellar mass. *Monthly Notices of the Royal Astronomical Society*, 91:456–466.

Chandrasekhar, S. (1931b). The maximum mass of ideal white dwarfs. *e Astrophysical Journal*, 74:81.

Chandrasekhar, S. (1931c). XLVIII. the density of white dwarf stars. *e London, Edinburgh, and Dublin Philosophical Magazine and Journal of Science*, 11(70):592–596.

Chen, P., Fu, H., and Gao, Y. (2005). 2MASS observation of BL lac objects. *New Astronomy*, 11(1):27–42.

Cheng, K., Ho, C., and Ruderman, M. (1986). Energetic radiation from rapidly spinning pulsars. I- Outer magnetosphere gaps. II- VELA and Crab. *Astrophysical Journal*, 300(Part 1).

Cherenkov, P. (1934). Visible emission of clean liquids by action of γradiation. *Doklady Akademii Nauk SSSR*, 2:451.

Chugunov, I. V., Eidman, V. I., and Suvorov, E. V. (1975). The motion of charged particles in a strong electromagnetic field and curvature radiation. *apss*, 32:L7–L10.

Cocke, W., Disney, M., and Taylor, D. (1969). Discovery of optical signals from pulsar NP 0532. *Nature*, 221:525.

Collaboration, T. F.-L. (2010). Gamma-ray emission concurrent with the nova in the symbiotic binary v407 cygni. *Science*, 329(5993):817–821.

de Jager, O. C., Raubenheimer, B. C., and Swanepoel, J. W. H. (1989). A poweful test for weak periodic signals with unknown light curve shape in sparse data. *Astronomy and Astrophysics*, 221:180–190.

Dermer, C. D. (2012). Sources of GeV photons and the fermi results. *arXiv*:□□□□.□□□□.

Dole, H., Lagache, G., Puget, J. L., Caputi, K. I., Fernandez-Conde, N., Le Floc'h, E., Papovich, C., Perez-Gonzalez, P. G., Rieke, G. H., and Blaylock, M. (2006). The cosmic infrared background resolved by spitzer. *Astronomy and Astrophysics*, 451(2):417□429.

Dom¯nguez, A. et al. (2011). Extragalactic background light inferred from AEGIS galaxy-SED-type fractions. *Monthly Notices of the Royal Astronomical Society*, 410:2556□2578.

Donato, D., Ghisellini, G., Tagliaferri, G., and Fossati, G. (2001). Hard x-ray properties of blazars. *Astronomy and Astrophysics*, 375:739□751.

Dondi, L. and Ghisellini, G. (1995). Gamma-ray-loud blazars and beaming. *Monthly Notices of the Royal Astronomical Society*, 273:583□595.

Du, Y. J., Qiao, G. J., and Wang, W. (2012). Radio-to-TeV Phase-resolved Emission from the Crab Pulsar: The Annular Gap Model. □ *e Astrophysical Journal*, 748:84.

Engel, R., Heck, D., and Pierog, T. (2011). Extensive air showers and hadronic interactions at high energy. *Annual Review of Nuclear and Particle Science*, 61(1):467□489.

Falco, E. E., Kochanek, C. S., and Munoz, J. A. (1998). Limits on cosmological models from radio-selected gravitational lenses. □ *e Astrophysical Journal*, 494(1):47□59.

Fan, Y.-Z., Zhang, B., and Chang, J. (2010). ELECTRON/POSITRON EXCESSES IN THE COSMIC RAY SPECTRUM AND POSSIBLE INTERPRETATIONS. *International Journal of Modern Physics D*, 19(13):2011□2058.

Fanaroff, B. L. and Riley, J. M. (1974). The morphology of extragalactic radio sources of high and low luminosity. *Monthly Notices of the Royal Astronomical Society*, 167:31P□36P.

Fermi, E. (1949). On the origin of the cosmic radiation. *Physical Review*, 75(8):1169.

Ficarra, A., Grueff, G., and Tomassetti, G. (1985). A new bologna sky survey at 408 MHz. *Astronomy and Astrophysics Supplement Series*, 59:255□347.

Fierro, J., Michelson, P., Nolan, P., and Thompson, D. (1998). Phase-resolved studies of the high-energy gamma-ray emission from the Crab, Geminga, and Vela pulsars. □ *e Astrophysical Journal*, 494(2):734□746.

Floyd, F., Glass, I., and Schnopper, H. (1969). Hard X-Rays from the Crab Pulsar. *Nature*, 224:50□51.

Fossati, G., Maraschi, L., Celotti, A., Comastri, A., and Ghisellini, G. (1998). A unifying view of the spectral energy distributions of blazars. *Monthly Notices of the Royal Astronomical Society*, 299(2):433–448.

Franceschini, A., Rodighiero, G., and Vaccari, M. (2008). Extragalactic optical-infrared background radiation, its time evolution and the cosmic photon-photon opacity. *Astronomy and Astrophysics*, 487(3):837–852.

Frank, I. and Tamm, I. (1937). Coherent visible radiation of fast electrons passing through matter. *Dokl. Akad. Nauk SSSR*, 14:109–114.

Fritz, G., Henry, R., Meekins, J., Chubb, T., and Friedman, H. (1969). X-ray Pulsar in the Crab Nebula. *Science*, 164(3880):709–712.

Gaisser, T. K. (1990). *Cosmic Rays and Particle Physics*. Cambridge University Press.

Gaisser, T. K. (2006). The cosmic-ray spectrum: from the knee to the ankle. *Journal of Physics: Conference Series*, 47:15–20.

Garcia-MuGoz, M., Mason, G. M., and Simpson, J. A. (1975). The cosmic-ray age deduced from the Be-10 abundance. *e Astrophysical Journal Letters*, 201:L141–L144.

Garcia-Munoz, M., Simpson, J. A., Guzik, T. G., Wefel, J. P., and Margolis, S. H. (1987). Cosmic-ray propagation in the galaxy and in the heliosphere - the path-length distribution at low energy. *e Astrophysical Journal Supplement Series*, 64:269–304.

Gehrels, N. et al. (2004). The swift Gamma-Ray burst mission. *e Astrophysical Journal*, 611(2):1005–1020.

Gehrels, N. and Michelson, P. (1999). GLAST: the next-generation high energy gamma-ray astronomy mission. *Astroparticle Physics*, 11:277–282.

Ghisellini, G. (2012). Radiative Processes in High Energy Astrophysics. *arXiv*:....

Ghisellini, G., Celotti, A., Fossati, G., Maraschi, L., and Comastri, A. (1998). A theoretical unifying scheme for gamma-ray bright blazars. *Monthly Notices of the Royal Astronomical Society*, 301(2):451–468.

Gilmore, R., Somerville, R., Primack, J., and Dom¯nguez, A. (2012). Gamma-ray spectra and the extragalactic background light. *Journal of Physics: Conference Series*, 355:012026.

Gilmore, R. C., Madau, P., Primack, J. R., Somerville, R. S., and Haardt, F. (2009). GeV gamma-ray attenuation and the high-redshift UV background. *Monthly Notices of the Royal Astronomical Society*, 399(4):1694–1708.

Ginzburg, V. L. and Syrovatskii, S. I. (1964). *The Origin of Cosmic Rays*. Pergamon Press.

Gold, T. (1968). Rotating neutron stars as the origin of the pulsating radio sources. *Nature*, 218(5143):731–732.

Goldreich, P. and Julian, W. H. (1969). Pulsar Electrodynamics. *Astrophysical Journal*, 157:869–880.

Green, D. A. (2004). Galactic supernova remnants: an updated catalogue and some statistics. *Bulletin of the Astronomical Society of India*, 32:335–370.

Gregory, P. C. and Condon, J. J. (1991). The 87GB catalog of radio sources covering delta between o and + 75 deg at 4.85 GHz. *The Astrophysical Journal Supplement Series*, 75:1011–1291.

Greisen, K. (1966). End to the cosmic-ray spectrum? *Physical Review Letters*, 16(17):748–750.

Grenier, I. and Harding, A. (2006). Pulsar twinkling and relativity. In *AIP Conference Proceedings*, volume 861, page 630.

Griffith, M., Langston, G., Heflin, M., Conner, S., Lehar, J., and Burke, B. (1990). The third MIT-Green bank 5 GHz survey. *The Astrophysical Journal Supplement Series*, 74:129–180.

Gunn, J. E. and Ostriker, J. P. (1969). Acceleration of high-energy cosmic rays by pulsars. *Physical Review Letters*, 22(14):728–731.

Gurevich, A., Duncan, L., Karashtin, A., and Zybin, K. (2003). Radio emission of lightning initiation. *Physics Letters A*, 312(3-4):228–237.

Haardt, F. and Maraschi, L. (1991). A two-phase model for the x-ray emission from seyfert galaxies. *The Astrophysical Journal Letters*, 380:L51–L54.

Hanlon, W. F. (2012). Updated cosmic ray spectrum. http://www.physics.utah.edu/~whanlon/spectrum.html. Retrieved on 2012-05-25.

Harding, A. (1981). Pulsar gamma-rays- Spectra, luminosities, and efficiencies. *Astrophysical Journal*, 245(Part 1).

Harding, A. (2000). Gamma-ray pulsars: models and predictions. *Arxiv preprint astro-ph/0010632*.

Harding, A. and Muslimov, A. (2002). Pulsar Polar Cap Heating and Surface Thermal X-Ray Emission. II. Inverse Compton Radiation Pair Fronts. *The Astrophysical Journal*, 568(2):862–877.

Hauser, M. G. and Dwek, E. (2001). The Cosmic Infrared Background: Measurements and Implications. *Annual Review of Astronomy and Astrophysics*, 39(1):249–307.

Heck, D., Knapp, J., Capdevielle, J., Shatz, G., and Thouw, T. (1998). CORSIKA: a monte carlo code to simulate extensive air showers. Wissenschaftliche Bericht FZKA6019, Forschungszentrum Karslruhe GmbH, Karslruhe.

Heitler, W. (1954). *The Quantum Theory of Radiation: Third Edition*. Courier Dover Publications.

Helene, O. (1983). Upper limit of peak area. *Nuclear Instruments and Methods in Physics Research*, 212(1–3):319–322.

Hess, V. F. (1912). Über Beobachtungen der durchdringenden Strahlung bei sieben Freiballonfahrten. *Physikalische Zeitschrift*, 13:1084–91.

Hess, V. F. (1913). Über den ursprung der durchdringenden strahlung. *Physikalische Zeitschrift*, 14:610.

Hillas, A. M. (1984). The origin of ultra-high-energy cosmic rays. *Annual Review of Astronomy and Astrophysics*, 22:425–444.

Hillas, A. M. (1985). Cerenkov light images of EAS produced by primary gamma. In *Proc. of the 19th International Cosmic Rays Conference*, volume 3, pages 445–448. NASA. Goddard Space Flight Center.

Hillas, A. M. (2005). Can diffusive shock acceleration in supernova remnants account for high-energy galactic cosmic rays? *Journal of Physics G: Nuclear and Particle Physics*, 31(5):R95.

Hirata, K., Kajita, T., Koshiba, M., Nakahata, M., Oyama, Y., Sato, N., Suzuki, A., Takita, M., Totsuka, Y., Kifune, T., Suda, T., Takahashi, K., Tanimori, T., Miyano, K., Yamada, M., Beier, E. W., Feldscher, L. R., Kim, S. B., Mann, A. K., Newcomer, F. M., Van, R., Zhang, W., and Cortez, B. G. (1987). Observation of a neutrino burst from the supernova SN1987A. *Physical Review Letters*, 58(14):1490–1493.

Hirotani, K. (2006). High-Energy Emission from Pulsar Magnetospheres. *Modern Physics Letters A*, 21:1319–1337.

Hobbs, G. B., Edwards, R. T., and Manchester, R. N. (2006). TEMPO2, a new pulsar-timing package - I. An overview. *Monthly Notices of the Royal Astronomical Society*, 369:655–672.

Hooper, D. and Taylor, A. M. (2010). On the heavy chemical composition of the ultra-high energy cosmic rays. *Astroparticle Physics*, 33(3):151–159.

Hrupec, D. (2008). *Extragalactic sources of rapidly variable high energy gamma radiation*. PhD thesis, University of Zagreb, Zagreb.

Hudson, H. and Ryan, J. (1995). High-energy particles in solar flares. *Annual Review of Astronomy and Astrophysics*, 33(1):239–282.

Ignasi, R. (2009). *Massive, automatic data analysis for the MAGIC telescopes*. Master thesis, Universitat Autonoma de Barcelona, Barcelona.

Jackson, J. D. (1999). *Classical Electrodynamics*. John Wiley & Sons Inc, third edition.

James, F. and Roos, M. (1975). Minuit - a system for function minimization and analysis of the parameter errors and correlations. *Computer Physics Communications*, 10(6):343–367.

Jones, T. W., O'dell, S. L., and Stein, W. A. (1974). Physics of compact nonthermal sources. i. theory of radiation processes. *e Astrophysical Journal*, 188:353–368.

Kang, H. and Jones, T. (2006). Numerical studies of diffusive shock acceleration at spherical shocks. *Astroparticle Physics*, 25(4):246–258.

Kashlinsky, A. (2005). Cosmic infrared background and early galaxy evolution. *Physics Reports*, 409(6):361–438.

Kembhavi, A. K. and Narlikar, J. V. (1999). *Quasars and Active Galactic Nuclei: An Introduction*. Cambridge University Press.

Kino, M., Takahara, F., and Kusunose, M. (2002). Energetics of TeV blazars and physical constraints on their emission regions. *e Astrophysical Journal*, 564(1):97–107.

Kneiske, T. M. and Dole, H. (2010). A lower-limit flux for the extragalactic background light. *Astronomy and Astrophysics*, 515:19.

Kniffen, D., Hartman, R., Thompson, D., FICHTEL, C., TUMER, T., Ogelman, H., and BIGNAMI, G. (1974). Gamma radiation from the Crab Nebula above 35 MeV. *Nature*, 251:397–399.

Kocevski, D. D. et al. (2012). CANDELS: constraining the AGN-Merger connection with host morphologies at z ~ 2. *e Astrophysical Journal*, 744:148.

KolhHrster, W. (1913). Messungen der durchdringenden strahlung im freiballon in grHsseren h|"ohen. *Physikalische Zeitschr*, 14:1153–1156.

Konopelko, A. et al. (1999). Performance of the stereoscopic system of the HEGRA imaging air erenkov telescopes: Monte carlo simulations and observations. *Astroparticle Physics*, 10(4):275–289.

Krawczynski, H., Hughes, S. B., Horan, D., Aharonian, F., Aller, M. F., Aller, H., Boltwood, P., Buckley, J., Coppi, P., Fossati, G., Gotting, N., Holder, J., Horns, D., Kurtanidze, O. M., Marscher, A. P., Nikolashvili, M., Remillard, R. A., Sadun, A.,

and Schroder, M. (2004). Multiwavelength observations of strong flares from the TeV blazar 1ES 1959+650. *The Astrophysical Journal*, 601(1):151–164.

Krymskii, G. F. (1977). A regular mechanism for the acceleration of charged particles on the front of a shock wave. *Akademiia Nauk SSSR Doklady*, 234:1306–1308.

Kuiper, L., Hermsen, W., Cusumano, G., Diehl, R., Schonfelder, V., Strong, A., Bennett, K., and McConnell, M. (2001). The Crab pulsar in the 0.75-30 MeV range as seen by CGRO COMPTEL. *Arxiv preprint astro-ph/0106077*.

Lagage, P. O. and Cesarsky, C. J. (1983). The maximum energy of cosmic rays accelerated by supernova shocks. *Astronomy and Astrophysics*, 125:249–257.

Landau, L. D. (1932). On the theory of stars. *Phys. Z. Sowjetunion*, 1:285.

Lattes, C. M. G., Occhialini, G. P. S., and Powell, C. F. (1947). Observations on the tracks of slow mesons in photographic emulsions. *Nature*, 160(4066):453–456.

Laurent-Muehleisen, S. A., Kollgaard, R. I., Ryan, P. J., Feigelson, E. D., Brinkmann, W., and Siebert, J. (1997). Radio-loud active galaxies in the northern ROSAT all-sky survey. i. radio identifications. *Astronomy and Astrophysics Supplement Series*, 122:235–247.

Li, T.-P. and Ma, Y.-Q. (1983). Analysis methods for results in gamma-ray astronomy. *The Astrophysical Journal*, 272:317.

Lombardi, S. (2011). Advanced stereoscopic gamma-ray shower analysis with the MAGIC telescopes. In *International Cosmic Ray Conference*, volume 3 of *International Cosmic Ray Conference*, page 262.

Longair, M. S. (2011). *High Energy Astrophysics*. Cambridge University Press.

Longo, E. and Sestili, I. (1975). Monte carlo calculation of photon-initiated electromagnetic showers in lead glass. *Nuclear Instruments and Methods*, 128(2):283–307.

Lovelace, R. V. E. and Romanova, M. M. (2003). Relativistic poynting jets from accretion disks. *The Astrophysical Journal*, 596(2):L159–L162.

Lynden-Bell, D. (1969). Galactic nuclei as collapsed old quasars. *, Published online: 00 August 0000; | doi:00.0000/000000a0*, 223(5207):690–694.

Lyne, A. G., Pritchard, R. S., and Graham-Smith, F. (1993). Twenty-Three Years of Crab Pulsar Rotational History. *Monthly Notices of the Royal Astronomical Society*, 265:1003.

Lyutikov, M., Otte, N., and McCann, A. (2012). The Very High Energy Emission from Pulsars: A Case for Inverse Compton Scattering. *The Astrophysical Journal*, 754:33.

Malkan, M. A. and Sargent, W. L. W. (1982). The ultraviolet excess of seyfert 1 galaxies and quasars. *The Astrophysical Journal*, 254:22–37.

Manchester, R. N., Hobbs, G. B., Teoh, A., , and Hobbs, M. (2005). The australia telescope national facility pulsar catalogue. *The Astronomical Journal*, 129(4):1993–2006.

Manchester, R. N. and Taylor, J. H. (1977). *Pulsars*. W. H. Freeman, San Francisco :.

Mannheim, K. and Biermann, P. L. (1992). Gamma-ray flaring of 3C 279 - a proton-initiated cascade in the jet? *Astronomy and Astrophysics*, 253:L21–L24.

Maraschi, L., Ghisellini, G., and Celotti, A. (1992). A jet model for the gamma-ray emitting blazar 3C 279. *The Astrophysical Journal Letters*, 397:L5–L9.

Mariotti, M. and Collaboration, M. (2010). Discovery of very high energy gamma-ray emission from b3 2247+381 by MAGIC. *The Astronomer's Telegram*, 2910:1.

Marscher, A. P., Jorstad, S. G., Gómez, J.-L., Aller, M. F., Ter"sranta, H., Lister, M. L., and Stirling, A. M. (2002). Observational evidence for the accretion-disk origin for a radio jet in an active galaxy. *Nature*, 417(6889):625–627.

Massaro, E., Perri, M., Giommi, P., and Nesci, R. (2004). Log-parabolic spectra and particle acceleration in the BL lac object mkn 421: Spectral analysis of the complete BeppoSAX wide band x-ray data set. *Astronomy and Astrophysics*, 413(2):489–503.

Matthews, J. (2005). A heitler model of extensive air showers. *Astroparticle Physics*, 22(5–6):387–397.

Mattila, K. (2006). The 1-μ m discontinuity in the extragalactic background light spectrum: an artefact of foreground subtraction. *Monthly Notices of the Royal Astronomical Society*, 372:1253–1258.

Mattox, J. R., Bertsch, D. L., Chiang, J., Dingus, B. L., Digel, S. W., Eposito, J. A., Fierro, J. M., Hartman, R. C., Hunter, S. D., Kanbach, G., Kniffen, D. A., Lin, Y. C., Macomb, D. J., Mayer-Hasselwander, H. A., Michelson, P. F., von Montigny, C., Mukherjee, R., Nolan, P. L., Ramanamurthy, P. V., Schneid, E., Sreekumar, P., Thompson, D. J., and Willis, T. D. (1996). The likelihood analysis of EGRET data. *The Astrophysical Journal*, 461:396.

Maurin, D., Taillet, R., and Donato, F. (2002). New results on source and diffusion spectral features of Galactic cosmic rays: I B/C ratio. *Astronomy and Astrophysics*, 394(3):1039–1056.

Mazin, D. and Raue, M. (2007). New limits on the density of the extragalactic background light in the optical to the far infrared from the spectra of all known TeV blazars. *Astronomy and Astrophysics*, 471(2):439–452.

Meyer, M., Raue, M., Mazin, D., and Horns, D. (2012). Limits on the extragalactic background light in the fermi era. *Astronomy & Astrophysics*, 542.

Miller, J. (1998). Particle acceleration in impulsive solar flares. *Space Science Reviews*, 86(1):79–105.

Miller, J. A. et al. (1997). Critical issues for understanding particle acceleration in impulsive solar flares. *Journal of Geophysical Research*, 102(A7):14631–14,659.

Millikan, R. A. and Cameron, G. H. (1926). High frequency rays of cosmic origin iii. measurements in snow-fed lakes at high altitudes. *Phys. Rev.*, 28:851–868.

Mitton, S. (1979). The crab nebula. *London: Faber and Faber,* ----, 1.

Molière, G. (1947). Theorie der streuung schneller geladener teilchen i. einzelstreuung am abgeschirmten coulomb-feld. *Zeitschri- Naturforschung Teil A*, 2:133.

Molière, G. (1948). Theorie der streuung schneller geladener teilchen II. mehrfach- und vielfachstreuung. *Zeitschri- Naturforschung Teil A*, 3:78.

Moralejo, A., Gaug, M., Carmona, E., Colin, P., Delgado, C., Lombardi, S., Mazin, D., Scalzotto, V., Sitarek, J., Tescaro, D., and collaboration, f. t. M. (2009). MARS, the MAGIC analysis and reconstruction software. *arXiv*:--------.

Moskalenko, I. V., Strong, A. W., Mashnik, S. G., and Ormes, J. F. (2003). Challenging Cosmic-Ray Propagation with Antiprotons: Evidence for a "Fresh" Nuclei Component? - *e Astrophysical Journal*, 586(2):1050–1066.

Murakami, H. et al. (1994). The infrared telescope in space (IRTS). - *e Astrophysical Journal*, 428:354–362.

Muslimov, A. and Harding, A. (2004). High-Altitude Particle Acceleration and Radiation in Pulsar Slot Gaps. - *e Astrophysical Journal*, 606(2):1143–1153.

MXcke, A. and Protheroe, R. (2001). A proton synchrotron blazar model for flaring in markarian 501. *Astroparticle Physics*, 15(1):121–136.

Nakamura, K. et al. (2010). Review of particle physics. *Journal of Physics G: Nuclear and Particle Physics*, 37(7A):075021.

NASA (2012a). Fermi Science Support Center.

NASA (2012b). HEASoft: A Unified Release of the FTOOLS and XANADU Software Packages.

Neronov, A., Semikoz, D., and Vovk, I. (2011). High galactic latitude fermi sources of γ-rays with energies above 100 GeV. *Astronomy & Astrophysics*, 529:A59.

Neumann, M., Reich, W., Fuerst, E., Brinkmann, W., Reich, P., Siebert, J., Wielebinski, R., and Truemper, J. (1994). Multifrequency observations of ROSAT selected radio sources. *Astronomy and Astrophysics Supplement Series*, 106:303–326.

Nieppola, E., Tornikoski, M., and Valtaoja, E. (2006). Spectral energy distributions of a large sample of BL lacertae objects. *Astronomy and Astrophysics*, 445(2):441–450.

Nilsson, K., Pasanen, M., Takalo, L. O., Lindfors, E., Berdyugin, A., Ciprini, S., and Pforr, J. (2007). Host galaxy subtraction of TeV candidate BL lacertae objects. *Astronomy and Astrophysics*, 475(1):199–207.

Nilsson, K., Pursimo, T., Heidt, J., Takalo, L. O., Sillanp"", A., and Brinkmann, W. (2003). R-band imaging of the host galaxies of RGB BL lacertae objects. *Astronomy and Astrophysics*, 400:95–118.

Nolan, P. L. et al. (2012). FERMI LARGE AREA TELESCOPE SECOND SOURCE CATALOG. *e Astrophysical Journal Supplement Series*, 199(2):31.

Oda, M., Nishimura, J., and Sakurai, K. (1988). *Cosmic Ray Astrophysics*. Terra Scientific Publishing Company.

Omodei, N., Longo, F., Share, G., Briggs, M., Gruber, D., LAT, F., and GBM Collaborations (2012). Fermi LAT Observation of Highly Energetic Impulsive Solar Flares. In *American Astronomical Society Meeting Abstracts #*, volume 220 of *American Astronomical Society Meeting Abstracts*, page 424.03.

Padovani, P., Perlman, E. S., Landt, H., Giommi, P., and Perri, M. (2003). What types of jets does nature make? a new population of radio quasars. *e Astrophysical Journal*, 588(1):128–142.

Pellizzoni, A., Pilia, M., Possenti, A., Chen, A., Giuliani, A., Trois, A., Caraveo, P., Del Monte, E., Fornari, F., Fuschino, F., et al. (2009). New Gamma-Ray Pulsars. *e Astrophysical Journal Letters*, 695:L115–L119.

P"tri, J. (2011). A unified polar cap/striped wind model for pulsed radio and gamma-ray emission in pulsars. *Monthly Notices of the Royal Astronomical Society*, 412:1870–1880.

Pozdnyakov, L. A., Sobol, I. M., and Syunyaev, R. A. (1983). Comptonization and the shaping of x-ray source spectra - monte carlo calculations. *Astrophysics and Space Physics Reviews*, 2:189–331.

Prandini, E., Bonnoli, G., Maraschi, L., Mariotti, M., and Tavecchio, F. (2010). Constraining blazar distances with combined fermi and TeV data: an empirical approach. *Monthly Notices of the Royal Astronomical Society: Letters*, 405(1):L76–L80.

Reinthal, R., Lindfors, E. J., Mazin, D., Nilsson, K., Takalo, L. O., Sillanp"", A., Berdyugin, A., and the MAGIC Collaboration (2012). Connection between optical and VHE gamma-ray emission in blazar jets. *Journal of Physics: Conference Series*, 355:012013.

Rissi, M., Otte, N., Schweizer, T., and Shayduk, M. (2009). A New Sum Trigger to Provide a Lower Energy Threshold for the MAGIC Telescope. *IEEE Transactions on Nuclear Science*, 56:3840–3843.

Robson, I. (1996). *Active Galactic Nuclei*. John Wiley & Sons, 1 edition.

Rochester, G. and Butler, C. (1947). Evidence for the existence of new unstable elementary particles. *Nature*, 160(855):173.

Roming, P., Kennedy, T., Mason, K., Nousek, J., Ahr, L., Bingham, R., Broos, P., Carter, M., Hancock, B., Huckle, H., Hunsberger, S., Kawakami, H., Killough, R., Koch, T., Mclelland, M., Smith, K., Smith, P., Soto, J., Boyd, P., Breeveld, A., Holland, S., Ivanushkina, M., Pryzby, M., Still, M., and Stock, J. (2005). The *Swi* ultra-Violet/Optical telescope. *Space Science Reviews*, 120(3):95–142.

Rossi, B. and Greisen, K. (1941). Cosmic-ray theory. *Reviews of Modern Physics*, 13(4):240–309.

Ruderman, M. and Sutherland, P. (1975). Theory of pulsars- Polar caps, sparks, and coherent microwave radiation. *Astrophysical Journal*, 196(pt 1).

Rybicki, G. B. and Lightman, A. P. (1991). *Radiative Processes in Astrophysics*. John Wiley & Sons.

Saito, T. (2010). *Study of the High Energy Gamma-ray Emission from the Crab Pulsar with the MAGIC telescope and Fermi-LAT*. PhD thesis, Ludwig-Maximilians-Universit"t MXnchen, Munich.

Salpeter, E. E. (1964). Accretion of interstellar matter by massive objects. *e Astrophysical Journal*, 140:796–800.

Scherer, K., Fichtner, H., Borrmann, T., Beer, J., Desorgher, L., FlXkiger, E., Fahr, H., Ferreira, S., Langner, U., Potgieter, M., Heber, B., Masarik, J., Shaviv, N., and Veizer, J. (2006). Interstellar-Terrestrial relations: Variable cosmic environments, the dynamic heliosphere, and their imprints on terrestrial archives and climate. *Space Science Reviews*, 127(1):327–465.

Schlafly, E. F. and Finkbeiner, D. P. (2011). Measuring reddening with sloan digital sky survey stellar spectra and recalibrating SFD. *e Astrophysical Journal*, 737:103.

Schmidt, F. (2012). Corsika shower images. Retrieved on 2012-10-30.

Seyfert, C. K. (1943). Nuclear emission in spiral nebulae. The Astrophysical Journal, 97:28.

Shapiro, S. L. and Teukolsky, S. A. (1983). *Black Holes, White Dwarfs, and Neutron Stars: The Physics of Compact Objects*. Wiley-Interscience.

Shields, G. A. (1978). Thermal continuum from accretion disks in quasars. *Nature*, 272(5655):706–708.

Sikora, M., Begelman, M. C., Madejski, G. M., and Lasota, J. (2005). Are quasar jets dominated by poynting flux? The Astrophysical Journal, 625(1):72–77.

Simpson, J. A. (1983). Elemental and isotopic composition of the galactic cosmic rays. *Annual Review of Nuclear and Particle Science*, 33(1):323–382.

Staelin, D. and Reifenstein, E. (1968). Pulsating radio sources near the Crab Nebula. *Science*, 162(3861):1481–1483.

Strong, A. W., Moskalenko, I. V., and Ptuskin, V. S. (2007). Cosmic-Ray propagation and interactions in the galaxy. *Annual Review of Nuclear and Particle Science*, 57(1):285–327.

Sturner, S. and Dermer, C. (1994). On the spectra and pulse profiles of gamma-ray pulsars. *Astrophysical Journal*, 420:79–79.

Sturrock, P. (1971). A model of pulsars. The Astrophysical Journal, 164:529.

Svensmark, H., Pedersen, J. O. P., Marsh, N. D., Enghoff, M. B., and Uggerhøj, U. I. (2007). Experimental evidence for the role of ions in particle nucleation under atmospheric conditions. *Proceedings of the Royal Society A: Mathematical, Physical and Engineering Science*, 463(2078):385–396.

Swordy, S. P., Mueller, D., Meyer, P., L'Heureux, J., and Grunsfeld, J. M. (1990). Relative abundances of secondary and primary cosmic rays at high energies. The Astrophysical Journal, 349:625–633.

Tavani, M., Barbiellini, G., Argan, A., Bulgarelli, A., Caraveo, P., Chen, A., Cocco, V., Costa, E., de Paris, G., Del Monte, E., di Cocco, G., Donnarumma, I., Feroci, M., Fiorini, M., Froysland, T., Fuschino, F., Galli, M., Gianotti, F., Giuliani, A., Evangelista, Y., Labanti, C., Lapshov, I., Lazzarotto, F., Lipari, P., Longo, F., Marisaldi, M., Mastropietro, M., Mauri, F., Mereghetti, S., Morelli, E., Morselli, A., Pacciani, L., Pellizzoni, A., Perotti, F., Picozza, P., Pontoni, C., Porrovecchio, G., Prest, M., Pucella, G., Rapisarda, M., Rossi, E., Rubini, A., Soffitta, P., Trifoglio, M., Trois, A., Vallazza, E., Vercellone, S., Zambra, A., Zanello, D., Giommi, P., Antonelli, A., and Pittori, C. (2008). The AGILE space mission. *Nuclear Instruments and Methods in Physics Research A*, 588:52–62.

Tavecchio, F., Ghisellini, G., Ghirlanda, G., Foschini, L., and Maraschi, L. (2010). TeV BL lac objects at the dawn of the fermi era. *Monthly Notices of the Royal Astronomical Society*, 401(3):1570–1586.

Tavecchio, F., Maraschi, L., and Ghisellini, G. (1998). Constraints on the physical parameters of TeV blazars. *The Astrophysical Journal*, 509(2):608–619.

Tavecchio, F., Maraschi, L., Pian, E., Chiappetti, L., Celotti, A., Fossati, G., Ghisellini, G., Palazzi, E., Raiteri, C. M., Sambruna, R. M., Treves, A., Urry, C. M., Villata, M., and Djannati-Atai, A. (2001). Theoretical implications from the spectral evolution of markarian 501 observed with BeppoSAX. *The Astrophysical Journal*, 554(2):725–733.

Tavecchio, F., Maraschi, L., Sambruna, R. M., and Urry, C. M. (2000). The x-ray jet of PKS 0637–752: Inverse compton radiation from the cosmic microwave background? *The Astrophysical Journal*, 544(1):L23–L26.

Terrats, D. G. (2011). *The effect of molecular and aerosol atmospheric profiles on the performance of the MAGIC telescopes.* Master thesis, Universitat Autonoma de Barcelona, Barcelona.

Thompson, D. f. t. F.-L. C. (2009). List of tev candidates for cherenkov telescopes. private communication.

Thompson, D. J. (2003). Gamma ray pulsars: Multiwavelength observations. To appear in Cosmic Gamma Ray Sources, Kluwer ASSL Series, Edited by K.S. Cheng and G.E. Romero.

Tsai, Y.-S. (1974). Pair production and bremsstrahlung of charged leptons. *Reviews of Modern Physics*, 46(4):815–851.

Unger, M. (2008). Cosmic rays above the knee. *arXiv*:0806.0406.

UNSCEAR (2010). *Sources and Effects of Ionizing Radiation, UNSCEAR 2008 Report: Volume I: Sources - Report to the General Assembly, Scientific Annex B*. United Nations Scientific Committee on the Effect of Atomic Radiation, United Nations, United Nations Office at Vienna.

Urry, C. M. and Padovani, P. (1995). Unified schemes for radio-loud active galactic nuclei. *Publications of the Astronomical Society of the Pacific*, 107:803.

Vietri, M. (2008). *Foundations of High-Energy Astrophysics*. University Of Chicago Press.

Vlahakis, N. and Konigl, A. (2004). Magnetic driving of relativistic outflows in active galactic nuclei. i. interpretation of Parsec-Scale accelerations. *The Astrophysical Journal*, 605(2):656–661.

VHlk, H. J., Berezhko, E. G., and Ksenofontov, L. T. (2005). Magnetic field amplification in tycho and other shell-type supernova remnants. *Astronomy and Astrophysics*, 433(1):229–240.

V"ron-Cetty, M.-P. and V"ron, P. (2010). A catalogue of quasars and active nuclei: 13th edition. *Astronomy and Astrophysics*, 518:10.

Wagner, R. (2006). *Measurement of VHE γ-ray emission from four blazars using the MAGIC telescope and a comparative blazar study*. PhD thesis, Technische Universit" t, Munich.

Wagner, R. (2012). VHE gamma-ray skymap & source catalog - robert wagner. retrieved on October 18th, 2012.

Wakely, S. and Horan, D. (2012). TeVCat: an online catalog for TeV Astronomy. University of Chicago.

Wang, P. F., Wang, C., and Han, J. L. (2012). Curvature radiation in rotating pulsar magnetosphere. *Monthly Notices of the Royal Astronomical Society*.

Webber, W. R. (1983). Cosmic ray electrons and positrons – A review of current measurements and some implications. In Shapiro, M. M., editor, *Composition and Origin of Cosmic Rays*, volume 107 of *NATO ASIC Proc.*, page P83–100.

Weekes, T. C., Cawley, M. F., Fegan, D. J., Gibbs, K. G., Hillas, A. M., Kowk, P. W., Lamb, R. C., Lewis, D. A., Macomb, D., Porter, N. A., Reynolds, P. T., and Vacanti, G. (1989). Observation of TeV gamma rays from the crab nebula using the atmospheric cerenkov imaging technique. – *e Astrophysical Journal*, 342:379–395.

Weidinger, M., RXger, M., and Spanier, F. (2010). Modelling the steady state spectral energy distribution of the BL-Lac object PKS 2155-30.4 using a selfconsistent SSC model. *Astrophys. Space Sci. Trans.*, 6(1):1–7.

Weiler, K. and Panagia, N. (1980). Vela X and the Evolution of Plerions. *Astronomy and Astrophysics*, 90(3):269.

Wilkinson, D. (2012). Space weather overview. Retrieved on 2012-09-22.

Woosley, S. and Janka, T. (2005). The physics of core-collapse supernovae. *Nature Physics*, 1(3):147–154.

Wu, Z., Jiang, D. R., Gu, M., and Liu, Y. (2007). VLBI observations of seven BL lacertae objects from RGB sample. *Astronomy and Astrophysics*, 466(1):63–73.

Yamamoto, A., Abe, K., Fuke, H., Haino, S., Hams, T., Kim, K., Lee, M., Makida, Y., Matsuda, S., Mitchell, J., Moiseev, A., Nishimura, J., Nozaki, M., Orito, R., Orito, S., Ormes, J., Sakai, K., Sanuki, T., Sasaki, M., Seo, E., Shikaze, Y., Streitmatter, R., Suzuki, J., Tanaka, K., Thakur, N., Yamagami, T., Yoshida, T., and

Yoshimura, K. (2007). The BESS program. *Nuclear Physics B - Proceedings Supplements*, 166(0):62–67.

Yanasak, N. E. et al. (2001). Measurement of the secondary radionuclides ^{10}Be, ^{26}Al, ^{36}Cl, ^{54}Mn, and ^{14}C and implications for the galactic Cosmic-Ray age. *The Astrophysical Journal*, 563(2):768–792.

Zanin, R. (2011). *Observation of the Crab pulsar wind nebula and microquasar candidates with MAGIC*. Ph.D. thesis, Universitat Autonoma de Barcelona, Barcelona.

Zatsepin, G. T. and Kuz'min, V. A. (1966). Upper limit of the spectrum of cosmic rays. *Soviet Journal of Experimental and Theoretical Physics Letters*, 4:78.

Zdziarski, A. A., Fabian, A. C., Nandra, K., Celotti, A., Rees, M. J., Done, C., Coppi, P. S., and Madejski, G. M. (1994). Physical processes in the x-ray / gamma-ray source of IC4329A. *Monthly Notices of the Royal Astronomical Society*, 269:L55.

Zdziarski, A. A., Johnson, W. N., Done, C., Smith, D., and McNaron-Brown, K. (1995). The average x-ray/gamma-ray spectra of seyfert galaxies from GINGA and OSSE and the origin of the cosmic x-ray background. *The Astrophysical Journal Letters*, 438:L63–L66.

Zel'dovich, Y. B. and Novikov, I. D. (1964). The fate of a star and the evolution of gravitational energy upon accretion. *Soviet Physics Doklady*, 9:195.

Zhou, X. X. and The Tibet ASγ Collaboration (2010). On temporal variations of the multi-TeV cosmic ray anisotropy using the Tibet III air shower array. *The Astrophysical Journal*, 711(1):119–124.